

## INFORMATION TO USERS

**This manuscript has been reproduced from the microfilm master. UMI films the text directly from the original or copy submitted. Thus, some thesis and dissertation copies are in typewriter face, while others may be from any type of computer printer.**

**The quality of this reproduction is dependent upon the quality of the copy submitted. Broken or indistinct print, colored or poor quality illustrations and photographs, print bleedthrough, substandard margins, and improper alignment can adversely affect reproduction.**

**In the unlikely event that the author did not send UMI a complete manuscript and there are missing pages, these will be noted. Also, if unauthorized copyright material had to be removed, a note will indicate the deletion.**

**Oversize materials (e.g., maps, drawings, charts) are reproduced by sectioning the original, beginning at the upper left-hand corner and continuing from left to right in equal sections with small overlaps. Each original is also photographed in one exposure and is included in reduced form at the back of the book.**

**Photographs included in the original manuscript have been reproduced xerographically in this copy. Higher quality 6" x 9" black and white photographic prints are available for any photographs or illustrations appearing in this copy for an additional charge. Contact UMI directly to order.**

# UMI

A Bell & Howell Information Company  
300 North Zeeb Road, Ann Arbor, MI 48106-1346 USA  
313/761-4700 800/521-0600



**Modeling and Analysis of  
Radio Frequency Structures  
using an Equivalent Circuit Methodology with  
Application to Charged Particle Accelerator RF Resonators**

By

John J. Vincent

**A DISSERTATION**

Submitted to  
Michigan State University  
in partial fulfillment of the requirements  
for the degree of

**DOCTOR OF PHILOSOPHY**

Department of Electrical Engineering

1996

**UMI Number: 9631355**

**Copyright 1996 by  
Vincent, John J.**

**All rights reserved.**

---

**UMI Microform 9631355  
Copyright 1996, by UMI Company. All rights reserved.**

**This microform edition is protected against unauthorized  
copying under Title 17, United States Code.**

---

**UMI**  
**300 North Zeeb Road**  
**Ann Arbor, MI 48103**

## **ABSTRACT**

### **Modeling and Analysis of Radio Frequency Structures using an Equivalent Circuit Methodology with Application to Charged Particle Accelerator RF Resonators**

By

John J Vincent

The delineation of analysis techniques for high power radio frequency resonators, used as a fundamental component of particle accelerators, receives little attention in the literature. This dissertation reviews, describes, and develops techniques for resolving a transmission line mode rf resonator into an approximate equivalent circuit. Specifically, it presents a toolbox of techniques used to model and represent rf structures.

One technique develops models of transmission lines with varying characteristic impedance (referred to as non-uniform) using multiple series connected circuits consisting of lumped elements and constant impedance transmission lines based on a conserved energy approach. This technique is tested for exponentially tapered and linearly tapered quarter-wave resonators. Another technique developed, maps transmission lines with arbitrary cross-sections (referred to as nonstandard) to a standard structure that preserves the characteristic impedance and loss properties of the original line.

The techniques developed are applied to the analysis of the complex K1200 Superconducting Cyclotron rf resonators at the National Superconducting Cyclotron Laboratory (NSCL). The results predicted from the model are compared to measurements. The K1200 rf resonators are tunable over the frequency range of 9.5 to 27 MHz with tuning stems that vary from 300 cm to 11 cm respectively. The resonators are operated in the continuous wave (cw) mode and sustain peak voltages of up to 180 kV requiring drive power of up to 250 kW.

Using the techniques developed, the resonant frequency versus tuning stem position was predicted to within a positioning error that varied from 1 to 3.5 cm over the tuning range of 9.5 to 27 Mhz. The discrepancy between model predictions and the experimental data for the resonator power dissipation is postulated to be due to high surface resistance in regions where the rf surfaces were heavily worked or welded. After adjusting the surface resistance of these regions uniformly, the equivalent shunt circuit resistance was predicted accurately across the tuning range to within the maximum measurement accuracy of +/- 5 %.

**Copyright by**

**John J Vincent**

**1996**

**Dedicated to my mother**

**Olga N Vincent**

**who has always put her children first.**



## ACKNOWLEDGMENTS

I wish to thank my guidance committee, Dr. Jes Asmussen, Dr. Konrad Gelbke, Dr. Timothy Grotjohn, Dr. Elias Strangas, and Dr. Richard York for their encouragement, guidance, and support during this research. In particular, I thank Dr. Asmussen and Dr. Gelbke for allowing me to pursue research related to my work at the NSCL, Dr. Grotjohn and Dr. York for their overall guidance, many useful discussions, and for the multiple critical reviews of the manuscript, and Dr. Strangas for expanding my interests to the area of modern machines and power converters.

I wish to thank the entire NSCL staff for the support I have enjoyed over my entire tenure here. I especially thank the laboratory staff associated with operations and electronics for the timely scheduling of the experiments and for their assistance with operating the equipment and taking the data. In addition, I thank the NSCL design department, particularly Mr. Jack Ottarson and Mrs. Donna Rich, for the many drawings of the K1200. Finally, I wish to acknowledge my late mentor, Mr. Jack Riedel, for his guidance and encouragement during my indoctrination into this work; he is missed.

This research is supported through a combined effort by MSU and The National Science Foundation.

# **TABLE OF CONTENTS**

## **CHAPTER ONE**

### **Introduction**

<b>1.1 Research Institution</b>	<b>1</b>
<b>1.2 Research Scope</b>	<b>1</b>
<b>1.3 RF Resonators in Particle Accelerators</b>	<b>2</b>
<b>1.4 Basic NSCL Background</b>	<b>4</b>
<b>1.5 Application of the Equivalent Circuit Technique at NSCL</b>	<b>5</b>
<b>1.6 The Modeling and Analysis Methodology</b>	<b>7</b>
<b>1.7 The Thesis Format</b>	<b>9</b>

## **CHAPTER TWO**

### **A Historical Background of RF Structure Analysis**

2.1 Introduction	10
2.2 Computer Assisted Field Analysis	12
2.3 Computer Assisted Circuit Analysis	14
2.4 The Equivalent Circuit Technique	14
2.5 Advance of the Equivalent Circuit Technique at the NSCL	16
2.6 Equivalent Circuit Technique Attributes	18

## **CHAPTER THREE**

### **Properties of Resonator Materials and Joint**

3.1 Introduction	20
3.2 Conductors	20
3.2.1 Normal Conductors	22
3.2.2 Skin Depth	24
3.3 RF Joint Resistance	25
3.4 Insulators	32
3.4.1 Electrical Characteristics of Vacuum	33

3.4.1.1 Breakdown	33
3.4.1.2 Multipactoring	34
3.4.1.3 X-ray Production	36
3.4.1.4 Vacuum Windows	36
3.4.2 Electrical Characteristics of Air	38

## **CHAPTER FOUR**

### **Computer Software**

4.1 Introduction	39
4.2 Electrostatic Analysis Software	40
4.2.1 The COSMOS Finite Element Software Package	40
4.2.2 Custom Written Software	42
4.2.3 Some Known Test Cases	43
4.3 RESON : RF AC Circuit Analysis Software	45
4.3.1 Custom Written Software	46
4.3.2 The General Admittance Matrix for Transmission Lines	47
4.3.3 A Simple RESON Test Case	50

## **CHAPTER FIVE**

### **Equivalent Circuits, Coupled Circuits, and Circuit Error**

5.1	Introduction	54
5.2	Circuit Quality Factor (Q)	55
5.3	Reduced Circuit Representations	56
5.3.1	The Series Resonant Circuit	57
5.3.2	The Shunt Resonant Circuit	57
5.4	Coupled Resonant Circuits	60
5.4.1	Overview	60
5.4.2	Qualitative Description of Coupled Resonators	60
5.5	Impedance Matched Input Coupling	62
5.5.1	Capacitive Coupling	64
5.5.2	Inductive Coupling	64
5.6	Model Uncertainties and Circuit Error Estimates	67

## **CHAPTER SIX**

### **Standard Elements of the Equivalent Circuit**

6.1	Introduction	70
6.1.1	Modeling the Lumped Elements	71

6.1.2 Elements with Significant Distributed Effects	72
6.2 Lead Inductance and Resistance	73
6.3 The Resistor Model	73
6.4 The Capacitor Model	76
6.5 The Inductor Model	78
6.5.1 Common Formulas for Ideal Inductances	80
6.5.2 Solenoids with Significant Distributed Effects	82
6.5.3 Inductors as Electronic Tuning Elements	82
6.6 The Transmission Line Model	83
6.6.1 Ideal Coaxial and Parallel Plate Types	85
6.6.2 Coaxial Line with Intervening Coaxial Cylinder	85
6.6.3 Other Documented Line Types	89

## **CHAPTER SEVEN**

### **Nonstandard Transmission Lines 1: Nonstandard Cross-sections, Discontinuities, and Corners**

7.1 Introduction	90
7.2 Using Electrostatic Analysis to Determine Non-Standard Line Parameters	90
7.2.1 Characteristic Impedance	91

7.2.2	Conduction Losses	92
7.2.3	A Simple Illustrative Example	96
7.3	Transmission Line Discontinuities	98
7.3.1	Coaxial Step Discontinuities	98
7.3.2	Parallel Plate Step Discontinuities	98
7.4	Corners and Bends	103

## **CHAPTER EIGHT**

### **Nonstandard Transmission Lines 2: Non-Uniform Transmission Lines**

8.1	Introduction	111
8.2	Tapered Transmission Lines	112
8.2.1	The Tapered Line Circuit Model	112
8.2.2	The Transmission Line Segment	115
8.2.3	Other Methods for Choosing $Z_0$	118
8.3	An Exponentially Tapered Transmission Line	123
8.4	A Linearly Tapered Transmission Line	130
8.4.1	Development of the Segmentation Convergence Criteria	130

8.4.2 The Non-Uniform Tapered Transmission Line Modeling Process	136
--	-----

## **CHAPTER NINE**

### **Development of the K1200 Cyclotron RF Resonator Equivalent Circuit**

9.1 Introduction	138
9.2 Resonator Configuration	138
9.3 Developing the Resonator Model	140
9.4 Determining the Element Values	144
9.4.1 The K1200 Dee Elements	144
9.4.2 The Tuning Stem Elements	168
9.4.2.1 Joint Resistors	178
9.4.2.2 Annuli	178

## **CHAPTER TEN**

### **The K1200 Resonator Simulation and Measurements**

10.1 Introduction	180
10.2 Measurements of Shunt Capacitance and Voltage Variations by Method of Resonator Perturbation	181
10.2.1 Voltage Variations by Inserting a Known Capacitor	181



10.2.2 Measurement of the Shunt Capacitance	184
10.3 The Measurement Techniques and Trials	185
10.3.1 The X-ray Dee Voltage Measurement Technique	186
10.3.2 The Resonator Amplitude Measurement Technique	187
10.3.3 The Resonator Power Measurement Technique	189
10.4 The K1200 Measurements	193
10.5 The Simulation of the K1200 Resonator Model	196
10.6 Comparisons of Measurements to Simulations	202
10.7 Adjustments to the Simulation Model to Match Measurements	205

## **CHAPTER ELEVEN**

### **Summary**

1.0 Overview of the Problem	207
2.0 Summary of the Dissertation	208
3.0 Conclusion	211
4.0 Directions for Future Research	212

## **LIST OF TABLES**

<b>Table 3.1 Common Conductor Material Parameters [1.5]</b>	<b>23</b>
<b>Table 3.2 Seal Resistance versus Frequency</b>	<b>28</b>
<b>Table 4.1 Four Coaxial Test Cases</b>	<b>45</b>
<b>Table 4.2 Closed Form Calculations versus RESON Predictions for a Coaxial Resonator</b>	<b>51</b>
<b>Table 5.1 Definition of Common Symbols</b>	<b>56</b>
<b>Table 5.2 Common Subscripts</b>	<b>56</b>
<b>Table 8.1 Percent Error for the Four Choices of <math>Z_t</math></b>	<b>121</b>
<b>Table 9.1 Results of K1200 Dee Cross-section Analysis</b>	<b>146</b>
<b>Table 9.2 The K1200 Dee Transmission Line Chart</b>	<b>160</b>
<b>Table 9.3 The K1200 Dee Stem Cross-section Data</b>	<b>172</b>
<b>Table 9.4 The K1200 Dee Stem Transmission Lines</b>	<b>173</b>
<b>Table 9.5 The K1200 Coaxial Step Capacitors</b>	<b>174</b>
<b>Table 9.6 The K1200 Dee Stem Joint Resistances</b>	<b>178</b>

<b>Table 9.7 The K1200 Annuli</b>	<b>179</b>
<b>Table 10.1 The K1200 DV4 Monitor Calibration</b>	<b>194</b>
<b>Table 10.2 The K1200 Shunt Resistance Measurements</b>	<b>194</b>
<b>Table 10.3 The K1200 Tuning Stem Measurements</b>	<b>196</b>
<b>Table 10.4 The K1200 Resonator Simulation</b>	<b>197</b>
<b>Table 10.5 The K1200 Element Sensitivity at 26.5 MHz</b>	<b>199</b>
<b>Table 10.6 The K1200 Simulated and Measured Average Values</b>	<b>202</b>

## LIST OF FIGURES

Figure 1.1	The proposed coupled cyclotron system.	3
Figure 3.1	The NSCL finger contacts for sliding joints.	30
Figure 4.1	Four numerically analyzed coaxial test cases using COSMOS.	44
Figure 4.2	The general transmission line circuit model.	49
Figure 4.3	The RESON input file for an example coaxial resonator.	52
Figure 4.4	The RESON output report for the example coaxial resonator.	53
Figure 5.1	The "Series Resonant Circuit".	58
Figure 5.2	The "Shunt Resonant Circuit".	59
Figure 5.3	Low-loss identical coupled resonant circuits.	61
Figure 5.4	Matched capacitive coupling to a feedline of impedance $Z_0$ .	65
Figure 5.5	Matched inductive coupling to a feedline of impedance $Z_0$ .	66

Figure 5.6	The error analysis circuit.	69
Figure 6.1	The inductance and resistance of a round conductor (a) and rectangular conductor (b). Use dimensional units consistent with $\mu$ and $\sigma$ .	74
Figure 6.2	The model of a lumped resistor including parasitic effects.	75
Figure 6.3	The model of a lumped capacitor including parasitic effects.	77
Figure 6.4	The model of a lumped inductor including parasitic effects.	79
Figure 6.5	The ideal self inductance of (a) the square core toroid, and (b) the air core solenoid.	81
Figure 6.7	The lossy transmission line circuit formulation.	84
Figure 6.8	Standard coaxial and parallel plate transmission lines.	86
Figure 6.9	A coaxial transmission line with an intervening dielectric cylinder.	87
Figure 7.1	A simple illustrative mapping example.	97
Figure 7.1	Formulas for steps in the inner and outer conductors of coaxial lines. Use units of centimeters.	99
Figure 7.2	The dual problems of a step in height and step in width of a parallel plate transmission line neglecting side fringes.	101
Figure 7.3	Formulas for steps in the height or width of parallel plate lines.	104

Figure 7.4	The dual problems of a E-Plane and H-Plane 90 degree bend for a parallel plate transmission line.	105
Figure 7.5	Modeling of 90 degree corners and bends in parallel plate transmission lines.	107
Figure 7.6	Summary of corners and bends.	110
Figure 8.1	Two tapered transmission lines and the associated : Segment Equivalent Circuit" (SEC).	113
Figure 8.2	A comparison of the choices for the transverse impedance.	122
Figure 8.3	The simulated exponential ( $Z_0$ ) line versus theory.	126
Figure 8.4	The simulated exponential ( $Z_1$ ) line versus measured results.	128
Figure 8.5	A plot of the exponentially tapered transmission lines results.	129
Figure 8.6	An overview of the linearly tapered transmission line study.	132
Figure 8.7	Plots of the convergence versus segmentation for linearly tapered quarter-wave resonators.	133
Figure 8.8	Constant error curves for linearly tapered quarter-wave resonators.	135
Figure 9.1	An overview of the K1200 cyclotron rf resonators.	139
Figure 9.2	The K1200 resonator quarter wave section circuit topology.	141

Figure 9.3	The top view of the K1200 dee showing the cross-sections to be analyzed.	143
Figure 9.4	The K1200 dee cross-sections (not to scale).	147
Figure 9.5	The K1200 dee tip geometry (not to scale).	163
Figure 9.6	The K1200 dee fine tuner (DFT).	164
Figure 9.7	The K1200 dee fine tuner transmission lines.	166
Figure 9.8	The K1200 dee stem.	169
Figure 9.9	The K1200 stem cross-sections.	170
Figure 9.10	The K1200 tunable stem sections.	177
Figure 10.1	98 kV X-ray spectrum from the K1200 C dee at 26.5 MHz.	188
Figure 10.1	The K1200 measured shunt resistance at the cyclotron center.	195
Figure 10.2	The K1200 simulated versus measured shunt resistance.	203
Figure 10.3	The K1200 tuning stem measured versus simulated positions.	204
Figure 10.4	The simulated shunt resistance with the resistivity degraded.	206

# **CHAPTER ONE**

## **Introduction**

### **1.1 Research Institution**

The work performed in this thesis is done in support of the National Superconducting Cyclotron Laboratory (NSCL) located on the campus of Michigan State University (MSU). The NSCL is supported by both MSU and the National Science Foundation (NSF). This work is an interdepartmental effort between the Electrical Engineering Department of the College of Engineering of MSU and the NSCL.

### **1.2 Research Scope**

This dissertation will develop and apply an equivalent circuit technique used to model and predict the performance of non-radiating radio frequency (rf) structures. In particular, the technique is applied to predict and document the performance of the K1200 Superconducting Cyclotron room temperature rf resonators (K12RF). The performance of the K12RF predicted by this procedure is then compared to the experimentally measured performance to validate the equivalent circuit models.



The NSCL has proposed to significantly add to its current capabilities by coupling the two cyclotrons, the K500 and K1200, together. Figure 1.1 shows a diagram of the proposed coupled cyclotron system. Since a significant portion of the current plans call for improving the K500 rf system (K5RF) and adding a new High Energy Buncher (HEB), documenting and testing this rf modeling and analysis technique as a feasible method of designing and predicting the performance of the new systems is desired. The accuracy of the analysis for the K5RF and the HEB can be expected to be similar to the results obtained for the K12RF.

Although this dissertation will concentrate on applying the described techniques to the K1200, it also serves to document and validate the employed procedures. In contrast to other analysis tools such as the three dimensional numerical techniques, the equivalent circuit technique is significantly less complex and offers increased speed of testing possible design options to optimize the performance of rf resonators and document the result. Hence this equivalent circuit technique, when it is applicable, is a significant asset to the accelerator community.

### **1.3 RF Resonators in Particle Accelerators**

Particle accelerators (such as cyclotrons) accelerate charged particles by passing them, one or more times, through strong synchronized electric force fields. RF resonators are used to efficiently maintain and synchronize the electric fields. Two conductor rf resonators are an integral part of many particle accelerators that require rapid time varying

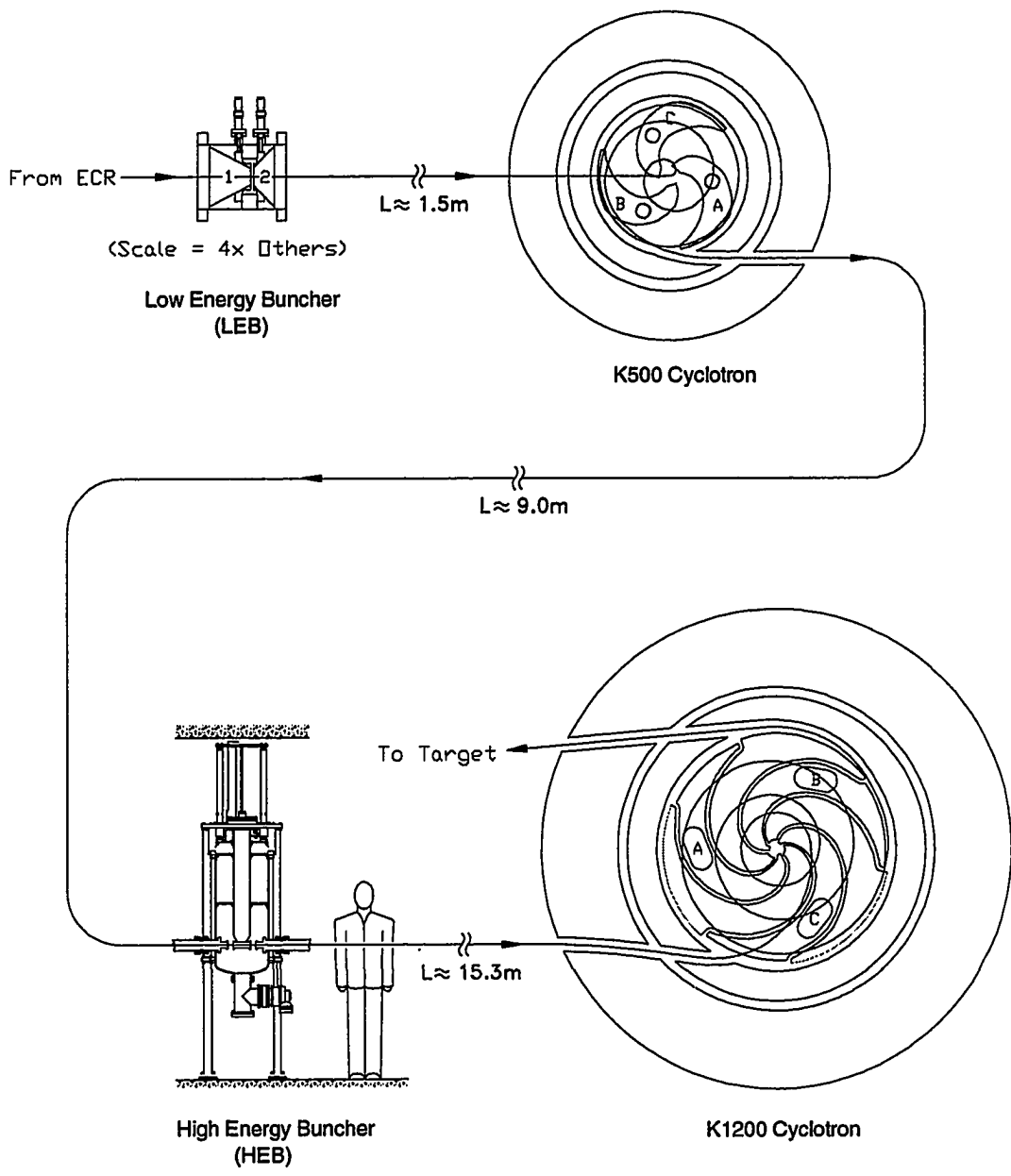


Figure 1.1 The proposed coupled cyclotron system.

synchronized voltages. The resonant circuit(s) are used to efficiently apply high voltages to the gaps that accelerate the passing charged particles. The application of high voltages to the accelerating gaps, without the use of resonant circuits, would require the energy stored in the electric field to be removed as heat each cycle. When resonant circuits are used, the stored energy alternates between electric and magnetic energy each cycle rather than being dissipated as heat. For example, the K1200 superconducting cyclotron has 3 accelerating structures called "dees" each of which have approximately 350 pF of capacitance when the resonator is tuned to 27 MHz. At this frequency, the dee operating peak voltage of 180 kV would require approximately 480 MW per dee if resonators were not employed to manage the circulating energy. With resonators, the necessary drive power needed without resonance is reduced by approximately the quality factor (Q) of the resonator which may have values ranging from a few hundred to tens of thousands. In particular, the K1200 Q varies from 6400 at 9 MHz to 3300 at 27 MHz.

#### **1.4 Basic NSCL Background**

The NSCL developed the worlds first superconducting cyclotron (the K500) followed by a more powerful cyclotron (the K1200). The techniques and software developed at the NSCL by this student [1.1, 1.2, 1.3] over the past 13 years to advance the equivalent circuit method of analysis of rf structures used in these cyclotrons and associated equipment are described and applied in this thesis.

The techniques described are significantly advanced from the techniques used in 1983 when the K1200 design began which consisted of 1) using resistive paper to determine transmission line characteristic impedance, 2) using a small set of subroutines written in BASIC (run on a sigma-7 or VAX 11/750 computer) to determine a first order circuit response, and 3) using low power scale models to verify and augment the calculations. The complexity of circuits and of the analysis that could be handled by the previous techniques are severely limited. In addition, the application of the previous techniques required a significantly greater amount of time and manpower to yield less information than the new techniques and computer software applied in this thesis.

The techniques developed and presented in this dissertation removed the need for using resistive paper techniques by applying two-dimensional electrostatic numerical analysis. In addition, a general purpose ac circuit analysis code, optimized for rf circuit analysis, has been developed (RESON) [1.3] and distributed to allow analysis of rf circuits of arbitrary complexity without any need of additional programming. When properly applied, the accuracy of the code and techniques developed have removed the need for low power models except in cases where high sensitivity to model parameters is noted.

### **1.5 Application of the Equivalent Circuit Technique at NSCL**

The equivalent circuit method described herein uses a circuit consisting of standard TEM mode transmission lines and lumped elements to model electromagnetic structures. The power of the method lies in the

fact that geometrically complex electromagnetic structures can be modeled using a simpler equivalent circuit, and that approximate representation of components can be modeled for which closed form solutions are either not available or feasible. The techniques described here are applied to multiple conductor TEM mode resonant structures operating in the so-called "transmission line mode" for which there is no lower cutoff frequency. The technique is applied to predict the performance of the K1200 resonators operating over the tuning range of 9.5 - 26.5 MHz. The calculated results are then compared to measurements.

The technique is applied in three steps. Step one describes the structure as an equivalent circuit topology consisting of transmission lines and lumped elements. Step two determines the values of each of the elements comprising the circuit topology found in step one. Finally, step three applies sinusoidal steady state circuit analysis to the resultant equivalent circuit to determine quantities of interest such as voltages, currents, resonant frequencies, stored energy, and power dissipation.

The equivalent circuit model is shown to be valid over the frequency band where the characteristics of the transmission lines and lumped elements in the circuit match the characteristics of the structure being modeled. The amount of effort put into the modeling is correlated with the accuracy of the results and is reasonably guided by the project requirements. If the model is to be used as a part of a conceptual design process, or the circumstance that the design has compensation for model uncertainties, then a very accurate modeling process is not necessary. On the other hand, if the device must work within tight design constraints, and would be very expensive to redesign and build, then time spent on

accurate models is justified. In this thesis, the equivalent circuit approach is shown to predict the response of the K1200 cyclotron rf resonators to within a few percent over the operating frequency band.

## **1.6 The Modeling and Analysis Methodology**

Step one of the modeling process requires an equivalent circuit topology be found. This step of the modeling process is not concerned with determining the electrical parameters of the elements, but rather with the types and arrangements of elements to be used. The resonator is first segmented into transmission line segments by inspecting the accelerating structure to determine the guided wave axes in the structure. The circuit topology consisting of loops and branches is normally obvious at this point of the modeling process. A typical equivalent circuit topology consists of one or more interconnected branches and/or loops of circuit elements consisting of equivalent transmission lines and lumped elements. For each branch of the circuit for which there exists transmission line behavior, the branch is segmented into one or more series connected transmission lines and series or shunt elements. In addition, at points along each guided wave axis in the structure with abrupt mechanical discontinuities, such as steps or joints, circuits based on lumped elements are inserted to account for the effect of the aberration.

Step two of the modeling process determines the electrical parameters of each element of the circuit determined in step one. Transmission line segments with a varying characteristic impedance (referred to as "non-uniform" in the literature) are further segmented into

multiple series connected "Segment Equivalent Circuits" (SEC) at this point. In general, the electrical parameters of each of the elements are determined by maintaining the material properties, the electrostatic stored energy, the magnetostatic stored energy, the rf losses, and the lengths along the guided wave axes. A combination of closed form and numerical analysis techniques are applied to determine the element values. Closed form solutions to standard transmission line cross-sections may be found in handbooks [1.4, 1.5]. The parameters of non-standard transmission lines are determined by using the numerically calculated electric field to determine the characteristic impedance and loss parameters. Often, the handbook formulas for standard lines do not contain loss information and a numerical analysis must be applied in these cases to obtain the missing information.

Step three simulates the equivalent circuit derived using normal sinusoidal steady state techniques. This includes describing elements of the circuit with an admittance matrix, adding the admittance matrix of each element to the main admittance matrix, and then solving the resultant system of equations for the voltages and currents. The voltages and currents are then used to determine other parameters of interest such as power loss, stored energy, other reduced equivalent circuit representations, etc. Software has been developed (RESON) to accomplish this step of the analysis.

## **1.7 The Thesis Format**

This dissertation is organized into four parts consisting of 1) introduction and background, 2) development of tools, 3) application, and 4) summary and recommendations. The first part includes chapters 1 - 4 and covers scope, some history, material properties and phenomena, and computer software. The second part includes chapters 5 - 8 which develops, describes, and tests a "toolbox" of techniques for modeling and analyzing rf structures. The third group consists of chapters 9 - 10 that applies some of the techniques described to the modeling and analysis of the K1200 cyclotron rf resonators and compares the results to measurements. Finally, chapter 11 summarizes the results and makes some recommendations for further research.



## CHAPTER TWO

### A Historical Background of RF Structure Analysis

#### 2.1 Introduction

Techniques and associated software, using an equivalent circuit method, have been developed to calculate the performance of high field transverse electromagnetic (TEM) resonators. TEM in this thesis is taken to mean that cross-sections perpendicular to the guided wave axis (referred to as transverse) of the transmission lines in the structure, neglecting losses, have the characteristic that

$$\nabla_t \times \mathbf{E}_t = 0,$$

where the subscripts refer to the "transverse" components.

The techniques developed use a combination of electrostatic numerical analysis and circuit analysis to determine the performance of TEM mode resonators. In theory, a three dimensional numerical analysis code may be used to predict the performance of any rf resonator operating in any mode, whereas the equivalent circuit technique is seemingly limited in scope. In practice, both methods have strengths and weakness.

The advancement, widespread acceptance, adaptation, and affordably of the digital computer has significantly changed the techniques

used for analyzing rf structures. Before digital computers were used to aid in the equivalent circuit analysis of rf structures, the rf structure would be divided into as few elements as possible arranged in as simple a circuit topology as possible so that the circuit response could be determined from either a practical closed-form analysis, or by applying a graphical technique such as a Smith Chart. For complex structures, this would lead to a coarse "back of the envelop" analysis which would then be checked and refined by reduced scale models. When closed form solutions for the circuit elements were not readily available or analytically obtainable, techniques used to determine the electrical characteristics of each element in the circuit model relied heavily on measurement or graphical techniques. Measurement techniques using electrolytic tanks and resistance paper were most often applied. Occasionally, hand generated curvilinear field maps would also be made to determine the electrical parameters of the transmission lines and lumped elements. The experimental techniques have mostly been replaced by computer based techniques that are faster, less labor intensive, and yield similar accuracy .

In the accelerator community, two approaches to the analysis of resonators have been pursued; a finite difference approach and an equivalent circuit approach. The finite difference method describes the structure by a specialized finite difference mesh and then solves the appropriate boundary value problem typically using an over-relaxation method. The equivalent circuit approach segments the structure into sections of equivalent transmission lines and lumped elements which results in an equivalent circuit description of the resonator. The finite difference approach may be applied to both single conductor cavities and

multiple conductor resonators operating in any mode, whereas the equivalent circuit approach is best suited for two or more conductor resonators operating in the transmission line mode. When two conductor resonators without cylindrical symmetry are used, the equivalent circuit approach is typically preferred. Transmission line mode resonators with significant non-cylindrical three dimensional entities are used in the equipment at the NSCL, and hence, the equivalent circuit method of analysis is preferred and emphasized in this research.

## **2.2 Computer Assisted Field Analysis**

The general application of the finite difference approach in the accelerator community largely began with the initial release of the POISSON [2.1] computer program in 1968. The POISSON program is used to numerically solve two dimensional magnetostatic and electrostatic boundary value problems and three dimensional axially symmetric cases. In 1976, building on the foundation of code written for POISSON, a computer program designed to compute the resonant frequencies and electromagnetic fields associated with axially symmetric rf cavities became available named SUPERFISH [2.2] . Although SUPERFISH was directly applicable to a large set of important design problems in the accelerator community, it did not address the problems associated with structures that had significant non-axially symmetric three dimensional aspects. In 1985, a computer program that could be used to compute the resonant frequencies and electromagnetic fields associated with three dimensional structures became available named MAFIA [2.3] . Although written as

general purpose, POISSON, SUPERFISH, and MAFIA are aimed at the class of problems that the accelerator community largely encounters. The programs POISSON, SUPERFISH, and MAFIA are available to the accelerator community for the cost of media and documentation.

Outside of the accelerator community, a great deal of commercial software written for UNIX workstations and personal computers has become available in the last 10 years some of which is applicable to rf cavity analysis. The relevant commercial software emphasizes the application of the finite element method or the boundary element method numerical techniques versus the finite difference techniques emphasized by the programs developed by the accelerator community. The commercial software tends to be expensive so that its use is limited to situations where it is applicable and POISSON, SUPERFISH, and MAFIA are thought to be inadequate. Although written as general purpose, the applicable commercial programs are sometimes aimed at large scale commercial needs such as motor design. The degree to which the commercial programs are applicable to the accelerator community is set by the degree of generality achieved by the program design or by some natural overlap between commercial large scale needs and accelerator needs such as motor magnet design and beamline magnet or accelerator magnet design.

### **2.3 Computer Assisted Circuit Analysis**

Roughly in parallel with the developments in the accelerator community, programs to perform circuit analysis on general circuit

topologies were developed by the electronics community. One of the first programs to be released and used primarily in the educational community in 1971 was CANCER [2.4]. CANCER was followed closely by SPICE [2.5] in 1973 which was destined to evolve into an industry standard. Although these programs included ac sinusoidal circuit response as an available analysis option, they emphasized transient and dc analysis of nonlinear circuits needed for the advanced design and analysis of integrated circuits. Although the ac analysis portions of these programs could be used to determine the frequency response of an equivalent circuit of an rf resonator, the transmission line models used were lossless so that the output of these circuits required further analysis with other programs to determine the circuit losses. Since no automated method existed to move the data from one program to another, each analysis involved a manual and hence time consuming, error prone process to enter the output of one program into the input of the other. As a result, these codes were not commonly adopted for purposes of resonator design and analysis by the accelerator community.

## **2.4 The Equivalent Circuit Technique**

Techniques for generating equivalent circuit representations and using them to analyze and understand the system response have been applied to many diverse types of systems. Examples of systems for which equivalent circuits have been successfully applied include representations for dynamic mechanical systems [2.6], microwave circuits [2.7], and electrical machinery [2.8] to name a few. In this dissertation, an equivalent

circuit technique is applied, and developed as necessary, to the analysis of rf resonators. The equivalent circuit technique is applied here to structures that may be segmented into equivalent transmission line segments that are operating in the transmission line mode. This technique involves resolving the structure into sections of uniform transmission lines and lumped elements.

The equivalent circuit approach to rf resonator modeling and analysis has been applied in various ways long before computers and the associated purely numerical techniques were developed. The techniques used to analyze the resulting circuit as well as the techniques used to determine the electrical characteristics of each of the elements comprising the circuit has evolved over the years. The changes in the application of this technique associated with the application of the computer have been sparsely documented in the literature, although many laboratories, including the NSCL, have developed custom implementations of their own.

The initial computer based circuit analysis techniques applied in the accelerator community limited the complexity of circuit topologies and consisted of writing a unique program for each structure to be analyzed. As structured programming techniques became more common, programs would in large part consist of reusable subroutines which reduced both the lines of new code that needed to be written for each new rf structure to be analyzed and reduced the errors typically encountered when developing new software. The application of general purpose ac circuit analysis software at the NSCL has removed the limitations on circuit topology that the previous techniques imposed.

## **2.5 Advance of the Equivalent Circuit Technique at the NSCL**

In 1985, while designing the K1200 cyclotron, the NSCL rf group headed by this student began to develop code that would automatically generate the SPICE program input based on a combination of electrical and mechanical specifications and read the resulting output for advanced post processing. This project quickly led to a program named RESON which is simply short for RESONator. This name was initially given to a group of BASIC subroutines written and used by the late Jack Riedel to analyze simple resonant circuits. RESON and SPICE ran on VAX VMS computers such as the VAX 11/750. As the personal computer became more powerful, and with the introduction of object oriented programming techniques, RESON was rewritten for the IBM PC and compatibles. SPICE was replaced in RESON by an embedded object oriented ac steady state circuit analysis engine written by this student. The modern RESON has been upgraded many times since and is available free both from the NSCL, and on many bulletin boards which have a technical forum both in the US and in Europe.

Before the equivalent circuit may be solved for the parameters of interest, the electrical parameters of each element of the circuit must be determined. Although closed form solutions for many standard transmission line, capacitor, and inductor designs exist, the problem of determining electrical parameters of non-standard designs remains [2.9]. In many cases, an expression for the characteristic impedance of a particular transmission line may be available while an expression to determine losses is not. Techniques are developed to determine

characteristic impedance and loss characteristics of transmission lines as well as values for lumped elements from electrostatic numerical analysis results.

In 1985, a copy of POISSON written for the VAX VMS system was modified to run on an IBM PC. Code was then written for this version that computed the stored energy in the electrostatic field which was used to determine the capacitance per meter of the geometry being analyzed. For example, if the geometry being analyzed represented a cross-section of a transmission line, then the characteristic impedance of the line may be directly determined from the computed stored energy at the applied voltage. In 1990, a further modification to the POISSON program was made to output a custom data file containing more information than the normal data (dump) files supplied. A new program was written to take the custom data file from the modified version of POISSON and use it to calculate the electrostatic field on the metal boundaries. Using the numerically determined electrostatic field on each conducting boundary in the problem, parameters that are used to determine losses on the line are numerically determined using a technique that will be described in later sections of this dissertation. In addition, the applied voltage and resulting induced charge on each conductor calculated from the electrostatic field is used to determine the capacitance per unit meter. New graphical codes have also been written that simplified investigating and documenting the results of the electrostatic analysis. The techniques and software developed have simplified and expanded the capabilities for parameterizing non-standard circuit elements including transmission lines.



## 2.6 Equivalent Circuit Technique Attributes

Although the computer programs that apply direct numerical techniques to analyze general three dimensional resonators could in theory be applied to cover all possible problems, for large geometrically complex resonators these programs may: 1) exceed the available computer resources, 2) require long computer run times, 3) require significant time and effort to generate and modify the program input during the trial and error design process, 4) require complex additional post processing to determine the voltages and currents in two conductor structures, and 5) typically only determine the response at the resonant frequency. However, these techniques do have the attributes that: 1) the user only needs a basic understanding of field theory sufficient to supply the proper input, 2) techniques exist to determine the error in the analysis with a high degree of mathematical confidence, 3) the accuracy may be improved to a great extent by decreasing the grid size, and 4) the model is valid for waveguide and transmission line structures operating in any modes (i.e. TEM,  $TE_{xy}$ ,  $TM_{xy}$ ).

On the other hand, the equivalent circuit approach applied here: 1) is only applicable directly to two or more conductor structures operating in the transmission line mode, 2) requires the user to have sufficient skill and experience to accurately model the structure, 3) has a topology that is not unique and is therefore arguable, and 4) is dependent on the modeler's skill and experience for determining an accurate circuit topology. However, this technique does have the attributes that 1) it yields the values of voltages and currents directly versus needing integration, 2) it is not limited

to investigating operation at the resonant frequency, 3) once the model is entered, significant modifications to test hypothesis for improving the performance of the structure may be made very rapidly, 4) when it is applicable, it will work regardless of the resonator size or complexity, 5) it requires significantly less computer resources, and 6) it results in significantly shorter computer run times.

## **CHAPTER THREE**

### **Properties of Resonator Materials and Joints**

#### **3.1 Introduction**

The electrical properties of materials and joints and the phenomena of electric breakdown (sparking) are an important concern in high field resonator design. The resonators of immediate concern in this dissertation use copper conductors operating at approximately room temperature in a combination of vacuum, air, and alumina dielectric media.

#### **3.2 Conductors**

The resonator power dissipation due to conduction losses is difficult to predict with good accuracy regardless of the technique used to analyze the resonator. The uncertainty in predicting losses is due to the uncertainty inherent in the physical properties of the materials [3.1], surface properties [3.2], and joints comprising the resonator [3.3].

The conductivity of metals may not match the tabulated values precisely and may be further degraded by the mechanical fabrication of the resonator. It is unclear if the conductivity near the material surface is changed significantly by non-uniform heating associated with hot hammering, rolling, and general forming processes. It is documented that

welds have a different electrical conductivity than would be expected by the material used. Even copper to copper welds formed with copper welding material significantly alter the conductivity of the material from that of the original copper [3.4]. Any deterioration that exists is likely due to a combination of increased surface impurities and lattice deformation.

The resistance of mechanical joints is difficult to predict because it is strongly influenced by the joint pressure, the joint materials, and the design of the mechanical contact surface [3.3]. For tuned resonators, the resonant frequency is typically adjusted by sliding shorting planes that use contact fingers to make the electrical connection. The resistance of the joint formed at the contact surfaces of the fingers is difficult to predict accurately due to fluctuations in contact pressure and contact surface over the area traversed and over time due to wear. For reasonably good contacts, the total resonator loss normally significantly exceeds the total joint losses so that moderate fluctuations over time go unnoticed. It is not unusual for degrading joint conditions to go unnoticed until catastrophic failures occur.

The lack of standard methods to account for possible changes in surface resistance due to mechanical processing clearly leads to unquantifiable error estimates of these quantities. In addition, the method developed later in this chapter that is used to estimate the joint loss has not been tested at these frequencies. As a matter of fact, even when the calculations appear straight forward, it is not unusual for the measured loss to significantly differ from the predictions. Significant research aimed at techniques to make good engineering estimates of the effect of joints and

material forming and joining processes will need to be performed before this situation may be improved.

### 3.2.1 Normal Conductors

For unpolished surfaces seemingly smooth to the touch, rf surface resistance is not affected until the frequencies are into the GHz regime [3.2]. Furthermore, no quantifiable method is known that predicts the degradation in the electrical conductivity near the conductor surface due to mechanical forming and welding processes. Since no practical techniques are known to quantitatively account for the effects of the mechanical processes, the conductivity near the surface will be taken to be either the textbook value or a stated manufacturers value for the bulk conductivity or, equivalently, resistivity.

The resistivity of conductors is given by manufacturers or handbooks at some reference temperature. The resistivity varies linearly with temperature from some reference value at room temperature according to the following formula.

$$\rho(T) = \rho_o(1 + \alpha\Delta T)$$

where

$\rho_o$ ,  $\Delta T$ , and  $\alpha$

represent the resistivity at some reference temperature, the temperature increase, and the temperature coefficient respectively. Table 3.1 lists some values for common materials used in particle accelerators.

Table 3.1 Common Conductor Material Parameters [1.5]

<b>Materials</b>	<b>Resistivity at 20 °C x10<sup>-6</sup> Ohm-cm</b>	<b>Resistivity Ratio to Copper</b>	<b>Temperature Coefficient °C<sup>-1</sup></b>
Aluminum	2.62	1.52	0.0049
Brass	3.9	2.26	0.002
Carbon (graphite)	1400	812.02	-0.0005
Chromium	2.6	1.51	
Copper	1.7241	1.00	0.0039
Gold	2.44	1.42	0.0034
Indium	9	5.22	0.00498
Iron	9.71	5.63	0.0052-0.0062
Magnesium	4.46	2.59	0.004
Molybdenum	4.77	2.77	0.0033
Nickel	6.9	4.00	0.0047
Silver	1.62	0.94	0.0038
Steel	13-22	12.76	0.003
Stainless Steel	90	52.20	
Tantalum	13.1	7.60	0.003
Titanium	47.8	27.72	
Tin	11.4	6.61	0.0042
Zinc	6	3.48	0.0037

At sufficiently low temperatures, the rf resistivity varies according to the "anomalous effect" [3.6, 3.7]. This effect causes the resistivity to maintain a higher value than would be predicted by the simple linear formula described. The anomalous skin effect becomes dominant when the electron mean free path becomes proportional to the rf skin depth. The formula for the anomalous rf surface resistance that determines the lower bound of the surface resistance is

$$R_s = \left( \frac{2l}{3\sigma} \right)^{\frac{1}{3}} \left( \frac{\omega\mu_o}{2} \right)^{\frac{2}{3}},$$

where " $l$ " is the electron mean free path. In addition to normal conductors, superconducting resonators may also be analyzed, in some cases, with the techniques described in this dissertation. A review of the properties of superconducting resonators was made at the NSCL in 1992 [3.7].

### 3.2.2 Skin Depth

The current tends to flow very near the surface at high frequencies due to the "Skin Effect". In a good conductor, the high frequency electric and magnetic field decay exponentially as they penetrate the surface of the conductor. The "Skin Depth" is defined as the depth in the conductor where the fields have decreased to  $1/e$  of the value at the surface. The formula for the skin depth in a good conductor is:

$$\delta = \frac{1}{\sqrt{\pi f \mu \sigma}}$$

A conservative estimate of the rf surface resistance can be made by assuming the total rf current flows uniformly in a surface layer of thickness  $\delta$ . The following formula for the rf surface resistance is calculated based on the skin depth.

$$R = \frac{L}{\sigma A} = \frac{L}{\sigma \delta w} = \sqrt{\frac{\omega \mu}{2\sigma}} \frac{L}{w} \equiv R_s \frac{L}{w}$$

The width " $w$ " in the above expression may be the actual geometric width if the current density is uniform or an equivalent width " $w_e$ ", that will be described in chapter seven, if the current is not uniform.  $R_s$  in the expression is called the "Surface Resistance", or is sometimes referred to

as "Ohms per Square" since a square surface in any measure has a net resistance  $R_s$ .

### **3.3 RF Joint Resistance**

Joints consist of both bolted joints and joints formed with contact fingers. The bolted joints maintain a great deal more pressure on the contact surface than do the finger joints. Finger joints are used where bolted joints cannot be used for mechanical reasons or where a movable joint is needed for resonator tuning. The cyclotron resonators are tuned with large tuning stems whose lengths are adjusted with a sliding short that uses contact fingers. A reasonable estimate may be made for bolted joint resistance based on extrapolations from data obtained from research performed by the Parker Seal Company [3.3]. However, the same research leads to excessive estimates of finger contact resistance because of the low contact pressure. For finger contacts, measurements made at the NSCL are used as a upper bound of the finger contact resistance. The NSCL measurements of the finger contact resistance in combination with the research from the Parker Seal Company for bolted joint resistance form a upper and lower bound for the possible finger resistance.

A method for estimating joint losses based on research that was performed at the Parker Seal Company is developed in this section. The research measured the resistance of joints in RG-53/U waveguide for various types of seals. The measurements were made using a specially designed apparatus that allowed them to place the seal in a resonant cavity either at a current null or maximum by moving two sliding shorts without



disturbing the seal. The difference in resonator loss between the two conditions is a measure of the seal insertion loss. In addition, the joint resistance as a function of flange bolt torque was also measured. The results for various seal materials and seal designs are expressed in terms of an equivalent joint resistance. These measurements were made for a flange force of 1000 pounds per linear inch.

In order to make use of this information, the joint resistance must be transformed from Ohms, denoted as  $R_f$ , to Ohm-cm denoted as  $R_j$ . Assuming the leakage from the joint is negligible, all of the insertion loss can be attributed to conduction loss. The total flange resistance is related to the power dissipated by

$$P_f = \frac{I_o^2 R_f}{2} \quad \text{where } I_o = \int_0^l |K_z| dl,$$

where  $K_z$  denotes the surface current density with units of A/m.

The same losses can be determined using Ohm-cm as

$$P_f = \frac{R_j}{2} \int_0^l |K_z|^2 dl.$$

Equating the two expressions yields

$$R_j = R_f \frac{\left[ \int_0^l |K_z| dl \right]^2}{\int_0^l |K_z|^2 dl}.$$

The measurements were made by Parker Seal Co. for a  $TE_{01}$  mode in a rectangular guide. The current density of this mode for a waveguide of

width "a" placed along the "x" direction in Cartesian coordinates may be expressed as:

$$K_z = H_o \sin\left(\frac{\pi x}{a}\right)$$

Using the above expression for the current density in the previous expression for  $R_j$  and multiplying by 1/2 yields:

$$R_j = \frac{1}{2} \left(\frac{4}{\pi}\right)^2 a R_f.$$

The 1/2 is inserted in the above expression because a seal consists of two series joints. The experimental data from Parker Seal Co. is for WR-284 waveguide. For WR-284 waveguide, the width is  $a = 7.2136$  cm. Using this value for "a" in the above expression leads to  $R_j = 5.84 R_f$  Ohm-cm.

Using this expression and the data from the research at 2.6 GHz,  $R_j$  varies from 0.0293 to 0.2048 Ohm-cm from best to worse case. The best case is the limit of measurement (which some specially designed seals exceeded), whereas, the worse case was for a conductive plastic seal. For reference, an anodized die cast Aluminum seal yields  $R_j = 0.0631$  Ohm-cm. The resistance values are a function of frequency. The data takes the form of straight lines with a positive slope on a log-linear plot of  $R_j$  versus frequency from 2.8 to 3.95 GHz. Table 3.2 table summarizes the results.

Table 3.2 Seal Resistance versus Frequency

<b>f (MHz)</b>	<b>R<sub>f</sub> Conductive Plastics</b>	<b>R<sub>f</sub> Impregnated Wire Mesh</b>	<b>R<sub>f</sub> Die Cast Aluminum (Anodized)</b>	<b>R<sub>f</sub> Limit of Measurement Reliability</b>
2600	0.04	0.02	0.0108	0.01
3100	0.09	0.08	0.0206	0.01
3650	0.24	0.2	0.045	0.02

The above data for the die cast aluminum seal fits

$$R_j(f) = 5.84 \times 0.0108 \times 10^{5.9 \times 10^{-4}(f-2600)} \Omega \cdot cm$$

with  $f$  expressed in MHz. The anodized Aluminum seal result will be used as the bolted joint value for this work since it is the most conservative of the metal seals.

For bolted joints and the anodized Aluminum seal, the data yields  $R_j = 0.00192$  Ohm-cm at 30 MHz and  $0.00187$  Ohm-cm at 9 MHz. Since these numbers are so close to one another, and the uncertainty is great, the joint resistance for bolted joints will be taken to be  $0.00190$  Ohm-cm and constant for bolted joints in this work. The number must be doubled if the bolted joint contains a seal since two joints then exist. The above resistance was obtained for a seal force of 1000 pounds per linear inch which corresponds to 4000 pounds per square inch (PSI) for a 1/4 inch wide flat seal. The joint pressure will be taken to be 4000 PSI for all bolted joints comprising the K1200 rf resonator.

For movable joints consisting of contact fingers, the joint pressure is much less. The fingers used at the NSCL are shown in figure 3.1. They are specially manufactured for the NSCL by Instrument Specialties Company. The ball which comprises the contact surface is composed of a 99% silver and 1% carbon graphite mixture. The fingers are silver plated to a thickness of 0.0019 cm. The contact surface of the ball appears as a circular flattened region after a nominal break-in period. The normal finger deflection requires about 10 oz. of force. Because of the variation in wear (flat spot size) and deflection tolerance, these nominal numbers results in a pressure of 150 to 500 PSI on the contact surface.

The available data from the Parker Seal Company Research for the variation in joint resistance due to joint pressure ends at 1000 PSI. 1000 PSI results in an increase in resistance by approximately a factor of 25 from the 4000 PSI joint pressure. This leads to a finger joint resistance of  $R_j = .0475$  Ohm-cm. There exists 5 fingers per linear inch. If each finger flattened contact area is taken to be circular with a 0.04 inch diameter, this leads to a linear contact surface of 0.628 inches per inch. (The current is assumed to flow onto the finger uniformly around the contact circle.) This increases the resistance to  $R_j = 0.0475/0.628 = 0.0756$  Ohm-cm.

This value for the joint resistance of the contact fingers leads to a power dissipation that exceeds our experience. In particular, the K1200 tuning stem sliding short carries approximately 4000  $A_{rms}$  at 26.5 MHz. This results in each finger carrying about 39  $A_{rms}$ . The inner conductor has a diameter of 8 inches, leading to the finger joint resistance being 0.001184 Ohms. The power dissipated would then be 18,950 kW, or 151.6 Watts per

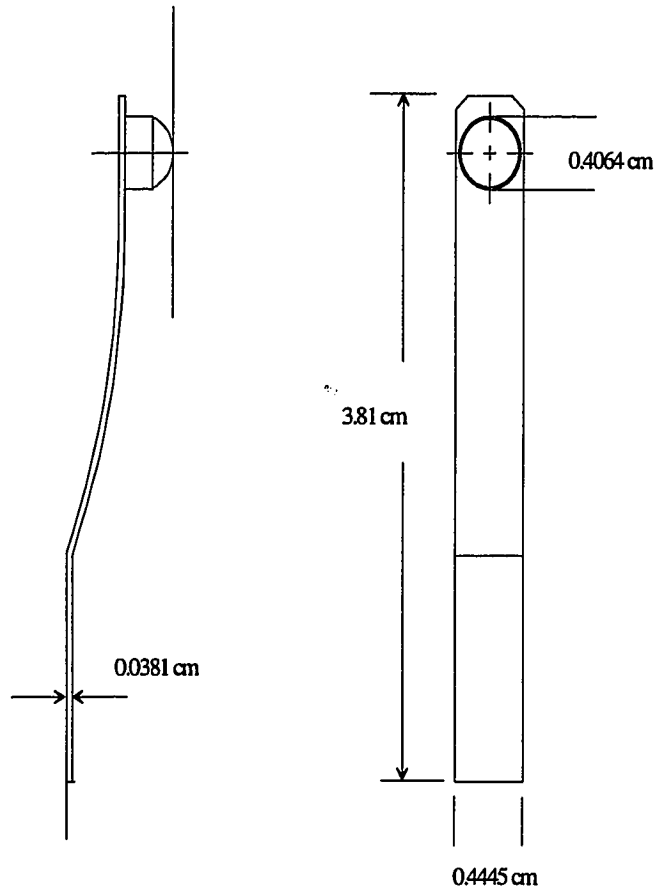


Figure 3.1 The NSCL finger contacts for sliding joints.

finger, which does not match our experience. As a result, measurements were made to determine an appropriate value.

In 1985, an apparatus was built to test the feasibility of using these fingers for the K1200 tuning stem. The device consisted of a 30 MHz quarter wave coaxial resonator. The device is 11.4 centimeters in diameter and 250 centimeters long. An adjustable capacitive coupling exists on the high voltage end and a single finger makes the electrical short at the high current end. A voltage monitor 13.335 cm from the short is used to determine the current in the short. For a current of 42 Arms, we measured a finger temperature rise of 40 °C in still air. Since this is about the maximum current the K1200 would need to hold per finger, this result was used to justify using these fingers as the electrical contact of the sliding tuning short. It takes about 50 Watts of power to drive the test resonator to achieve this finger current, much of which may be easily attributed to resonator losses and radiation. Clearly this is much less than the 150 Watts per finger the previous value of joint resistance would predict for a current of 39  $A_{rms}$ .

After having seen the joint resistance for the fingers extrapolated from the research, I elected to again set up the finger tester and retake the measurements made in 1985. The apparatus has a serious problem with radiation, so that accurate determinations of the finger resistance are not possible without extensive changes. However, if after subtracting the calculated losses in the resonator surfaces, the remaining power needed to drive the resonator is attributed to finger losses, the finger resistance is found to be about 5 times less than the predicted value would suggest. This is clearly a very conservative estimate because the significant loss of

power due to radiation is included as part of the finger loss. The measured value yields a result of 0.0304 Ohms per finger. There exist 5 fingers per inch leading to a contact resistance of 0.015 Ohm-cm. This number forms an upper bound to the finger joint resistance. Since the contact pressure may vary significantly, the actual resistance likely has a range of values versus a particular value.

In conclusion, bolted joint resistance will be handled by assuming an extension of research that was performed at the Parker Seal company at 2.6 to 4 GHz. The extension leads to using  $R_j = 0.0019$  Ohm-cm for all bolted joints. In addition, the NSCL sliding contact fingers will be taken to be bounded by 0.0019 to 0.015 Ohm-cm based on the Parker Seal Research and the NSCL measurements. The finger resistance will initially be set to 0.015 Ohm-cm in the simulations and then adjusted if necessary, within the set bounds, to match measurements.

### **3.4 Insulators**

Insulators considered in this section include, alumina, vacuum, and air. The alumina is normally used as the interface between the air and vacuum sides of the resonator. An insulator serving as a dielectric interface between vacuum and air is typically referred to as a "vacuum window".

### 3.4.1 Electrical Characteristics of Vacuum

#### 3.4.1.1 Breakdown

Many different theories have been proposed to attempt to accurately predict at what field levels a vacuum insulated device will flash over. It is generally accepted that 100 kV/cm (corresponding to the sparking point for dc conditions and a 1 cm gap) is a practically attainable value without any special surface treatments. The theory which seems most usable for purposes of this dissertation is one that was proposed by Kilpatrick [3.8].

The "Kilpatrick Criterion" relates the particle impact energy to the surface gradient at the cathode. The particle impact energy is a measure of peak applied potential and the particle motion dynamics. It is normally assumed that the particle gains kinetic energy equal to the peak gap potential. Electrons and hydrogen ions are thought to be the dominant particles involved in sparking in vacuum. For a particular range of charged particles considered in a rf field operating over a particular frequency band, the particle may not attain the full impact energy equal to the gap potential due to transit-time factors. As a result, for these conditions higher gradients than the dc value are obtainable before breakdown.

The Kilpatrick criterion was empirically derived from a mixture of known and applied functional relationships in combination with measurements taken on operating equipment without any special surface treatments. The criterion matches experimental data for  $10^{-5} < \text{gap} < 10 \text{ cm}$ ,  $0 < \text{voltage} < 1.2 \times 10^6 \text{ volts}$ ,  $9 \times 10^4 < \text{surface gradient} < 8 \times 10^7 \text{ volts/cm}$ , and  $\text{dc} < \text{frequency} < 3 \times 10^9 \text{ Hz}$ .



The empirical relation arrived at for the dc limit is:

$$WE^2 e^{-\frac{1.7 \times 10^5}{E}} \leq 1.8 \times 10^{14}$$

In the above relation, E is in the electric field intensity at the cathode surface expressed in volts/cm and W is the impact energy expressed in electron volts. For a impact energy of 100 keV (Vdc = 100 kV), the criteria predicts about 100 kV/cm to be the maximum allowable cathode field before sparking will occur.

#### 3.4.1.2 Multipactoring

Multipactoring is an electron resonance phenomena associated with rf fields in vacuum [3.9]. In its simplest form, it may be described as a electron oscillating between two metal plates to which an rf voltage is applied. For example, if an electron is synchronous with the rf field it will leave the first plate at a phase angle with respect to the rf of 0 degrees, arrive at the other plate at a phase angle of 180 degrees, and then return at a phase angle of 360 degrees.

For the electron to remain synchronized with the applied field, it must loose energy at each rebound. The electron may loose energy by some combination of applying heat to the plates, x-ray production due to bremsstrahlung , releasing another bound electron (secondary electron emission), or loosing synchronization with the applied field. For multipactoring to cause a build up of electrons, the electron secondary emission of the conductors must be greater than one.

Based on the above discussion, multipactoring is a non-linear phenomena since its occurrence is dependent on both frequency and field amplitude. In order to prevent the build up of electrons, it is necessary to pass through the "multipactoring zone" quickly before a build up of electrons causes the field to be effectively clamped to some optimum multipactoring potential.

At some constant applied potential, multipactoring will occur at odd harmonics of the fundamental applied frequency. If the amplitude is also allowed to vary, and a range of starting phase is allowed, then harmonically related "Multipactoring Zones" are encountered [3.9]. In other words, instead of a given multipactoring optimum voltage at a some frequency, there exists a range of voltage for which multipactoring can exist.

In addition to the simple parallel plate model of multipactoring described, when insulators are used that have secondary emission coefficients greater than one, single surface multipactoring may exist [3.10]. This type of multipactoring is caused by the insulator surface charging which attracts electrons back to it. A combination of 1) having a certain applied rf field amplitude and frequency, 2) the secondary electron emission being greater than one, and 3) a dc field building up due to electrons being expelled from the surface, leads to single surface multipactoring. The K1200 dee stem insulators show signs of what may be due to episodes of single surface multipactoring by displaying characteristic patterns of spots as shown in the literature.

### **3.4.1.3 X-ray Production**

Free charged particles exist in imperfect vacuum. These particles, primarily electrons, are accelerated by applied electric fields. When these particles collide with the surfaces of the structure, they experience a sudden deceleration leading to x-ray production (bremsstrahlung). At sufficiently high voltages, the x-rays produced can penetrate the surrounding walls and at high enough intensities may become a health hazard. Since the portions of the K1200 cyclotron rf resonators that are vacuum insulated are deeply embedded in the iron yoke, no hazard exists since the iron forms an effective shield. However, the x-rays may influence the performance of vacuum window material as described in the next section.

### **3.4.1.4 Vacuum Windows**

Alumina vacuum windows are used on the K1200 cyclotron for both the rf input coupler and the dee stem insulators. These insulators have a secondary electron emission of 2 to 9 over a broad range of impact energy. In addition, informal measurements at the NSCL indicate that they are very sensitive to photoemission in the presence of photonic radiation of  $> 2$  eV. Measurements indicate that the insulator can charge rapidly in the presence of this radiation, particularly when electric fields exist to draw away the resulting photoelectrons. Untreated alumina insulators tend to charge to a saturation value that is not understood and then take in excess of 12 hours to return to normal. Although it is generally believed that

multipactoring is the dominant reason for vacuum window failures, charging of the insulator by photonic radiation in the presence of high fields may also be a factor. Our experience indicates that when insulators are shielded from line of sight of high fields, they operate more reliably.

Alumina insulators may be treated to reduce the secondary electron emission and the recovery time from photonic charging. Two methods are known to this student. The most commonly applied technique involves applying a few Angstroms coating of titanium-nitride to the vacuum side surface of the insulator. This has been shown to prevent damage to vacuum windows of high power klystrons as an example. The method is thought to reduce the secondary electron emission of the alumina down to that of the titanium, which is less than one, as well as allow a discharge path while not radically reducing the rf Q of the material. The titanium tends to evaporate off in time requiring retreatment. The other treatment referred to as "graying" involves a high temperature treatment of the insulator in a vacuum furnace near the sintering temperature [3.11]. This process will give a creamy white alumina insulator an off-white or gray color throughout its volume. A pink alumina insulator become dark gray deep into the surface. This technique does not wear off in time and has seemingly the same effects as the titanium treatments based on the unpublished measurements and operating experience of the NSCL.

In conclusion, photonic charging and multipactoring are most likely the dominant destruction mechanisms in vacuum windows. A combination of 1) treating the insulator to lower the secondary electron emission coefficient and allow the induced charge to bleed off and 2) keeping the insulator away from line-of-sight to any high voltages that may produce

x-rays leading to insulator charging corrects the problem. Evidence in the K1200 cyclotron indicates we experience significantly fewer failures when these processes are performed.

### **3.4.2 Electrical Characteristics of Air**

Breakdown curves for spark gaps consisting of polished balls of various diameter are given in the literature [1.5] For purposes of this thesis, air will be taken to break into corona and become prone to complete breakdown when the fields on the surface of the cathode are greater than or equal to 30 kV/cm. It is normally good practice to keep air flow past surfaces close to these values to prevent a build up of conductive gases such as  $O^3$ , which can cause breakdowns. If the high voltage is applied with a current limited power supply, these type of breakdowns typically manifest themselves into relaxation oscillations.

## **CHAPTER FOUR**

### **Computer Software**

#### **4.1 Introduction**

Both commercial and specially written software is used for the work done in this dissertation. All of the software is run on Intel based IBM compatible Personal Computers (PC). Two computers were used, a Intel 90 MHz/32 MB Pentium computer in my office and a 100 MHz/16 MB Intel Pentium computer in my home. Both of these computers use the Windows 95 operating system from Microsoft Corporation. The computers are networked together on the Internet to allow for the efficient transfer of information used in this research between my home and office. The office computer is connected to the network through a 10 Mbps Ethernet connection and the computer in my home via a 28.8 kbps telephone modem.

The dissertation is written using the AMI PRO version 3.1 word processor from Lotus Development Corporation. Mechanical drawings are done using Microstation version 5.0 software from Bentley Computer Systems and Autosketch version 2.0 and AutoCad version 12.0 from Autodesk corporation. Much of the data was stored, analyzed, and plotted with the Excel version 5.0 spreadsheet software from Microsoft Corporation. The specially written software is written in Borland Pascal

version 7.0 or Borland Delphi version 1.0 from Borland International, Inc.. The electrostatic analysis is performed with COSMOS version 1.71C from Structural Design and Research Corporation. The closed-form solutions were studied and plotted with MathCad version 6.0 from MathSoft Inc.. The circuit simulation is performed with RESON version 1.3 written by a co-worker and I. Some software was also specially written by me to either generate nearly repetitive input models for RESON cases or to post process output from COSMOS.

## **4.2 Electrostatic Analysis Software**

Originally, a heavily modified free version of the Poisson computer program was used to perform the electrostatic analysis as described in chapter two. Recently a version of COSMOS using advanced finite element analysis techniques has become available at reduced cost to educational institutions for the Windows 95 operating system. A copy of this software was obtained and found to be more suitable and stable than the previous software, so it was decided to use it instead.

### **4.2.1 The COSMOS Finite Element Software Package.**

The COSMOS software consists of modules to perform different functions or types of analysis. The modules are purchased separately or in groups. The GEOSTAR module is used to draw or import geometry from CAD systems and has extensive automeshing capability. The module ESTAR is used to perform the electrostatic analysis on the finite element mesh and associated boundary conditions output from GEOSTAR. The

user converses with the program modules through a single complimentary menu and command line based user interface.

The input to the program was either drawn directly with GEOSTAR (rarely) or was imported from a file, formatted in the DXF graphics format, generated by the Mechanical Design department and then edited with GEOSTAR. The editing involved removing unnecessary geometric entities and grouping the remaining geometric entities as needed into advanced interrelated geometric entities. The geometric entities in GEOSTAR include points, curves, contours, surfaces, and regions. The editing involved arranging the "curves" into closed "contours" which were used as boundaries to define one or more "regions" to be meshed and analyzed. The region defined is then automeshed with quadrilateral finite elements with a user defined granularity that the program increases as needed for places within the region that have a rapidly changing geometry. All of the geometric or mesh entities may be plotted at any time to ensure the program has interpreted the commands as intended.

Once the geometry is entered, interpreted, and meshed, boundary conditions and material properties are applied in preparation for the ensuing analysis. Boundary conditions may be put on any physical entity, such as a point, curve, contour, node, or region. The Dirichlet (constant potential) or Neumann (symmetry condition: the partial derivative of the potential normal to the boundary forced to zero) may be applied. The boundaries default to Neumann type. Once the boundary conditions are specified, the analysis is performed and many outputs are available including plots and lists of potentials, node locations, plots and lists of electric fields, etc. on any of the user specified geometric entities or mesh nodes.



The plots of electric fields and constant potential contours that appear in the thesis were generated and output from COSMOS to files in the DXF graphics format. The DXF files were input with Autosketch, edited to remove any stray effects, and copied to the windows clipboard in a Windows Metafile format (WMF). The contents of the clipboard were pasted into AMI PRO's embedded drawing package for additional editing as needed and entry into the dissertation.

The values of the electric fields on the boundaries were output to ASCII text files by COSMOS and then imported to a Excel spreadsheet. The data was then rearranged as needed and output to multiple dBase format database files in preparation for being input by the specially written software for post processing. The dBase format was chosen because it was easily input by Delphi programs in preparation for post processing.

#### **4.2.2 Custom Written Software**

The specially written software used to post process the results of the electrostatic analysis was written with Delphi. Delphi was chosen because it is a so-called 4<sup>th</sup> generation development environment that generates the code for the user interface objects based on simple user interaction. It also contains objects to read dBase type databases.

The program read the electric field data from the dBase files previously described and applied the formulas for nonstandard transmission lines developed in chapter seven. Since the data output by COSMOS is arranged in node order, versus in point order along each boundary, the data was first sorted into boundary point order to facilitate the ensuing integrals. Once the data was sorted into the needed order, the

integrations necessary to determine the equivalent width ( $w_e$ ) of each boundary as described in chapter 7 were determined. The program also calculates the induced charge on each boundary and the boundary length. A simple trapezoidal algorithm was used to perform the integrations. The resultant program data was output to ASCII files. In addition, comparing the capacitance of the structures per unit length based on the stored charge on each boundary to the value obtained from the stored energy calculated by COSMOS provided a good check on the accuracy of the post processing algorithms.

### **4.2.3 Some Known Test Cases**

To help gauge the accuracy of the programs, four test cases are evaluated. The mesh density is held constant, and no special mesh generating algorithms are applied to take advantage of the circular symmetry. The four test case are coaxial cable cross-sections of 25, 50, 100, and 200 Ohms. The equal potential plots are shown in figure 4.1. The comparison of the calculations with the known values are tabulated in table 4.1. The error in outer conductor equivalent width vary from 0 to 0.64 %, inner conductor equivalent width from 0.04 to 0.69 % and error in  $Z_o$  from -0.69 to 0.08%. It should be emphasized that the solution accuracy could have been increased by reducing the mesh size, however, the goal was to measure the effects of the relative mesh size which would be used to solve the actual problems.

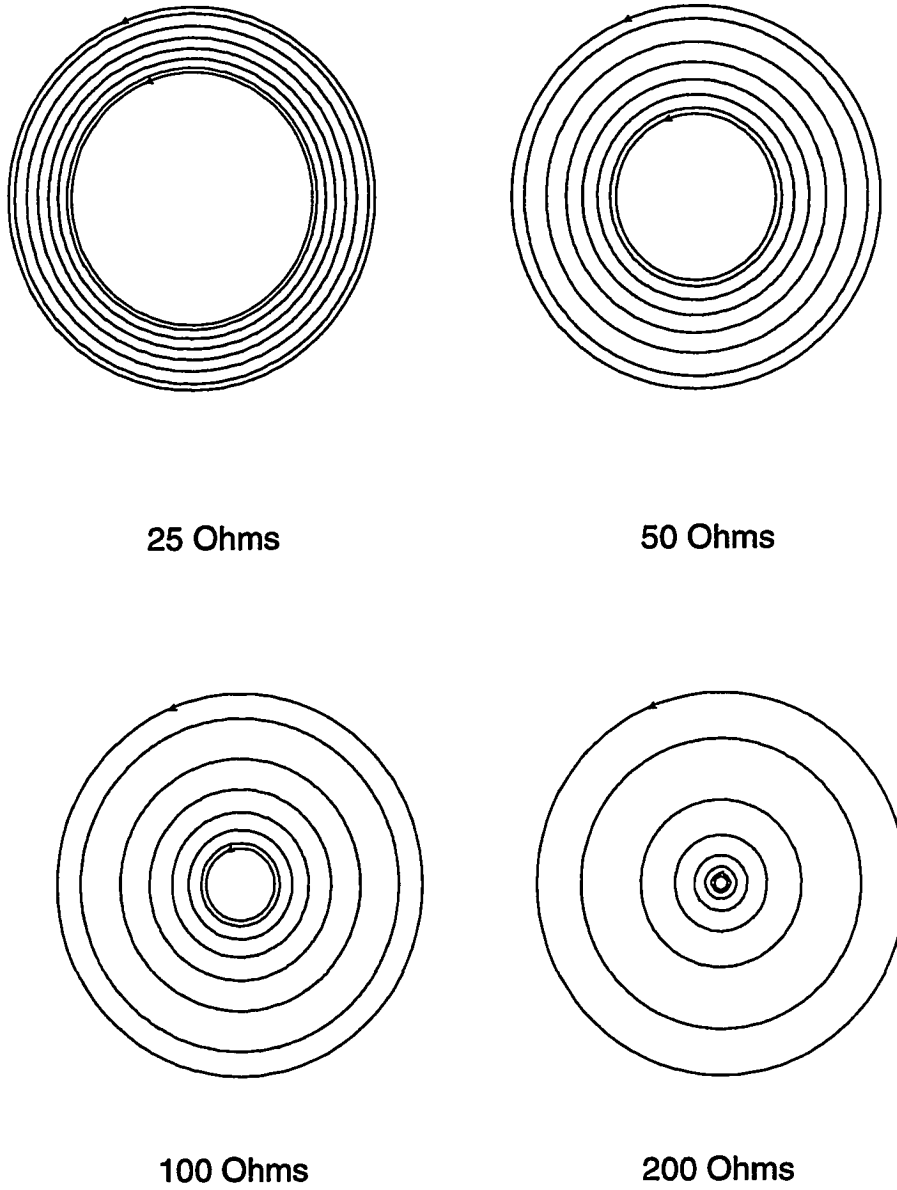


**Figure 4.1** Four numerically analyzed coaxial test cases using COSMOS.

Table 4.1 Four Coaxial Test Cases

<b>Axtual <math>Z_0</math> (Ohms)</b>	<b>Numerical <math>Z_0</math> (Ohms)</b>	<b>Actual inner conductor <math>w_e</math> (cm)</b>	<b>Numerical Inner Conductor <math>w_e</math> (cm)</b>	<b>Actual Outer Conductor <math>w_e</math> (cm)</b>	<b>Numerical Outer Conductor <math>w_e</math> (cm)</b>
25	24.97	6.28	6.26	9.53	9.45
50	49.98	6.28	6.26	14.45	14.38
100	100.08	3.14	3.12	16.65	16.57
200	198.63	0.5	0.5	14.45	14.39

### 4.3 RESON : RF AC Circuit Analysis Software

RESON is a ac circuit analysis program based loosely on SPICE. It is optimized for rf circuit analysis, since beyond solving for currents and voltages, it also solves for power, stored electric energy, and stored magnetic energy. The program also has enhanced input and output functions. The program input and output is through ASCII data files. The input file format looks similar to SPICE input files.

The program is written in Borland Pascal version 7.0 for the MS-DOS operating system. The ASCII file based user I/O was written by a co-worker, John Priller, while the computational, data management, and circuit analysis engine was written by me. The program is distributed free on many computer bulletin boards as well as through other means such as engineering software packages shipped on CD ROM.

The portion of the software that does the analysis is written with an object oriented analysis engine. The details of the available circuit

elements and available I/O functions and report formats are available in the manual [4.1]. The program manages and solves the matrix equation

$$\mathbf{I} = \mathbf{YV},$$

where  $\mathbf{I}$  is the  $n \times 1$  current vector,  $\mathbf{Y}$  is the  $n \times n$  admittance matrix, and  $\mathbf{V}$  is the  $n \times 1$  voltage vector. Each element has a local admittance matrix whose rows and columns correspond to the terminals of the element. The main admittance matrix rows and columns corresponds to the nodes of the main circuit. An element is added to the main circuit by adding the elements of the local admittance matrix to the main admittance matrix such that the local admittance matrix terminal indices are replaced by the corresponding main admittance matrix node indices.

Memory is allocated dynamically so that the problem size is limited to the available memory. The current version of the program is limited by the MS-DOS program space that is less than 640 kBytes. Problems have been tested up to 200 nodes in this environment. A 32 bit version of the program is planned to increase processing speed and problem size by making better use of the current 32 bit computer technology.

#### **4.3.1 Custom Written Software**

Two programs written in Delphi were designed to create RESON input files based on user specifications for linear and logarithmic tapers. These programs are used to generate the large input files needed for the 300 - 500 RESON runs that were needed to validate the developed theory for handling non-uniform transmission lines presented in chapter eight.

### 4.3.2 The General Admittance Matrix for Transmission Lines

Most of the admittance matrices for common elements are either easily derivable or available in the literature [4.2]. All of the transmission lines in RESON inherit the general transmission line object. Since the proper implementation of this element is central to this dissertation, it is appropriate to describe the details here. The transmission line in RESON is a three terminal device. It can be envisioned as a ring, with one of the three conductors common to both ends. If a four terminal device is needed, it may be constructed with two, three-terminal devices. Figure 4.2 displays the circuit aspects of the model.

In RESON, the materials are all treated as isotropic and linear. The materials include both dielectric and permeable types. The dielectric materials are described by a dielectric constant

$$\epsilon = \epsilon_0 \epsilon_r \text{ with } \epsilon_0 \cong 8.854 \times 10^{-12} \frac{F}{m} \text{ and } \epsilon_r \geq 1$$

and the material "Q<sub>e</sub>" which relates the stored electric energy to the electric energy dissipated per cycle

$$Q_e = \frac{\omega C}{G}$$

where C is the capacitance per meter and G is the conductance per meter. The permeable materials are described by a permeability

$$\mu = \mu_0 \mu_r \text{ with } \mu_0 = 4\pi \times 10^{-7} \frac{H}{m} \text{ and } \mu_r \geq 1$$

and the material " $Q_h$ " which relates the stored magnetic energy to the magnetic energy dissipated per cycle

$$Q_h = \frac{\omega L}{R_h}$$

where  $L$  is the inductance per meter and  $R_h$  is a series resistance per meter. An additional resistance per meter is needed to account for the conduction losses of each conductor is denoted by  $R_c$ .

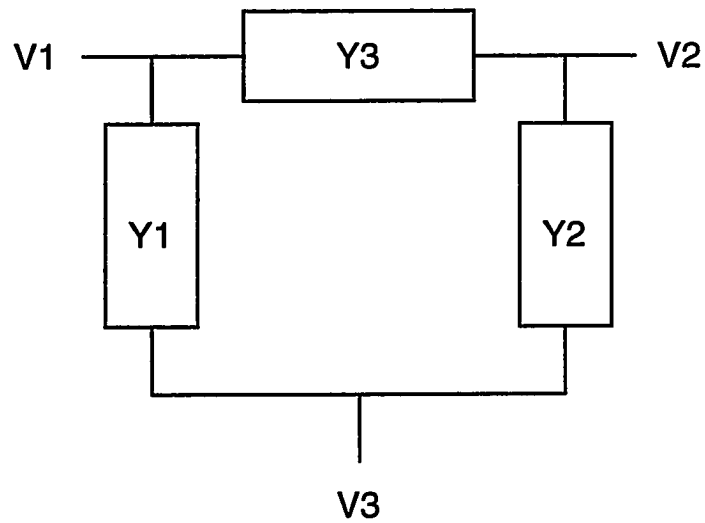
$$R_c = R_s \left( \frac{1}{w_{e1}} + \frac{1}{w_{e2}} \right),$$

where  $w_{e1}$  and  $w_{e2}$  are equivalent conductor widths for each conductor that will be described in chapter 7, and  $R_s$  is the normal rf surface resistance described in chapter 3.

A perturbation method is used to determine the parameters of the transmission line. The line is initially assumed to be lossless and the lossless values for  $Z_o$ ,  $L$ , and  $C$  are determined in the conventional way for the particular geometry. These parameters are then combined with the electrical loss parameters of the line.

$$G = \frac{\omega C}{Q_e}, \quad R = R_c + \frac{\omega L}{Q_h}$$

The values are then used in the expressions listed in figure 4.2 to establish the wave-number and the new (perturbed) value of  $Z_o$ .



The Circuit Model

$$Y = \begin{bmatrix} Y1 + Y3 & -Y3 & -Y1 \\ -Y3 & Y2 + Y3 & -Y2 \\ -Y1 & -Y2 & Y1 + Y3 \end{bmatrix}$$

The Associated Admittance Matrix

$$Y1 = \frac{\tanh(\gamma l)}{Z_o}, \quad Y2 = Y1, \quad Y3 = \frac{1}{Z_o \sinh(\gamma l)}$$

$$\gamma = \alpha + j\beta = \sqrt{(R + j\omega L)(G + j\omega C)}, \quad Z_o = \sqrt{\frac{R + j\omega L}{G + j\omega C}}$$

Figure 4.2 The general transmission line circuit model.



### 4.3.3 A Simple RESON Test Case

A simple quarter-wave coaxial resonator is simulated and the results compared against a solved example described by Hayt [4.3]. The example resonator has an inner conductor of 1 cm radius, an outer conductor of 2.72 cm radius, a length of 37.5 cm, and is loaded with a material with dielectric constant of 10. The conductors are silver and the dielectric material has a dielectric material quality factor ( $Q_e$ ) of 1000. Table 4.2 tabulates the results . Figure 4.3 contains the computer input file to RESON, and figure 4.4 the output report from RESON for a operating voltage of 2 Volts peak. The numbers from the two calculations are nearly identical. For reference, the dielectric power dissipated is 52.4  $\mu\text{W}$ , the inner conductor 16.8  $\mu\text{W}$ , the outer conductor 6.2  $\mu\text{W}$ , and the end plate (annulus) is 0.9  $\mu\text{W}$ .

Table 4.2 Closed Form Calculations versus RESON Predictions for a Coaxial Resonator

	<b>Closed Form Calculation</b>	<b>RESON Calculation</b>
<b>Resonant Frequency (MHz)</b>	100	100
<b>Equivalent Shunt Resistance (Ohms)</b>	26,200	26,260
<b>Equivalent Shunt Capacitance (pF)</b>	41.7	41.7
<b>Equivalent Shunt Inductance (nH)</b>	60.7	60.7

```

* Hayt Test Line ( 01/10/96, John Vincent )
*
* Defines a quarter-wave coaxial resonator, with
* ra = 1 cm, rb = 2.72 cm, l = 37.5 cm,
* epsr = 4, mur = 1, Qe = 1000.
*
* Should result in Rs = 26,200, Cs = 41.7 pF, Ls = 60.7 nH, Q = 687
*       Power Loss = 76.3 uW, with distribution
*       dielectric = 52.4 uW, center conductor = 16.8 uW,
*       outer conductor = 6.2 uW, end plate = 0.9 uW
*
* define the units
*
.UNIT MILLIMETER
*
.MAT=SILVER
*
* shunt drive
*
I1 1 0 0.000053841 0.0
*
Cin 1 0 1.0E-16 ; must have two connections to every node
*
* The Coaxial Transmission Line
*
TC01 1 2 0 Ri=10.0 Ro=27.2 L=375 E=4 QE=1000
*
* The Annulus
*
AN1 2 3 Ri=10.0 Ro=27.2
*
* The Short
*
Vshort 3 0 0.0 0.0
*
* The analysis to be performed
*
.AC LIN 20 99.99E+6 100.01E+6
*
* The Output
*
.PRINT AC VM(1,0) IM(Vshort)
.REPORT AC 100.00E+6

.OUTPUT 1 "Results at 108 Mhz for Min C " I T A $ P Pc Pe Ut Q
.SHUNT 1 " Results at 108 Mhz for Min C " 1
.COUPLE 1 " Results at 108 Mhz for Min C " node=1 Z0=50

```

Figure 4.3 The RESON input file for an example coaxial resonator.

```
"Report File: ", "HAYT.1"  
  
"Report Title:", ""  
"Frequency (hz):", 100.000E+06  
  
"Output:", "Results at 108 Mhz for Min C "  
  
"LABEL", "P", "PC", "PE", "UT"  
  
"I1", -76.15E-06, -76.15E-06, 0.000E+00, 108.2E-09  
"TC01", 75.29E-06, 22.95E-06, 52.34E-06, 52.38E-03  
"AN1", 894.3E-09, 894.3E-09, 0.000E+00, 0.000E+00  
  
" Results at 108 Mhz for Min C "  
"Shunt at Node:", 1  
"R (Ohms):", 26.26E+03  
"L (H):", 60.74E-09  
"C (F):", 41.64E-12  
  
"Total Electric Energy (VA)", 26.17E-03  
"Total Magnetic Energy (VA)", 26.21E-03  
"Total Energy (VA)", 52.38E-03  
"Total Power Delivered (WATTS)", 76.15E-06  
"Total Power Dissipated (WATTS)", 76.19E-06
```

Figure 4.4 The RESON output report for the example coaxial resonator.

## **CHAPTER FIVE**

### **Equivalent Circuits, Coupled Circuits, and Circuit Error**

#### **5.1 Introduction**

Representative lumped element equivalent circuits are used extensively in the design and analysis of rf circuits. This chapter will concentrate on using simple RLC (Resistor, Inductor, Capacitor) equivalent representations to understand and develop complex resonant circuits.

A common and powerful technique for representing the overall operating parameters of complex resonant circuits is to use an equivalent RLC series or parallel (shunt) circuit representation of the overall resonator response. This representation not only allows a simple view of the overall operating parameters, but is also a useful intermediary for determining, or designing, interactions between circuits. These circuits are only exactly valid for one frequency although they are considered approximately valid within the bandwidth of the resonance. The element (RLC) values are determined by equating the stored electric energy, stored magnetic energy (equal at resonance), and losses of the resonator to the those of the RLC circuit. The equivalent shunt circuit is a more useful representation in most instances.

## 5.2 Circuit Quality Factor (Q)

The circuit Q is defined for materials, circuit elements, or entire circuits as:

$$Q = 2\pi \frac{\text{Peak Energy Stored each Cycle}}{\text{Average Power Dissipated each Cycle}}$$

Based on the above definition, the Q of the RLC shunt resonant circuit is:

$$Q = \omega_o R_p C$$

The Q of the RLC series resonant circuit is:

$$Q = \frac{\omega_o L}{R_s}$$

The above results are also used to describe the loss characteristics of individual capacitors, inductors, and materials. For example, it is not unusual to hear "the inductor Q is", or the "capacitor Q is", or the "material Q is" in normal conversation among radio frequency engineers. This language relates to the ideality of the component or material. In the case of the L or C component, the equations for the Q of the shunt or series resonant circuit respectively are used directly to determine the "element Q". In the case of a material, the "material Q" is simply the inverse of the handbook loss tangent of the material. In all of these cases, the fundamental definition of Q is maintained to be the ratio of energy stored to energy lost per cycle.

### 5.3 Reduced Circuit Representations

The details of the RLC equivalent series and shunt representation are developed in this section. Table 5.1 lists the common symbols that are used for this work. The symbols in the table are often augmented by descriptive subscripts for which some are tabulated in table 5.2.

Table 5.1 Definition of Common Symbols

<b>Symbol</b>	<b>Represents</b>	<b>Units</b>
U	Stored Energy	Joules
W	Power	Watts

Table 5.2 Common Subscripts

<b>Subscript</b>	<b>Represents</b>
E, e	electric
H, h	magnetic
d	dissipated

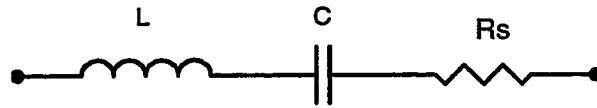
### 5.3.1 The Series Resonant Circuit

The series resonant circuit is sometimes used as an equivalent circuit representing the overall response of a larger circuit at resonance. The series resonant circuit and some useful equations are shown in figure 5.1. The energy stored in the series circuit changes abruptly from primarily electric to primarily magnetic as the operating frequency is varied through resonance. Another way to view this behavior is to observe that for  $f < f_0$  the series circuit appears capacitive, whereas, for  $f > f_0$  the series circuit appears inductive. For fixed values of ideal capacitance and inductance, the series circuit Q increases as the resistance is decreased.

### 5.3.2 The Shunt Resonant Circuit

The shunt resonant circuit is sometimes used as an equivalent circuit representing the overall response of a larger circuit at resonance. The shunt representation is used much more often than the series representation. The shunt resonant circuit and some useful equations are shown in figure 5.2. The energy stored in the shunt circuit changes abruptly from primarily magnetic to primarily electric as the operating frequency is varied through resonance. Another way to view this behavior is to observe that for  $f < f_0$  the shunt circuit appears inductive, whereas, for  $f > f_0$  the shunt circuit appears capacitive. For fixed values of ideal capacitance and inductance, the shunt circuit Q decreases as the resistance is decreased.



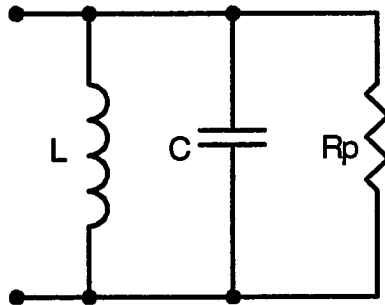


$$L = \frac{2U_H}{I_{rms}^2}, \quad C = \frac{\left(\frac{I_{rms}}{\omega}\right)^2}{2U_E}, \quad R_s = \frac{W_d}{I_{rms}^2}$$

$$\omega_o = \frac{1}{\sqrt{LC}}, \quad Q = \frac{\omega_o L}{R_s} = \frac{1}{\omega_o R_s C}$$

$$U_E = \frac{\frac{1}{2}LI^2}{\left(\frac{f}{f_o}\right)^2} = \frac{U_H}{\left(\frac{f}{f_o}\right)^2}$$

Figure 5.1 The "Series Resonant Circuit".



$$L = \frac{\left(\frac{V_{rms}}{\omega}\right)^2}{2U_H} \quad , \quad C = \frac{U_E}{2V_{rms}^2} \quad , \quad R_p = \frac{W_d}{V_{rms}^2}$$

$$\omega_o \equiv \frac{1}{\sqrt{LC}} \quad , \quad Q = \frac{R_p}{\omega_o L} = \omega_o R_p C$$

$$U_H = \frac{\frac{1}{2}CV^2}{\left(\frac{f}{f_o}\right)^2} = \frac{U_E}{\left(\frac{f}{f_o}\right)^2}$$

Figure 5.2 The "Shunt Resonant Circuit"

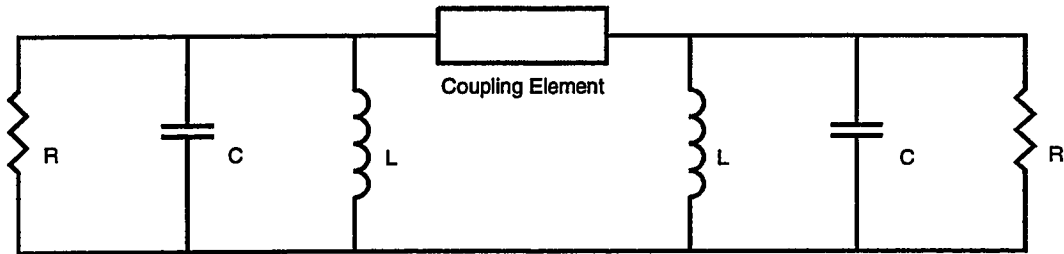
## **5.4 Coupled Resonant Circuits**

### **5.4.1 Overview**

Although none of the equipment that this dissertation is directly concerned with contains coupled resonant circuits, the accelerator community does make extensive use of them so that some description of the basic principles is appropriate. Normally, nearly identical resonators are coupled together. When resonant circuits are coupled together, multiple resonant frequencies referred to as "modes" can exist. The degree to which these modes are separated in frequency is determined by the amount of energy managed by the coupling element in relation to the total circuit energy. The greater the proportion of the total circuit energy the coupling element manages, the further the modes will be separated in frequency and vice-versa. The so called "Push-Push" condition describes the condition where the coupled resonant circuits are operating nearly in phase, whereas, the "Push-Pull" condition describes the condition where the coupled resonators are operating at nearly 180 degrees apart in phase. Capacitively coupled and inductively coupled identical resonators will be briefly discussed.

### **5.4.2 Qualitative Description of Coupled Resonators**

Figure 5.3 shows two identical resonators represented by their equivalent shunt circuits operating coupled together with an energy transfer



Push-Push Coupling with a Capacitor " $C_c$ " or Inductor " $L_c$ ".

$$f_c \cong \frac{1}{2\pi\sqrt{LC}}$$

Push-Pull Coupling with a Capacitor " $C_c$ " or Inductor " $L_c$ ".

$$f_c \cong \frac{f_o}{\sqrt{1 + \frac{2C_c}{C}}} \quad \text{or} \quad f_c \cong \frac{f_o}{\sqrt{1 + \frac{\left(\frac{L_c}{2}\right)}{L}}}$$

Figure 5.3 Low-loss identical coupled resonant circuits.

and storage element and operating at some coupled frequency ( $f_c$ ). The analysis of this circuit can be completely understood qualitatively.

If both resonators are lossless and operating at the same voltage and phase, then the coupling element has no voltage across it and may be removed from the circuit, this is the push-push state and clearly operates at the highest frequency of the two modes since a reactive element is effectively removed from the circuit. In the push-pull state, the two resonators are operating at the same voltage but 180 degrees apart in phase so that the coupling element is energized at twice the voltage seen by each resonator alone. The degree to which the modes push-push to push-pull are separated in frequency is proportional to the amount of energy managed by the coupling element in proportion to the amount of energy managed by the uncoupled circuits.

## 5.5 Impedance Matched Input Coupling

Input and output coupling is handled identically. The coupling is considered to be matched when the power reflected from the load is zero. Although this condition may be accomplished by many different methods, in general, capacitive coupling, loop coupling, or some combination of these are used.

The coupling considered here is narrow band. The necessary condition is:

$$W_{feed} = W_{lost} \text{ or } W_f = W_d$$

If a feed line (subscript l) of known impedance is supplying the power to the resonator at a point of potential  $V_r$ , then for matched coupling the following condition must hold:

$$\frac{V_l^2}{Z_o} = \frac{V_r^2}{R_p}$$

$Z_o$  is the characteristic impedance of the feed line, and  $R_p$  is the equivalent shunt resistance of the resonator at the coupling point. The three main methods of coupling are described below, although many techniques exist.

For the first method to be described, if a point in the resonator is at voltage  $V_l$ , and the power dissipated is the power delivered, then  $R_p$  is equal to  $Z_o$ . Under this condition, the feed line may be attached directly to the resonator and the match is automatic. This first case is the simplest to understand, however, it is rarely applied because such a point in the resonator may not be accessible. Normally the accessible points in the resonator are not at the correct potential and generally move with changing frequency in a way that makes this form of coupling mechanically unattractive .

The second method inserts a loop in the rf magnetic field that intercepts the proper amount of flux to generate a voltage which is equal to the feed line voltage when the power delivered is equal to the power absorbed. The coupling may be adjusted by either rotating the loop such that it varies the amount of flux that is intercepted or by varying the loop area. The fundamental equations relating the loop voltage to the intercepted flux are:

$$\Psi = \int_s \mathbf{B} \cdot d\mathbf{S} \quad \text{and} \quad V_l = -\frac{d\Psi}{dt}$$

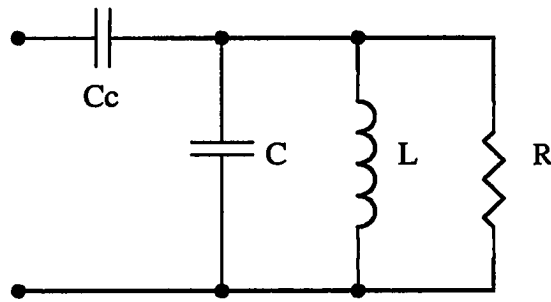
A third common method is to couple to a point in the resonator with a series reactive element that drops the proper amount of voltage so that the proper voltage/current relationship is presented to the feedline. Normally a capacitor is used as the series element although an inductor or some other circuit arrangement may also be used. Capacitive and inductive coupling are considered here. This method normally creates the largest perturbation to the cavity frequency. The resonant frequency is then shifted or the cavity retuned to resonate out the series element. The proper value of the series element is given in figure 5.4 for capacitive coupling and in figure 5.5 for inductive coupling. The equivalent shunt circuit is used to facilitate the analysis in both cases.

### **5.5.1 Capacitive Coupling**

Capacitive coupling is more common than inductive coupling. Capacitive coupling is the method applied at the NSCL for the K1200 Cyclotron. Figure 5.4 details this method. In the figure,  $\Delta f$  represents the perturbation in resonant frequency due to the insertion of the coupling capacitor.

### **5.5.2 Inductive Coupling**

Inductive coupling is less common than capacitive coupling. Figure 5.5 details this method. In the figure,  $\Delta f$  represents the perturbation in resonant frequency due to the insertion of the coupling element.



$$Z(\omega) = \frac{1}{j\omega C_c} + \frac{1}{\frac{1}{R} + \frac{1}{j\omega L} + j\omega C}$$

$$= \frac{\frac{1}{R}}{\left(\frac{1}{R}\right)^2 + \left(\omega C - \frac{1}{\omega L}\right)^2} - j \left[ \frac{1}{\omega C_c} + \frac{\left(\omega C - \frac{1}{\omega L}\right)}{\left(\frac{1}{R}\right)^2 + \left(\omega C - \frac{1}{\omega L}\right)^2} \right]$$

$$\equiv Z'(\omega) - jZ''(\omega)$$

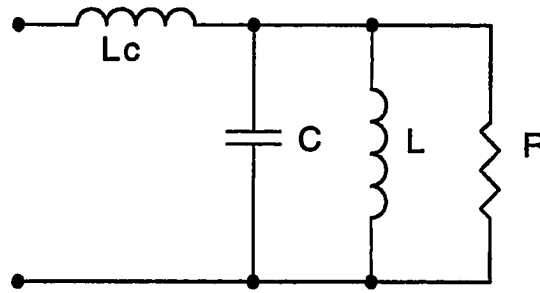
$$Z'(\omega) = Z_o \quad Z''(\omega) = 0$$

$$f_o \equiv \frac{1}{2\pi\sqrt{LC}} \quad C_c = \frac{\frac{L}{Z_o R}}{1 - \left(\frac{f}{f_o}\right)^2} \quad f = f_o \sqrt{1 - \frac{L}{Z_o R C_c}}$$

$$\Delta f = f_o \left( \sqrt{1 - \frac{L}{Z_o R C_c}} - 1 \right)$$

Figure 5.4 Matched capacitive coupling to a feedline of impedance  $Z_o$ .





$$Z(\omega) = j\omega L_c + \frac{1}{\frac{1}{R} + \frac{1}{j\omega L} + j\omega C}$$

$$= \frac{\frac{1}{R}}{\left(\frac{1}{R}\right)^2 + \left(\omega C - \frac{1}{\omega L}\right)^2} + j \left[ \omega L_c - \frac{\left(\omega C - \frac{1}{\omega L}\right)}{\left(\frac{1}{R}\right)^2 + \left(\omega C - \frac{1}{\omega L}\right)^2} \right]$$

$$\equiv Z'(\omega) + jZ''(\omega)$$

$$Z'(\omega) = Z_o \quad , \quad Z''(\omega) = 0$$

$$f_o \equiv \frac{1}{2\pi\sqrt{LC}} \quad L_c = Z_o RC \left[ 1 - \left(\frac{f_o}{f}\right)^2 \right] \quad f = \frac{f_o}{\sqrt{1 - \frac{L_c}{Z_o RC}}}$$

$$\Delta f = f_o \left[ 1 - \frac{1}{\sqrt{1 - \frac{L_c}{Z_o RC}}} \right]$$

Figure 5.5 Matched inductive coupling to a feedline of impedance  $Z_o$ .

## 5.6 Model Uncertainties and Circuit Error Estimates

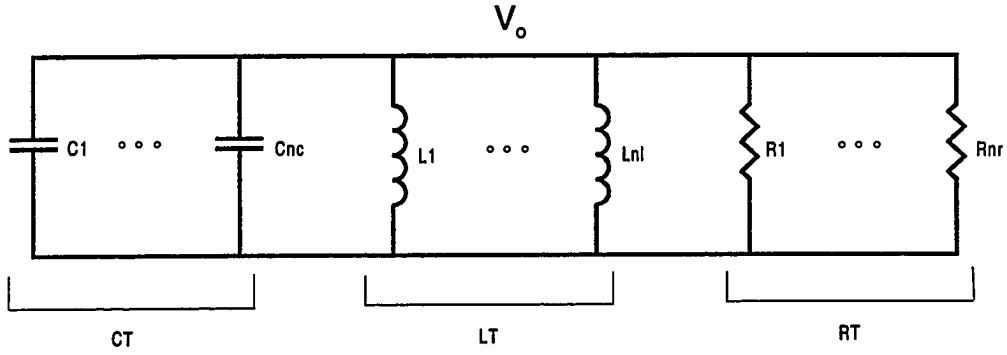
The major uncertainties in the model of a resonant circuit are due to approximations made in modeling the geometrically complex shapes and in the appropriate surface resistivity. Other uncertainties are associated with non-uniform transmission lines. An error analysis is developed that determines the effect any particular element has on the circuit response. The error analysis may be used to determine the upper and lower bounds of the circuit response.

The error analysis uses a model that consists of the superposition of the contributions of each element in the overall circuit to the equivalent shunt circuit representation. Each element of the actual circuit may contribute to the overall magnetic stored energy, electric stored energy, and losses. Individual shunt capacitors, inductors, and resistors in the equivalent shunt circuit will model the contribution of each element of the main circuit. As a result, in a circuit with "N" elements, the equivalent shunt circuit may have up to "N" each of capacitors, inductors, and resistors. Since any individual circuit element may not use all three elements to adequately model its contribution, the actual number of each type of element R, L, or C will typically be less than or equal to N. Figure 5.6 details the error analysis technique to be applied here. In the figure, " $V_o$ " represents the peak voltage applied across the shunt circuit that the contribution of all elements of the resonator will be transformed to. This voltage may represent some particular location in the actual resonator or may be any other desired value (such as 1 Volt for example).

The circuit analysis performed for this dissertation includes the option of computing the stored energy and losses for each element of the

circuit. Using this information, the individual elements of the error analysis equivalent shunt circuit are readily determined from the equations given in figure 5.6. This granular knowledge of energy and power for each element allows not only the determination of the equivalent shunt circuit values, but also of the magnitude that any given elements contribution has on the overall circuit behavior. For example, a element that has a  $\pm 50\%$  uncertainty in its predicted power dissipation and dissipates 1% of the total resonator power causes a  $\pm 0.5\%$  uncertainty in the overall circuit power dissipation. The same analysis holds for the electric and magnetic stored energy contribution of each element to the overall circuit energy. Additionally, the elements in the equivalent circuit can be grouped into subgroups that represent some particular subsystem of the resonator (the K1200 dee as an example).

Using the ideas described here, a tabulated list of the percent of the total energy any element or group of elements represents, and the associated uncertainty in these values, can be used as a measure of the overall error in predicted circuit response. Such a tabulation in combination with a knowledge of the uncertainty in element values may be used either quantitatively or qualitatively in estimating the overall circuit response error. Normally, a quantitative estimate will only be pursued if the qualitative survey of the tabulated stored energy and power data for each element shows that elements known to have large uncertainties also contain a significant fraction of the overall circuit energy or power.



$$C_T = \sum_{n=1}^{N_c} C_n \quad , \quad \frac{l}{L_T} = \sum_{n=1}^{N_L} \left( \frac{l}{L_n} \right) \quad , \quad \frac{l}{R_T} = \sum_{n=1}^{N_R} \left( \frac{l}{R_n} \right)$$

$$C_n = \frac{U_{en}}{V_o} \quad , \quad L_n = \frac{V_o}{\omega_o U_{hn}} \quad , \quad R_n = \frac{V_o}{W_{dn}}$$

$$\omega_o = \frac{l}{\sqrt{L_T C_T}} = \frac{\omega_{nom}}{\sqrt{\frac{\sum_{n=1}^{N_c} U_{en}}{\sum_{n=1}^{N_L} U_{hn}}}}$$

Figure 5.6 The error analysis circuit.

## **CHAPTER SIX**

### **Standard Elements of the Equivalent Circuit**

#### **6.1 Introduction**

At radio frequencies, the parasitic elements of circuit components become apparent and sometimes even dominant. Most components contain some parasitic capacitance, inductance, and resistance regardless of what the ideal component value may suggest. In addition, there is the added complexity of wave behavior when component sizes become comparable to the rf wavelength.

This chapter describes the common circuit elements and models of non-ideal elements that have been found useful. Circuits to represent lumped elements that account for parasitic effects will be described for resistors, capacitors and inductors. Circuit elements are referred to as lumped if the dimensions do not lead to significant wave-like behavior. It is sometimes hard to find these circuits in the literature since they have been in use for a long time and many of the most relevant books are out of print [6.1]. The lossy transmission line formulation will be described for modeling distributed behavior. The coaxial, parallel plate, and coaxial with an intervening dielectric cylinder type transmission lines be detailed.

### 6.1.1 Modeling the Lumped Elements

Many structures include resistive, capacitive, and inductive components that are small with respect to the wavelength. Components of rf circuits that are best modeled as lumped elements normally have parasitic properties causing them to not behave as an ideal element at high frequencies. Inductors contain lead resistance, turn-to-turn capacitance, and in cases where a permeable material is used, core losses and nonlinear material properties. Capacitors contain lead inductance, lead resistance, and material losses in cases where a dielectric is used. Resistors contain lead inductance and bulk capacitance. These lumped components are each modeled as an equivalent circuit which contains the ideal element combined with other elements arranged in a circuit topology to model the behavior of the component over the broadest relevant frequency range.

Industry standard equivalent circuits exist for resistors, capacitors, and inductors that include parasitic effects. Generally, these are intended to model small, low power, components typically used on printed circuit boards operated about fixed, small, bandwidths. The same circuits are applicable to larger, higher power components, if the size of the components with respect to the rf wavelength is negligible. Since the equivalent circuit of each component is added to the equivalent circuit of the entire structure, which is then analyzed numerically, the behavior of the non-ideal component need not be studied in closed form. Values for the ideal element and its associated parasitic elements may be determined analytically or from measurements. Typically the characteristics of small

components used on circuit boards are measured, whereas, high power components are calculated and then verified by measurement when significant uncertainties with the calculations are thought to exist. In the case of commercial components, manufacture's data may be available to aid in the modeling process.

### **6.1.2 Elements with Significant Distributed Effects**

In cases where the dimension of the lumped component approaches a significant fraction of a wavelength, the resulting distributed effects must be included. Each case must be separately evaluated to determine a model which properly accounts for the behavior. In some cases, the characteristics of the element itself are distributed, whereas, in other cases the element internal leads cause the distributed effects. For example, a resistor that is distributed over long lengths may be treated as a transmission line with high loss conductors. However, this would be an incorrect model if the resistance effect itself was localized and the distributed effect was due to the internal leads. In the case where the wave behavior is due to the internal leads, then the appropriate model is a transmission line that matches the lead characteristics in series with the lumped component.

A component which often exhibits distributed wave behavior is the wound inductor. Large single layer inductors with conductor lengths approaching  $1/4$  wavelength are used frequently in high power rf structures. Examples include inductors used in dc bias circuits for large vacuum tubes or as part of the resonant circuit itself. Since there has been

little success in obtaining practical closed form exact solutions for wound inductive components operating at high frequency, semi-empirical techniques are normally used.

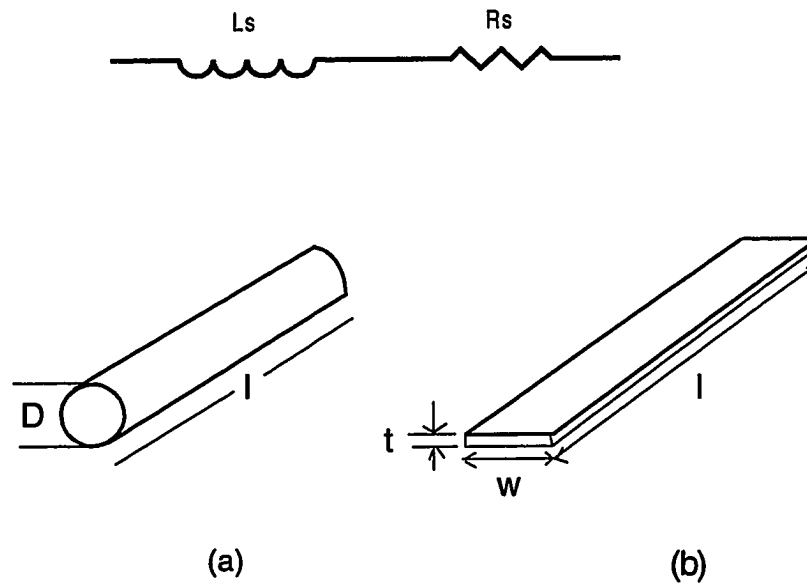
## 6.2 Lead Inductance and Resistance

Many components may be adequately modeled by an ideal core element connected to the circuit with leads which are short with respect to relevant wavelengths. Under these conditions, a lumped ideal inductance ( $L_s$ ) in series with a resistance ( $R_s$ ) may be used to represent the leads. The typical lead shapes are cylindrical (referred to as leads) or rectangular (referred to as straps). Approximate formulas for these common shapes are well known [6.1, 6.2] and are given in figure 6.1.

## 6.3 The Resistor Model

The equivalent circuit of a lumped resistive component is shown in figure 6.2. The circuit allows modeling of the internal lead inductance and bulk capacitance. The resistor is connected to the circuit through leads which are modeled separately with lumped elements or distributed elements as appropriate. The values of the elements comprising the resistor model are either determined from standard electrostatic analysis techniques, available from the manufacturer, or measured. Measurements are made to determine, or confirm, the values of the circuit elements in the resistor model. The ideal bulk resistance ( $R$ ) is assumed constant and may be measured with a dc Ohm meter of suitable accuracy. The values of





$$L = \frac{\mu l}{2\pi} \left[ \ln \left( \frac{4l}{D} \right) - 1 \right] \text{ H} \quad L = \frac{\mu l}{2\pi} \left[ \ln \left( \frac{2l}{w+t} \right) + 0.5 + 0.2235 \frac{w+t}{l} \right] \text{ H}$$

$$\text{for } \delta < \frac{D}{2}$$

$$\text{for } \delta < \frac{t}{2}$$

$$R_{ac} \cong \frac{l}{D} \sqrt{\frac{\omega \mu}{2\sigma}} \Omega$$

$$R_{ac} \cong \frac{l}{2w} \sqrt{\frac{\omega \mu}{2\sigma}} \Omega$$

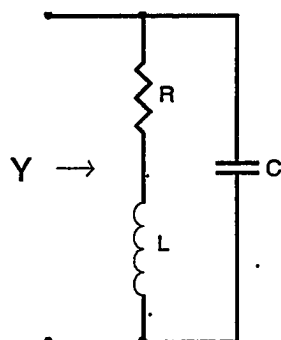
$$\text{for } \delta \geq \frac{D}{2}$$

$$\text{for } \delta \geq \frac{t}{2}$$

$$R_{DC} = \frac{l}{\sigma \pi \left( \frac{D}{2} \right)^2}$$

$$R_{DC} = \frac{l}{\sigma t w}$$

Figure 6.1 The inductance and resistance of a round conductor (a) and rectangular conductor (b). Use dimensional units consistent with  $\mu$  and  $\sigma$ .



usable range:

$$Q \leq 1, \quad Y^r(\omega) \leq Y^i(\omega) \Rightarrow \omega L \leq R \leq \frac{1}{\omega C}$$

input admittance:

$$Y(\omega) = \frac{R}{R^2 + (\omega L)^2} + j \left[ \omega C - \frac{\omega L}{R^2 + (\omega L)^2} \right]$$

$$\equiv Y^r(\omega) + jY^i(\omega)$$

$$\omega = 0 \rightarrow Y(\omega) = Y^r(0) + j0 = \frac{1}{R}, \quad \omega = \omega_o \rightarrow Y^i(\omega_o) = 0, \quad Y^r(\omega_o) = \frac{R}{Z_o^2}$$

$$Z_o \equiv \sqrt{\frac{L}{C}}, \quad \omega_o \equiv \frac{1}{L} \sqrt{Z_o^2 - R^2}$$

$$L = \frac{1}{\omega} \sqrt{\frac{R - R^2 Y^r(\omega)}{Y^r(\omega)}}, \quad C = \frac{1}{\omega} \left[ Y^i(\omega) + \frac{\omega L}{R^2 + (\omega L)^2} \right]$$

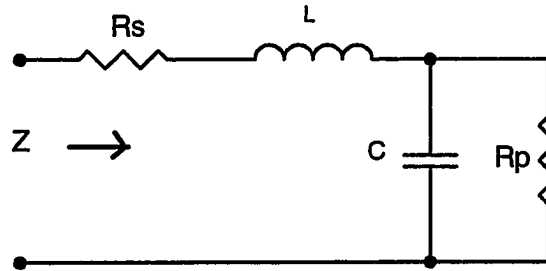
Figure 6.2 The model of a lumped resistor including parasitic effects.

the internal inductance ( $L$ ) and capacitance ( $C$ ) are best determined from measurements made at or near the operating frequency band. Two or more measurements are needed to uniquely determine the values of the internal inductance and capacitance. If the self resonant frequency is within the range of the experimental setup and test equipment, it should be measured to confirm the circuit model. Normally an exact fit of the parameters to the dc value plus two additional frequencies within the operating band yields an adequate model.

#### **6.4 The Capacitor Model**

The equivalent circuit of a lumped capacitive component is shown in figure 6.3. The circuit allows modeling of the internal lead inductance ( $L$ ), lead resistance ( $R_s$ ), bulk capacitance ( $C$ ), and dielectric losses represented by a bulk resistance ( $R_p$ ). The capacitor is connected to the circuit through leads which are modeled separately with lumped elements or distributed elements as appropriate.

The values of the elements comprising the capacitor model are either determined from standard electrostatic analysis techniques, available from the manufacturer, or measured. Measurements are made to determine, or confirm, the values of the circuit elements in the capacitor model. The ideal bulk capacitance is assumed to be constant and may be measured with a low frequency capacitance meter of suitable accuracy. The values of the internal lead resistance, bulk resistance, and lead inductance are best determined from measurements made at or near the



input impedance:

$$Z(\omega) = R_s + j\omega L + \frac{1}{\frac{1}{R_p} + j\omega C}$$

$$= R_s + \frac{R_p}{1 + (\omega R_p C)^2} - j \left( \frac{\omega C}{\left(\frac{1}{R_p}\right)^2 + (\omega C)^2} - \omega L \right)$$

$$Z(\omega) \equiv Z'(\omega) - jZ''(\omega)$$

equivalent circuit parameters for  $Q \gg 1$  and  $f < f_o$ :

$$f_o \equiv \frac{1}{2\pi\sqrt{LC}} \quad , \quad Z(\omega) \equiv esR - j\frac{1}{\omega C_{eq}}$$

$$esR \equiv R_s + \frac{R_p}{1 + (\omega R_p C)^2} \quad , \quad \text{for } \omega C \ll R_p : C_{eq} = \frac{C}{1 - \left(\frac{f}{f_o}\right)^2}$$

(esR = manufacturers jargon: "Equivalent Series Resistance")

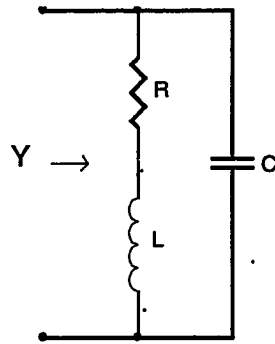
Figure 6.3 The model of a lumped capacitor including parasitic effects.

operating frequency band. Unlike the resistor, the  $Q$  of the capacitor is assumed to be  $\gg 1$  so that a measurement of the dc capacitance,  $Q$ , and the self resonant frequency of the capacitor may be used to determine the elements if the lead resistance is neglected.

## **6.5 The Inductor Model**

The equivalent circuit of a lumped inductive component is shown in figure 6.4. The circuit allows modeling of the conductor resistance ( $R$ ) and bulk capacitance ( $C$ ). The leads which connect the inductor to the circuit are modeled separately with lumped elements or distributed elements as appropriate.

The inductor is probably the most difficult component to analyze accurately. Estimation of the conduction loss is complicated by the complex current distribution on the conductors due to the "proximity effect", in addition to the normal skin effect. Shields also cause the inductance to decrease and the losses to be increased. For single layer air core solenoids, approximate formulas and tables exist to help quantify these effects [6.1, 3.5]. For more complex structures, numerical analysis techniques may be necessary. The ideal bulk inductance may be measured with a low frequency instrument of suitable accuracy. The values of the internal lead resistance and bulk capacitance are best determined from measurements made at or near the operating frequency band. Unlike the resistor, the  $Q$  of the inductor is assumed to be much greater than one so that a measurement of the dc inductance,  $Q$ , and the self resonant frequency of the inductor may be used to determine the



input admittance:

$$Y(\omega) = \frac{R}{R^2 + (\omega L)^2} + j \left[ \omega C - \frac{\omega L}{R^2 + (\omega L)^2} \right]$$

$$\equiv Y'(\omega) - jY''(\omega)$$

equivalent circuit parameters for  $Q \gg 1$  and  $f < f_o$ :

$$f_o \equiv \frac{1}{2\pi\sqrt{LC}} \quad , \quad Y(\omega) \equiv \frac{1}{R_{eq}} - j\frac{1}{\omega L_{eq}}$$

$$R_{eq} = R \left( 1 + \left( \frac{\omega L}{R} \right)^2 \right) \quad , \quad \text{if } \omega L \gg R : L_{eq} = \frac{L}{1 - \left( \frac{f}{f_o} \right)^2}$$

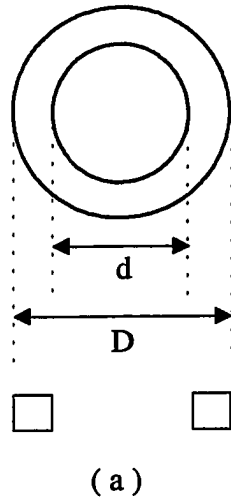
Figure 6.4 The model of a lumped inductor including parasitic effects.

element values.

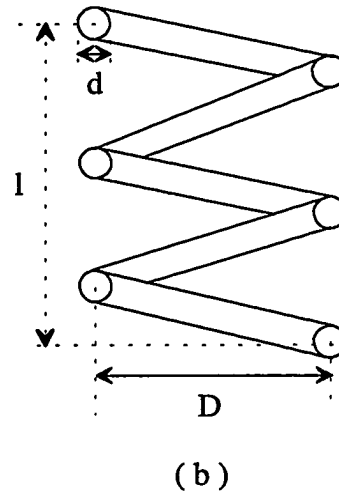
### **6.5.1 Common Formulas for Ideal Inductances**

The solenoid and toroid are two common structures used in rf circuits, and formulas for the idealized magnetostatic self inductance of these two common geometries exist [6.1, 6.3]. The ideal inductance ignores parasitic effects and any distributed effects due to the conductor lengths. Figure 6.5 displays the geometry and associated formulas for the ideal inductance of these two structures.

For the solenoid, the ideal inductance is reduced when placed in a shield (typically cylindrical). Tables exist to determine the reduction in the ideal inductance due to a cylindrical shield [3.5, 6.4]. The shield behaves as a shorted coupled coil. If the shield is cut vertically (interrupting the circular currents which would otherwise flow) the inductance reduction factor due to the shield is reduced.



$$L = \frac{\mu N^2}{2\pi} h \ln \left( \frac{D}{d} \right) \text{ H}$$



$$L = \frac{2.54 N^2 D^2}{36D + 40l} \mu\text{H}$$

accuracy  
 < 1% error  
 for  $l > 0.4D$

N is the number of turns.

For the toroid, use dimensional units compatible with the permeability " $\mu$ ".

For the solenoid, use centimeters.

Figure 6.5 The ideal self inductance of (a) the square core toroid, and (b) the air core solenoid.



### **6.5.2 Solenoids with Significant Distributed Effects**

If the lengths of the conductor making up the inductor becomes significant with respect to the relevant frequency range then the problem becomes more complex. One practical recourse with these structures is to rely on approximate procedures and measurements to determine a reasonable model.

The structure which appears most frequently in high power rf structures is the single layer, shielded, air core solenoid. Techniques have been developed at the NSCL to yield a reasonably accurate model of this structure when the length of the winding is significant with respect to the wavelength [6.5]. This technique treats the solenoid as a slow wave structure and transforms it to an equivalent transmission line representation.

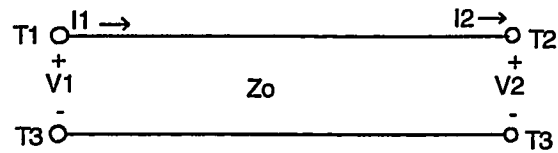
### **6.5.3 Inductors as Electronic Tuning Elements**

In high power structures which do not require high frequency modulation, permeable core materials are typically avoided due to their non-linear and high loss properties. However, if rapid frequency modulation is required, then a technique which exploits the non-linear properties of permeable materials is sometimes used. In this case, the modulating structure consists of a winding(s) which are separated from the rf fields by a thin layer of non-magnetic metal which is impenetrable by the rf fields due to the skin depth yet sufficiently penetrated by the modulating frequency. In addition, the applied modulating magnetic field and the rf

magnetic field are often designed to be perpendicular to one another and the permeable material is operated near saturation to reduce losses [6.6]. This type of structure plays an important role in high energy synchrotrons which require rapid frequency modulation. These effects are not encountered in this dissertation although they are the subject of intense research by facilities that need them [6.7].

## 6.6 The Transmission Line Model

All transmission lines share a common circuit model. The transmission line model equations are given in figure 6.7. The lossy transmission line equations are used for this model. When the lossy transmission line model is used for unterminated lines, it is essential that both the characteristic impedance and the propagation constant be complex or large errors may result [6.8]. The transmission line is treated as a three terminal device with one conductor maintained at a constant potential while the other conductor potential varies as usual. The currents on the conductors are the mirrors of one another. In figure 6.7,  $w_1$  and  $w_2$  represent the conductor widths,  $Q_e$  and  $Q_m$  represent the Q of the electric and magnetic material intervening the conductors, and L and C represent the inductance and capacitance per unit length.



$$V_1 = V_2 \cosh(\gamma l) + \frac{I_2}{Y_o} \sinh(\gamma l)$$

$$I_1 = V_1 Y_o \sinh(\gamma l) + I_2 \cosh(\gamma l)$$

$$Y_o = \sqrt{\frac{G + j\omega C}{R + j\omega L}}$$

$$\gamma = \alpha + j\beta = \sqrt{(R + j\omega L)(G + j\omega C)}$$

$$R_{c1} = \frac{1}{w_1} \sqrt{\frac{\mu\omega}{2\sigma}} \quad , \quad R_{c2} = \frac{1}{w_2} \sqrt{\frac{\mu\omega}{2\sigma}}$$

$$G = \frac{\omega C}{Q_e} \quad , \quad R = \frac{\omega L}{Q_m} + R_{c1} + R_{c2}$$

$$Z_o = \sqrt{\frac{L}{C}} \quad , \quad v = \frac{1}{\sqrt{LC}} \quad , \quad C = \frac{1}{vZ_o} \quad , \quad L = \frac{Z_o}{v}$$

where "v" denotes the speed of light in the medium

Figure 6.7 The lossy transmission line circuit formulation.

### 6.6.1 Ideal Coaxial and Parallel Plate Types

The ideal coaxial and parallel plate transmission lines are very heavily utilized types. Figure 6.8 contains the formulas for these two types.

### 6.6.2 Coaxial Line with Intervening Coaxial Cylinder

The K1200 cyclotron rf resonators contain a vacuum window which separates the tunable stem from the rest of the resonator. This vacuum window appears as a coaxial transmission line with an intervening dielectric cylinder. Figure 6.9 displays this geometry and the resultant formulas from the ensuing development.

The development of the formulas for this type of line begins by noting that the electric flux density is unaffected by dielectrics. Due to symmetry, only the "r" component in the cylindrical coordinate system is retained.

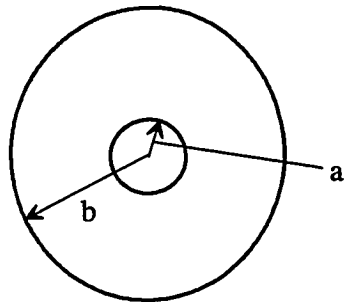
$$\nabla \cdot \mathbf{D} = \frac{1}{r} \frac{\partial}{\partial r}(rD_r) = 0 \Rightarrow D_r = \frac{A}{r}$$

with "A" an arbitrary constant. This results in an expression for the voltage between the conductors of

$$V_o = \frac{A}{\epsilon_o} \left[ \ln \left( \frac{c}{a} \right) + \frac{1}{\epsilon_r} \ln \left( \frac{d}{c} \right) + \ln \left( \frac{b}{d} \right) \right] \equiv \frac{AB}{\epsilon_o}.$$

The electric flux density is then

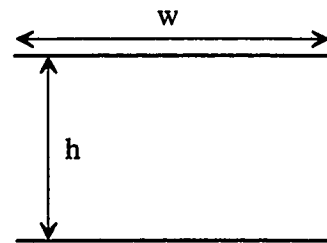
$$D_r = \left( \frac{\epsilon V_o}{B} \right) \left( \frac{1}{r} \right)$$



Coaxial Line

$$Z_o = \frac{1}{2\pi} \sqrt{\frac{\mu}{\epsilon}} \ln\left(\frac{b}{a}\right)$$

$$w_1 = 2\pi a, \quad w_2 = 2\pi b$$



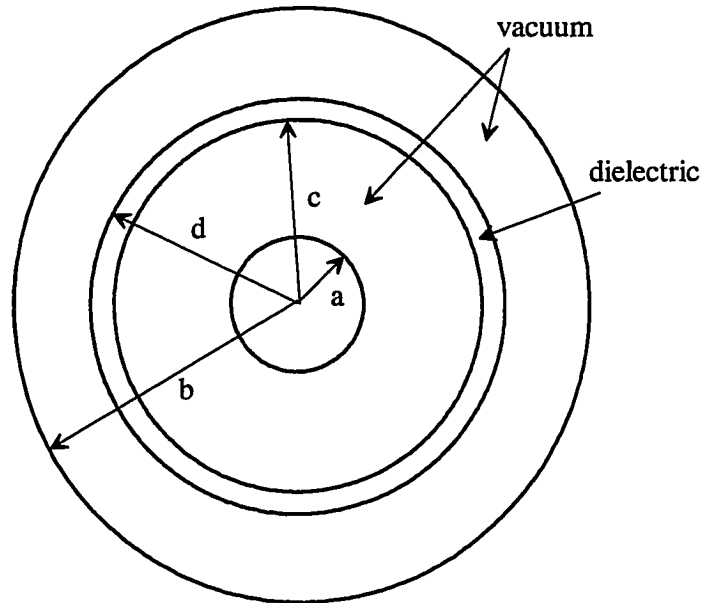
Parallel Plate Line

$$Z_o = \sqrt{\frac{\mu}{\epsilon}} \left(\frac{h}{w}\right)$$

$$w_1 = w_2 = w$$

Use the formulas from Figure 6.7  
to Complete the model

Figure 6.8 Standard coaxial and parallel plate transmission lines.



Coaxial Cylinder with an Intervening  
Dielectric with Dielectric Constant  
 $\epsilon_r$

Model with the standard coaxial  
line formulas with inner radius "a",  
outer radius "b", and effective dielectric constant  
 $\epsilon_r'$

$$\epsilon_r' = \frac{\ln\left(\frac{b}{a}\right)}{\left[\ln\left(\frac{c}{a}\right) + \frac{1}{\epsilon_r} \ln\left(\frac{d}{c}\right) + \ln\left(\frac{b}{d}\right)\right]}$$

Figure 6.9 A coaxial transmission line with an intervening dielectric cylinder.

The charge per meter determines the capacitance per meter.

$$\frac{Q}{l} = \int_0^{2\pi} D r d\phi \Rightarrow C_o = \frac{2\pi\epsilon_o}{B}$$

The inductance per meter is given by:

$$L_o = \frac{\mu_o}{2\pi} \ln\left(\frac{b}{a}\right).$$

The characteristic impedance and group velocity are then found

$$Z_o = \sqrt{\frac{L_o}{C_o}} = \frac{\eta}{2\pi} \sqrt{B \ln\left(\frac{b}{a}\right)} \quad \text{and} \quad v = \frac{1}{\sqrt{L_o C_o}} = \frac{c}{\sqrt{\frac{\ln\left(\frac{b}{a}\right)}{B}}}$$

where " $\eta$ " is the wave impedance in vacuum ( $\sim 377$  Ohms) and " $c$ " is the speed of light in vacuum ( $\sim 3 \times 10^8$  m/s). The line may be transformed to a standard loaded coaxial type by finding a suitable choice of dielectric constant. This value may be equivalently derived from either the expression for the characteristic impedance or the expression for the velocity. Deriving the effective dielectric constant from the velocity expression yields:

$$v = \frac{c}{\sqrt{\frac{\ln\left(\frac{b}{a}\right)}{B}}} \equiv \frac{c}{\sqrt{\epsilon_r'}} \Rightarrow \epsilon_r' = \frac{\ln\left(\frac{b}{a}\right)}{B} = \frac{\ln\left(\frac{b}{a}\right)}{\left[\ln\left(\frac{c}{a}\right) + \frac{1}{\epsilon_r} \ln\left(\frac{d}{c}\right) + \ln\left(\frac{b}{d}\right)\right]}$$

The coaxial line with an intervening dielectric cylinder as shown in the figure may now be modeled with an equivalent line of the original length, original inner and outer conductor radius, yet with an overall dielectric constant of  $\epsilon_r'$  and the original dielectric material  $Q_e$ .

### 6.6.3 Other Documented Line Types

Standard handbooks [3.5, 6.4] may be used to determine the characteristic impedance and occasionally the loss characteristics for many standard line types. For the typical case where a closed form solution for the characteristic impedance is given but no loss information, techniques from chapter 7 on non-standard transmission lines may be applied.



## **CHAPTER SEVEN**

### **Nonstandard Transmission Lines 1: Nonstandard Cross-sections, Discontinuities, and Corners**

#### **7.1 Introduction**

This chapter describes and develops methods for handling nonstandard transmission line cross-sections, discontinuities, and corners. A "Nonstandard" transmission line cross-section is one for which a closed-form solution is not known. When a transmission line cross-section changes abruptly along the guided wave axis, the abrupt change is referred to as a "Discontinuity". When the guided wave axis changes direction, either smoothly or abruptly, this will be referred to and handled as a "Corner". The developments in this chapter are adequate for modeling many rf structures including the K1200 rf resonators.

#### **7.2 Using Electrostatic Analysis to Determine Non-Standard Line Parameters**

As mentioned in section 2.1, when operating in the so-called transmission line mode, the electric fields at a cross-section may be determined from the known voltages on the conductors using electrostatic methods. In the following developments, it is presumed that the transverse

electric fields are determined using electrostatic methods either in closed form or numerically.

### 7.2.1 Characteristic Impedance

The characteristic impedance is found by using the solution for the electrostatic field maintained by the voltage between the two conductors. The induced charge on a conductor ( $Q$ ) per unit length, divided by the voltage between the two conductors ( $V_o$ ), yields the capacitance per unit length of the transmission line. The characteristic impedance is readily found from a combination of this knowledge and the speed of light in the medium " $v$ " surrounding the conductors.

$$Q = \int_s \mathbf{D} \cdot d\mathbf{S} \quad , \quad C = \frac{|Q|}{V_o} \quad , \quad Z_o = \frac{1}{vC}$$

This technique can be extended to systems with more than two conductors by determining the electric field for multiple bias conditions. For example, if the voltage for all conductors less one is set equal to zero, then the capacitance per unit length between the energized conductor and each additional grounded conductor in the system may be found by determining the charge induced on each grounded conductor. Since the net charge in the system is zero, the sum of the magnitude of the induced charge on all zero potential conductors must equal the charge on the energized conductor.

In mathematical terms, the capacitance between the energized conductor "i" and the un-energized conductor "j" is:

$$C_{ij} = \frac{|Q_j|}{V_i}.$$

### 7.2.2 Conduction Losses

This section will develop a method to map non-constant current distributions on a transmission line conductor to an equivalent constant current distribution on an "Equivalent Conductor Width", denoted by " $w_e$ ", which maintains the same net losses and total current. In an infinitely long uniform transmission line oriented along the z direction, the TEM field solution is defined to have x and y directed components but no z component. Under these constraints, and assuming a suppressed  $e^{j\omega t}$  functionality, the electric field traveling in the positive z direction may be expressed as:

$$\mathbf{E}(x, y, z) = E_x(x, y)e^{-jkz}\hat{x} + E_y(x, y)e^{-jkz}\hat{y}$$

The magnetic field is proportional to the curl of  $\mathbf{E}$ :

$$\nabla \times \mathbf{E} = -\frac{\partial E_y}{\partial z}\hat{x} + \frac{\partial E_x}{\partial z}\hat{y} + \left(\frac{\partial E_y}{\partial x} - \frac{\partial E_x}{\partial y}\right)\hat{z}$$

Since the transverse electric field obeys the electrostatic field solution which is a conservative vector field then:

$$\frac{\partial E_y}{\partial x} - \frac{\partial E_x}{\partial y} = 0$$

Substituting the resultant curl expression into another of Maxwell's equations, assuming sinusoidal behavior, and solving for  $\mathbf{H}$  leaves:

$$\mathbf{H} = -\frac{1}{j\omega\mu} \nabla \times \mathbf{E} = \frac{1}{j\omega\mu} \frac{\partial}{\partial z} (E_y \hat{x} - E_x \hat{y}) e^{-jKz} = -\frac{K}{\omega\mu} (E_y \hat{x} - E_x \hat{y}) e^{-jKz}$$

The wave number "K" with units of radians/meter may be expressed as:

$$K = \omega \sqrt{\mu\epsilon}$$

Using the above expression for K,  $\mathbf{H}$  may be expressed as:

$$\mathbf{H} = -\sqrt{\frac{\epsilon}{\mu}} (E_y \hat{x} - E_x \hat{y}) e^{-jKz} = \frac{-(E_y \hat{x} - E_x \hat{y}) e^{-jKz}}{\eta}$$

Due to the skin effect, at sufficiently high frequencies the current is constrained to very near the surface so that the conductor current density may be considered a surface current sheet of thickness  $\delta$ . The surface current density denoted by  $\mathbf{K}_s$  is determined by:

$$\mathbf{K}_s = \hat{n} \times \mathbf{H}_s$$

where,

$$\hat{n} = n_x \hat{x} + n_y \hat{y}$$

" $\mathbf{H}_s$ " is the value of the magnetic field at the conductor surface and "n" is a unit vector oriented into the field and normal to the conductor surface. With these results, the surface current and electric field at the surface are related by:

$$\mathbf{K}_s = \hat{n} \times \mathbf{H}_s = \frac{(n_x E_{xs} + n_y E_{ys}) \hat{z}}{\eta} = \frac{(\hat{n} \bullet \mathbf{E}_s) \hat{z}}{\eta}$$

The above expression is a fundamental result that will be used extensively in determining the conductor losses in the rf resonators considered.

Using the result for the surface current density developed above, a method to map a non-uniform current distribution flowing on an arbitrarily shaped conductor to a constant current density on a simple planer conductor is now developed. The mapping will maintain the original total current and conduction losses.

The term mapping often refers to mathematical techniques which are uniquely reversible. The mapping referred to here is transformation of many different geometries to a single standard one and hence, is not uniquely reversible. However, the term is used with the understanding that it does not refer to a strict mathematical convention.

The surface resistance of a good conductor is given by:

$$R_s = \frac{1}{\sigma\delta} = \sqrt{\frac{\omega\mu}{2\sigma}},$$

where  $\delta$  is the skin depth defined in section 3.2.3 and  $\sigma$  is the conductivity. The conduction losses per unit length along a width "l" of conductor is given by the following line integrals:

$$P = R_s \int_0^l |K_s|^2 dl = \frac{R_s}{\eta^2} \int_0^l |E_s|^2 dl$$

The power may be mapped onto an equivalent conductor of width " $w_e$ " by the following expression:

$$P = \frac{R_s i^2}{w_e}$$

Substituting into the previous expression for power leaves:

$$\frac{R_s i^2}{w_e} = R_s \int_0^l |K_s|^2 dl = \frac{R_s}{\eta^2} \int_0^l |E_s|^2 dl$$

The total current "i" along "l" is determined from:

$$i = \int_0^l |K_s| dl = \frac{1}{\eta} \int_0^l |E_s| dl$$

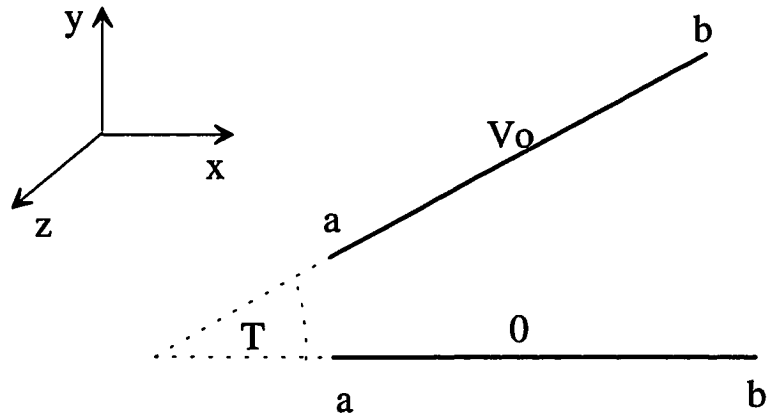
Substituting into the previous expression and solving for " $w_e$ " leaves:

$$w_e = \frac{\left[ \int_0^l |K_s| dl \right]^2}{\int_0^l |K_s|^2 dl} = \frac{\left[ \int_0^l |E_s| dl \right]^2}{\int_0^l |E_s|^2 dl}$$

The previous expression will be used extensively to map irregular shaped conductors with non-constant current distributions into simple uniform conductors which may be described by simple transmission line models. Using the method described, the conduction losses of a non-uniform current distribution on a complex conductor shape may be mapped to an equivalent width of conductor, denoted by " $w_e$ ", with a uniform current distribution. In most cases, the electric field and the above expression will be evaluated numerically.

### 7.2.3 A Simple Illustrative Example

A simple problem which may be worked in closed form, when fringe effects and fields outside of the wedge are neglected, is presented in figure 7.1. The graphic in the figure represents the cross-section of an infinitely long transmission line for which the fields are somehow contained within the minor angle of the wedge totally within the space intervening the conductors.



1) Solve Laplace's equation:  $\nabla^2 V = \frac{1}{r^2} \frac{d^2 V}{d^2 \phi} = 0 \Rightarrow V(\phi) = \frac{V_0}{T} \phi$

2) Solve for the electric field:  $\mathbf{E} = -\nabla V = -\frac{\left(\frac{V_0}{T}\right)}{r} \hat{\phi}$

3) Solve for the charge per unit length:  $\frac{Q}{L} = -\frac{\epsilon V_0}{T} \int_a^b \frac{dr}{r} = -\frac{\epsilon V_0}{T} \ln\left(\frac{b}{a}\right)$

4) Solve for the capacitance per unit length:  $C = \frac{|Q|}{V_0} = \frac{\epsilon}{T} \ln\left(\frac{b}{a}\right)$

5) Solve for the characteristic impedance:  $Z_0 = \frac{1}{vC} = \frac{T \sqrt{\frac{\mu}{\epsilon}}}{\ln\left(\frac{b}{a}\right)} = \frac{\eta T}{\ln\left(\frac{b}{a}\right)}$

6) Solve for the equivalent width of each conductor :

$$w_e = \frac{\left[ \int_0^l |E_s| dl \right]^2}{\int_0^l |E_s|^2 dl} = \frac{\left[ \int_a^b \frac{dr}{r} \right]^2}{\int_a^b \frac{dr}{r^2}} = \frac{\ln\left(\frac{b}{a}\right)}{\left(\frac{1}{a} - \frac{1}{b}\right)}$$

Figure 7.1 A simple illustrative mapping example.



### **7.3 Transmission Line Discontinuities**

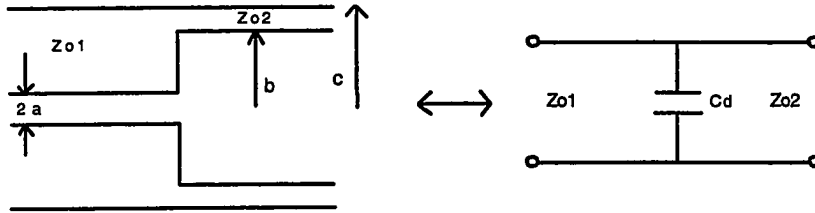
Discontinuities along the direction of propagation are modeled with lumped elements. The discontinuities encountered along the direction of propagation take the form of a T-Circuit topology with a shunt capacitor and two series inductors. It is not unusual for a discontinuity to be adequately represented by only a shunt capacitive element or series inductive element in which case the T-circuit reduces to a single element. The discontinuities normally encountered are small with respect to the rf wavelength so that electrostatic techniques may be employed, and first order closed form expressions for the discontinuities utilized. When closed form solutions are not readily obtainable, then numerical analysis can be used. Fringe effects are either handled numerically or assumed to scale in accordance with the fringe effects of the associated transmission lines.

#### **7.3.1 Coaxial Step Discontinuities**

Figure 7.1 lists formulas for steps in the conductors of coaxial structures. [2.7, 7.2]

#### **7.3.2 Parallel Plate Step Discontinuities**

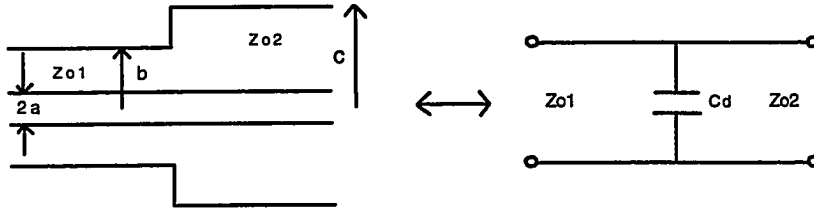
Parallel plate height and width step problems are duals of one another. The formulas derived in this section are for the simple parallel plate case which neglects edge effects. When thought to be needed, more advanced formulas may be found by extending the results for microstrip



$$C_d = \frac{c\epsilon}{50} \left[ \frac{\alpha^2 + 1}{\alpha} \ln \frac{1 + \alpha}{1 - \alpha} - 2 \ln \frac{4\alpha}{1 - \alpha^2} \right] + 2\pi c(1 - \alpha)(1 - \tau)(1.11 \times 10^{-15}) F$$

$$\alpha = \frac{c - b}{c - a} \quad , \quad \tau = \frac{c}{a}$$

The maximum error is  $\pm 0.6\pi c fF$  for  $0.01 \leq \alpha \leq 1.0$  and  $1.0 \leq \tau \leq 6.0$ .



$$C_d = \frac{a\epsilon}{50} \left[ \frac{\alpha^2 + 1}{\alpha} \ln \frac{1 + \alpha}{1 - \alpha} - 2 \ln \frac{4\alpha}{1 - \alpha^2} \right] + 2\pi a(0.8 - \alpha)(\tau - 1.4)(4.12 \times 10^{-15}) F$$

$$\alpha = \frac{c - b}{c - a} \quad , \quad \tau = \frac{c}{a}$$

The maximum error is  $\pm 0.6\pi a fF$  for  $0.01 \leq \alpha \leq 0.7$  and  $1.5 \leq \tau \leq 6.0$

Figure 7.1 Formulas for steps in the inner and outer conductors of coaxial lines. Use units of centimeters.

transmission lines found in the literature [1.4, 2.7, 6.4]. Functionally, the magnetic field for a step in width is the same as the electric field for a step in height differing only by a scalar multiplier. The problem is first analyzed for a step in height using electrostatic techniques. The electrostatic result is then modified using the duality of the results to find the results for a step in width. A step in height will be modeled in the circuit with a shunt capacitor, whereas, the step in width will be modeled with a series inductance.

The justification for the duality condition is based on the set of simplified Maxwell's equations which are written for the isotropic, non-conducting, interconductor gap case under time static conditions. These equations may be written as

$$\nabla_t \times \mathbf{E}_t = 0 \quad , \quad \nabla_t \times \mathbf{H}_t = 0$$

$$\nabla \cdot \mathbf{H} = 0 \quad , \quad \nabla \cdot \mathbf{E} = 0,$$

with boundary conditions for the appropriate dual cases as

$$\hat{n} \cdot \mathbf{H} = \hat{t} \times \mathbf{H} = 0 \quad \hat{n} \times \mathbf{E} = 0$$

on the conducting boundaries. The unit vector  $\hat{n}$  is defined as oriented into the field and normal to the boundary surface and the unit vector  $\hat{t}$  is oriented plane parallel to the conducting surface.

The general solution to Laplace's equation for the electrostatic potential in the region  $x > 0$  in figure 7.2 may be expressed as:

$$V(x, y) = a + by + \sum_{n=1}^{\infty} [A_n \sin(\lambda y) + B_n \cos(\lambda y)] e^{-\lambda x}$$

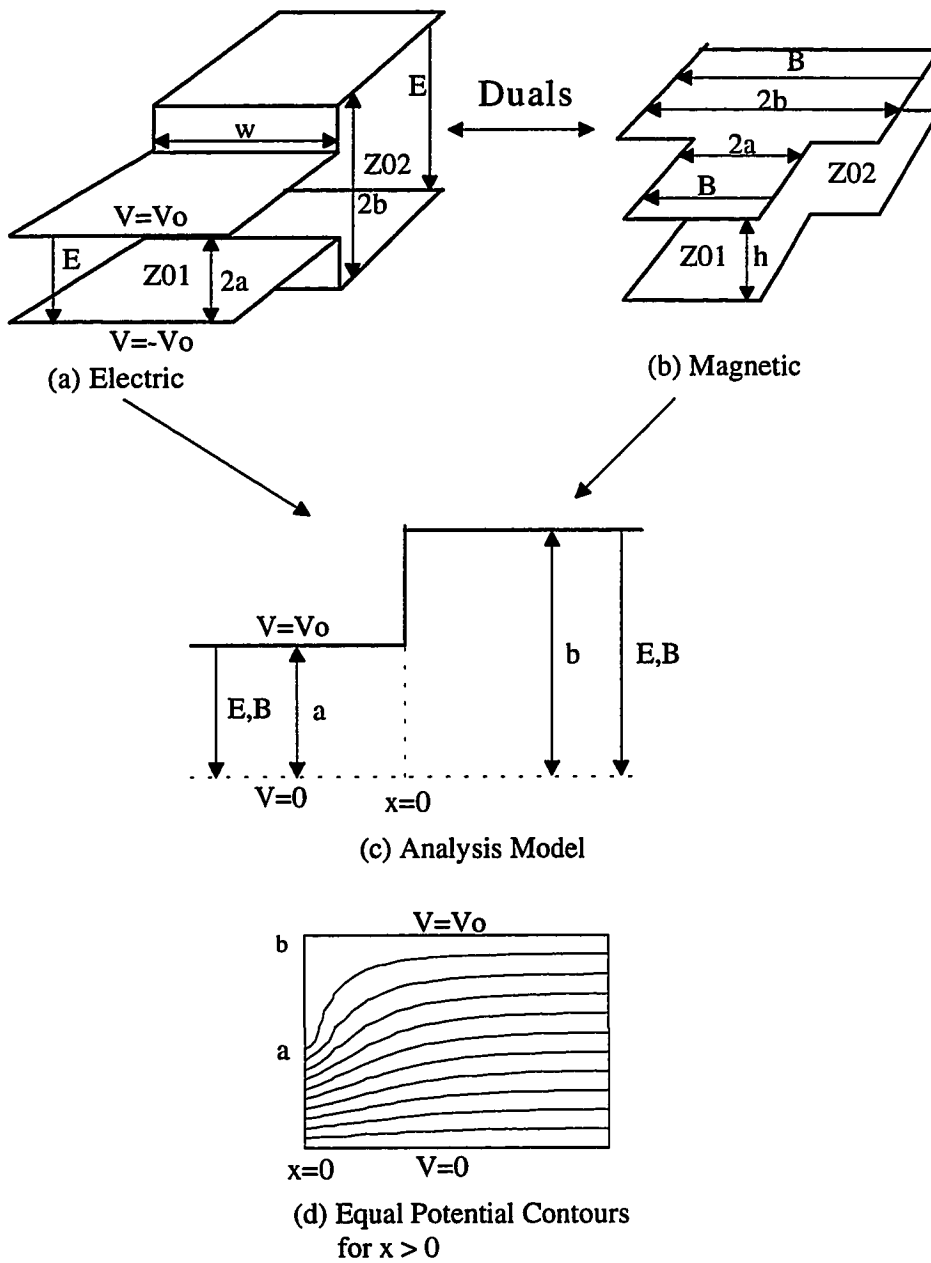


Figure 7.2 The dual problems of a step in height and step in width of a parallel plate transmission line neglecting side fringes.

Applying the boundary conditions:

$$E_x(0, y) = 0, E_x(b, 0) = 0, E_y(\infty, y) = \frac{-V_o}{b}, E_y(0, y) = \frac{-V_o}{a}$$

yields:

$$V(x, y) = \frac{V_o}{b}y + \frac{2V_o}{\pi^2} \left(\frac{b}{a}\right) \sum_{n=1}^{\infty} \frac{1}{n^2} \sin(n\pi\frac{a}{b}) \sin(n\pi\frac{y}{b}) e^{\frac{-n\pi x}{b}}$$

The y-directed electric field on the  $y = 0$  plane is :

$$\mathbf{E}_y(x, 0) = \frac{-V_o}{b} - \left(\frac{2}{\pi}\right) \frac{V_o}{b} \sum_{n=1}^{\infty} \left[ \frac{1}{n} \sin(n\pi\frac{a}{b}) e^{\frac{-n\pi x}{b}} \right]$$

For the dual magnetic problem, the y-directed magnetic field is:

$$\mathbf{H}_y(x, 0) = \frac{-I_o}{b} - \left(\frac{2}{\pi}\right) \frac{I_o}{b} \sum_{n=1}^{\infty} \left[ \frac{1}{n} \sin(n\pi\frac{a}{b}) e^{\frac{-n\pi x}{b}} \right]$$

The electric and magnetic fields are clearly the sum of the unperturbed constant field value with a component due to the discontinuity. For the electric case, the additional shunt capacitance is found by computing the net induced electric charge due to the discontinuity field on the  $y = 0$  plane and dividing by the applied voltage. For the magnetic case, the additional series inductance is found from computing the net induced magnetic flux due to the discontinuity field on the  $y = 0$  plane and dividing by the applied current.

The analysis yields:

$$C = \frac{2\varepsilon w}{\pi^2} \left( \frac{b}{a} \right) \left| \sum_{n=1}^{\infty} \left[ \frac{-1}{n^2} \sin(n\pi \frac{a}{b}) \right] \right| \quad \text{F}$$

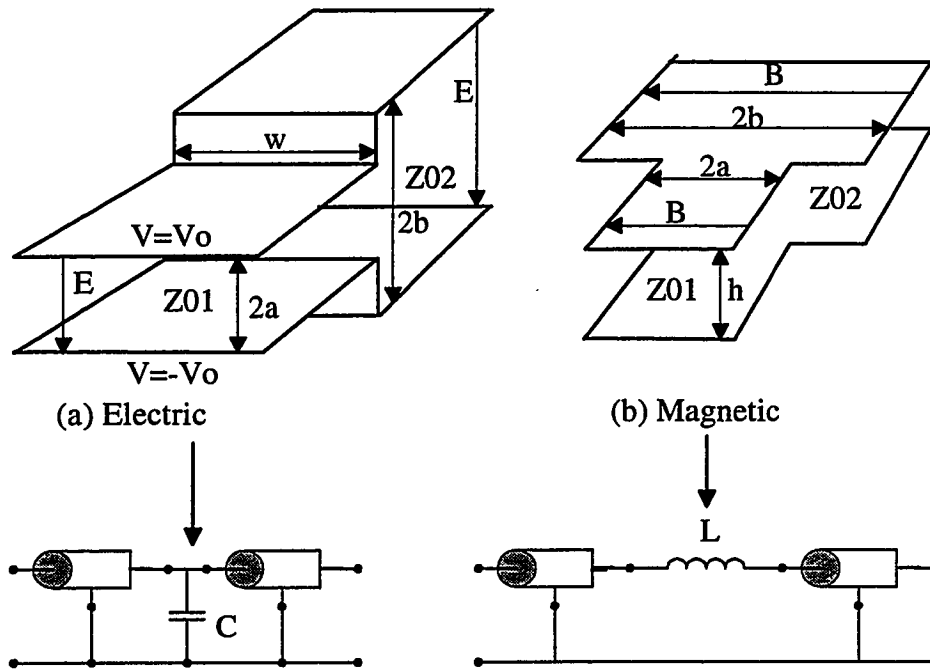
Since the analysis for a step in width is the magnetic dual of the step in height, then the result for a step in width from a to b is obtained from the result for the step in height by replacing the source term  $V_o$  by  $I_o$ , and changing the material parameter from  $\varepsilon$  to  $\mu$ .

$$L = \frac{2\mu h}{\pi^2} \left( \frac{b}{a} \right) \left| \sum_{n=1}^{\infty} \left[ \frac{-1}{n^2} \sin(n\pi \frac{a}{b}) \right] \right| \quad \text{H}$$

The results are depicted in figure 7.3.

#### 7.4 Corners and Bends

Figure 7.4 displays the E-Plane and H-Plane corners for a simple parallel plate transmission line with the edge effects neglected. Roughly speaking, ignoring changes in magnitude, an E-Plane discontinuity occurs when there is a perturbation in the E-Field functionality, yet the H-Field functionality is unperturbed. For simple parallel plate transmission lines, E-Plane and H-Plane are dual cases of one another. This section will describe a technique for handling corners of any angle in a simple parallel plate transmission. The technique will be shown to be equivalent to a formal first order solution to the field equations. Based on the results for the parallel plate line, it will be apparent that the same technique applied to



for a step in height:

$$C = \frac{2\epsilon w}{\pi^2} \left( \frac{b}{a} \right) \left| \sum_{n=1}^{\infty} \left[ \frac{-1}{n^2} \sin(n\pi \frac{a}{b}) \right] \right|$$

for a step in width:

$$L_s = \frac{2\mu h}{\pi^2} \left( \frac{b}{a} \right) \left| \sum_{n=1}^{\infty} \left[ \frac{-1}{n^2} \sin(n\pi \frac{a}{b}) \right] \right|$$

Figure 7.3 Formulas for steps in the height or width of parallel plate lines.

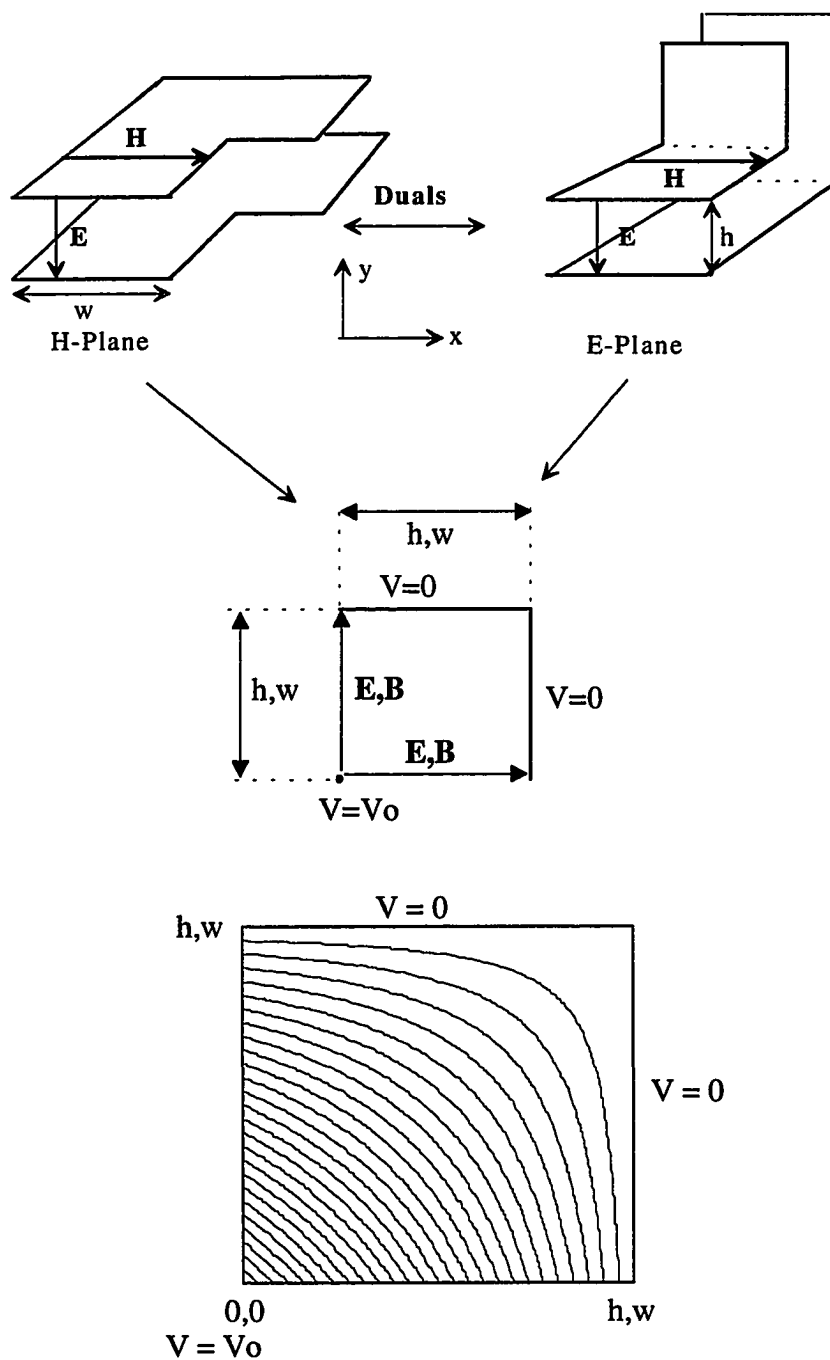


Figure 7.4 The dual problems of a E-Plane and H-Plane 90 degree bend for a parallel plate transmission line.



any line is a reasonable first order approximation to this problem and has been the technique applied for many years at the NSCL.

The results of the first order analysis for a 90 degree corner is displayed in figure 7.5 Neglecting fringe effects, a first order solution to Laplace's equation for the 90 degree E-plane case displayed in figure 7.4 is:

$$V(x,y) = V_o \left(1 - \frac{x}{h}\right) \left(1 - \frac{y}{h}\right)$$

from which

$$E_x(y) = \frac{V_o}{h} \left(1 - \frac{y}{h}\right) , \quad E_y(x) = \frac{V_o}{h} \left(1 - \frac{x}{h}\right) ,$$

which results in a induced charge for a width "w" of

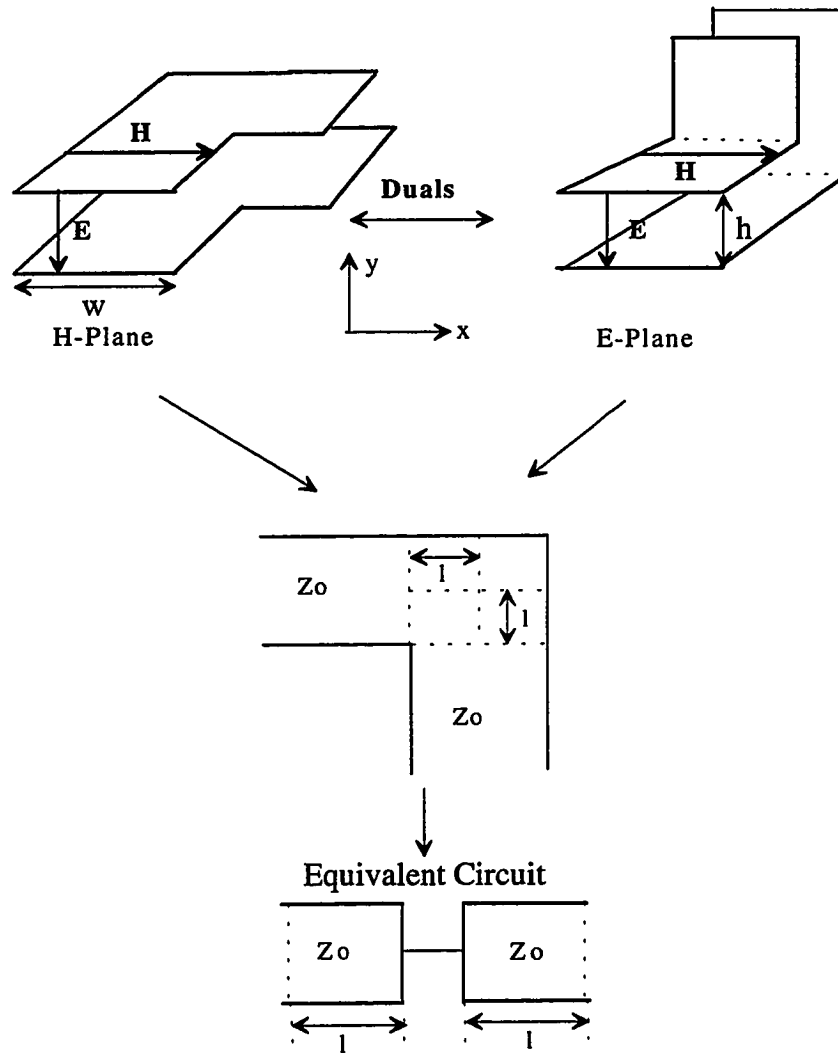
$$Q = w\epsilon_o V_o.$$

The magnetic field amplitude in the discontinuity is constant.

$$H_z = \frac{I_o}{w} \quad \Rightarrow \quad \Psi = \frac{\mu_o I_o}{w} h^2$$

Using the relationships developed for the magnetic flux and the electric charge, the total inductance and capacitance of the discontinuity is determined.

$$C = \frac{|Q|}{V_o} = w\epsilon_o \quad , \quad L = \frac{|\Psi|}{I_o} = \frac{\mu_o h^2}{w}$$



$$\text{E-Plane : } l = \frac{h}{2} \quad , \quad \text{H-Plane : } l = \frac{w}{2}$$

Figure 7.5 Modeling of 90 degree corners and bends in parallel plate transmission lines.

The inductance and capacitance per unit length of the normal transmission line is:

$$C = \frac{\epsilon_0 w}{h} \quad , \quad L = \frac{\mu_0 h}{w}$$

If both lines are extended one half way into the discontinuity as proposed in figure 7.5, then the total capacitance and inductance contributed by the lines is found by multiplying the capacitance and inductance per unit length by the total length  $2 \times l = h$  or  $w$ .

$$C = \frac{\epsilon_0 w}{h} h = \epsilon_0 w \quad , \quad L = \frac{\mu_0 h}{w} h = \frac{\mu_0 h^2}{w}$$

The above solution is seen to be equal to the solution obtained from the first order field analysis. Since the two solutions yield identical results, it is apparent that extending each line an appropriate distance into the discontinuity is a justifiable method of handling such situations. Although the analysis was performed for the E-Field discontinuity, the results for the H-Plane discontinuity yields the same results since it is the dual case. Therefore, for this case each line is extended according to the formulas:

$$\text{E-plane Bend} : l = \frac{h}{2} \quad , \quad \text{H-plane Bend} : l = \frac{w}{2}$$

The previous development was made for geometrically identical lines making a 90 degree corner. The results are easily reasoned to extend to cases where either the height or width differs for the two lines. If the width or height of each of the two lines entering and leaving a corner are different, then the lines are modeled as extending a different distance into

the corner. For this case, the formulas used to calculate the distance each line is extended into the corner are

$$\text{E-Plane Bend : } l_i = \frac{h_i}{2} \quad \text{or} \quad \text{H-Plane Bend : } l_i = \frac{w_i}{2}$$

where "i" denotes line 1 or 2. If the width abruptly changes for an E-plane corner, or the height changes abruptly for a H-plane corner, a discontinuity element must be included in the circuit model as described previously in the section on discontinuities.

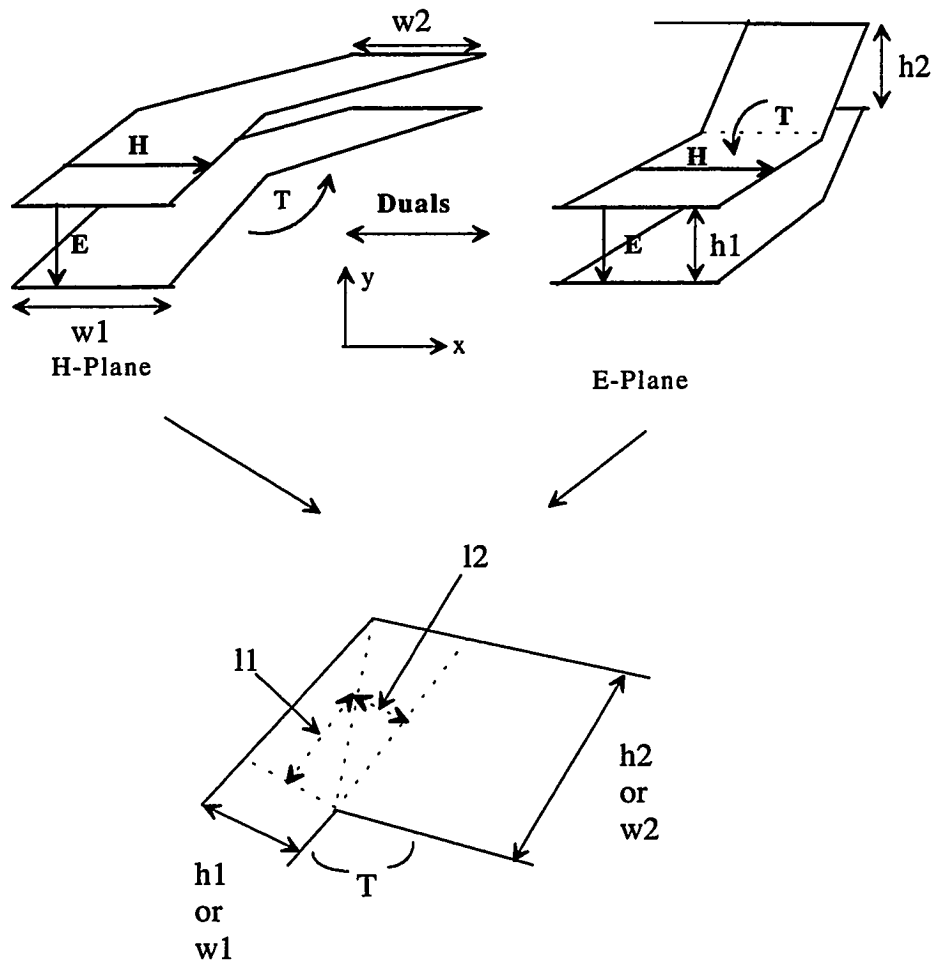
In addition to changes in height or width, the corner may differ from 90 degrees. Observing from the previous developments that the amount of capacitance or inductance accrued by the corner is calculable by the unperturbed field, the problem reduces to a geometric problem as shown in figure 7.6. In this case, for a corner of "T" degrees the following formulas apply.

$$\text{E-plane : } l = \frac{h}{2} \sin(T) \quad , \quad \text{H-Plane : } l = \frac{w}{2} \sin(T)$$

The formulas for changes in height or width may be combined to account for all the cases as:

$$\text{E-plane : } l_i = \frac{h_i}{2} \sin(T) \quad , \quad \text{H-plane : } l_i = \frac{w_i}{2} \sin(T)$$

Figure 7.6 summarizes the general case for corners. Transmission lines other than parallel plate lines will also be handled with this method and comparable results are expected.



H-plane Bend :  $l_i = \frac{w_i}{2} \sin(T)$  , E-plane Bend :  $l_i = \frac{h_i}{2} \sin(T)$

Figure 7.6 Summary of corners and bends.

## **CHAPTER EIGHT**

### **Nonstandard Transmission Lines 2: Non-Uniform Transmission Lines**

#### **8.1 Introduction**

This chapter describes and develops methods for handling non-uniform transmission lines; i.e., transmission lines that have a cross-section perpendicular to the guided wave axis (referred to as transverse) that varies along the guided wave axis. A technique for slicing the non-uniform transmission line into segments and then modeling each segment with a "Segment Equivalent Circuit" (SEC) consisting of two uniform transmission lines and an intervening discontinuity circuit is developed. The technique is tested by comparing its predictions to known theoretical and experimental results from the literature for exponentially tapered transmission lines [8.1]. Convergence criteria for applying the technique are then developed with a linearly tapered transmission line. The technique developed in this chapter is shown to converge with a  $k/N^2$  rate to results that match theoretical and measured results.

## **8.2 Tapered Transmission Lines**

### **8.2.1 The Tapered Line Circuit Model**

A great deal of literature exists for non-uniform transmission lines [8.1, 2.7, 8.3, 8.4, 8.5, 8.6, 8.7, 8.8]. The literature is concentrated on finding optimum tapers for impedance transformers [8.5, 8.6, 8.8] and resonant sections for microwave filters [8.1]. If the characteristic impedance is presumed to be known at each point along the taper, then the physical problem reduces to a Ricatti's differential equation in terms of the voltage reflection coefficient [8.1, 2.7]. A line with an exponentially varying characteristic impedance provides a natural solution to the Ricatti equation and is presumably why the exponentially tapered microstrip transmission line is emphasized in the literature. A particular set of analytical and experimental results for exponentially tapered resonators [8.1] will be used to verify the computer assisted linearly segmented method proposed here.

Tapered transmission lines will be modeled by geometrically slicing the line into a series of connected segments. Figure 8.1 shows two of the many possible types of tapers. Each segment is then transformed into a Segment-Equivalent-Circuit (SEC).

A frequently applied method for modeling a tapered transmission line is to create line segments which use the geometric averages of the original line to determine the electrical parameters of each segment. In this case, the equivalent circuit of each segment consists of a single line. The geometry of the equivalent segment is set to the value found half way

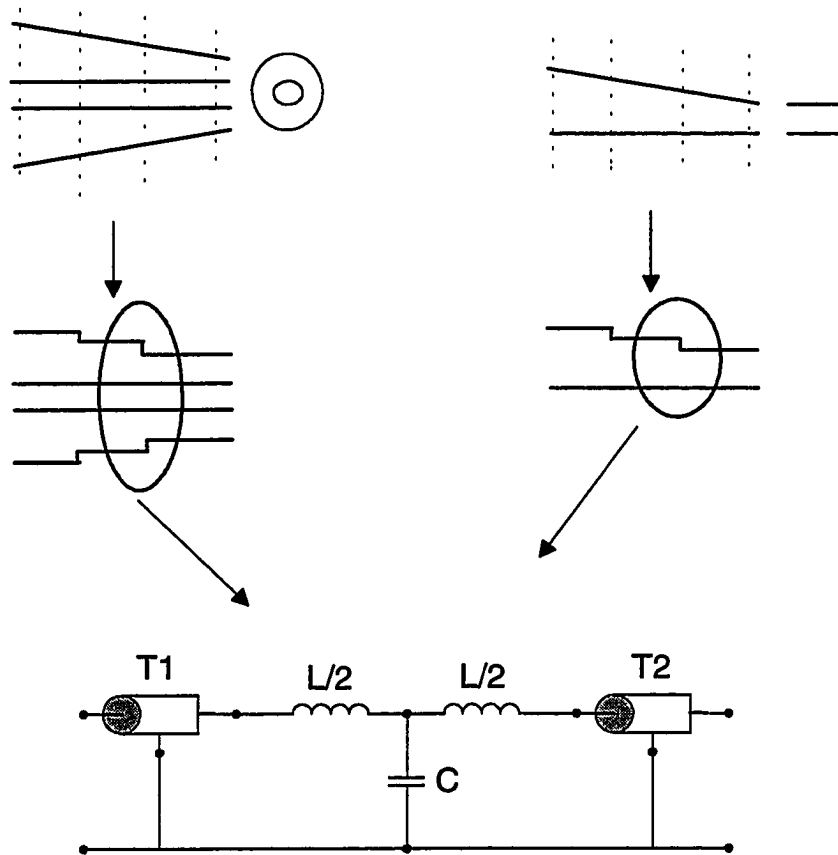


Figure 8.1 Two tapered transmission lines and the associated "Segment Equivalent Circuit" (SEC).



along the length of the tapered segment it represents. The effects of the perturbations of the electric or magnetic field due to the geometric variation along the length of the original line are ignored. This method is simple and yields acceptable results, although it does not maintain all of the electrical parameters of the original line.

The SEC applied here differs from the above technique by more fully accounting for the effects of the taper. The most general form of the SEC applied is shown in figure 8.1. Similar to the historical method, the original tapered transmission line is sliced into electrically short segments with each segment represented by a SEC circuit. Each SEC consists of two uniform transmission lines separated by a circuit that approximates the effect of the functional perturbations of the electric and magnetic fields due to the taper. Geometrically, the SEC is designed by assuming a model that represents the taper by two uniform transmission lines separated by an abrupt discontinuity representing the effect of the taper. Ideally the SEC would produce the same time delay, maintain the same net quantity of electric and magnetic energy (equivalently: maintain the same net capacitance and inductance), and produce the same losses as the original segment of line it represents. The tapered line is segmented along  $z$  such that: 1) the characteristic impedance of each segment may be modeled to vary linearly, and 2) each segment is sufficiently electrically short with respect to the highest frequency of interest to maintain an acceptable error tolerance.

Although the tapered transmission line operating in the transmission line mode contains  $z$ -directed field components, it is modeled to be operating in a TEM mode since the field shape of the  $z$ -directed

components are not due to the operating frequency and may be computed with static techniques. Using these ideas, the uniform transmission lines of the SEC are determined based on the line transverse geometry only and the effects of the z-directed field are approximated with a circuit whose components represent the geometric change along z by a geometrically abrupt discontinuity in the center of the segment.

### 8.2.2 The Transmission Line Segment

The reactive parameters for the transmission line segments are determined based on; 1) conserving the distance along the guided wave axes, 2) conserving the net electrostatic energy, 3) conserving the magnetostatic energy, and 4) conserving the material properties. The "Transverse Characteristic Impedance" denoted by " $Z_t$ " is computed using the transverse fields alone. The transverse characteristic impedance found at each end of the segment ( $Z_{t1}$  and  $Z_{t2}$ ) are used in the ensuing development. The conductor equivalent widths at each end of the original segment are known or are calculable with the numeric techniques described in chapter seven.

The following development determines the parameters of the SEC by conserving the electrostatic and magnetostatic stored energy as well as the losses of the original line. Defining the quantities  $C_1(z)$  and  $L_1(z)$  as

$$C_1(z) \equiv \frac{C_{11}}{g(z)} \text{ and } L_1(z) \equiv L_{11}g(z) \text{ where } g(0) \equiv 1$$

where  $C_{t1}$  and  $L_{t1}$  are defined as the "transverse capacitance" and "transverse inductance" per meter at  $z = 0$ , and  $g(z)$  is a user defined function. Using the above expressions, the transverse characteristic impedance at any point along the guided wave axis is determined as

$$Z_t(z) = \sqrt{\frac{L_{t1}}{C_{t1}}} g(z).$$

The net transverse capacitance and net transverse inductance is preserved by a uniform transmission line through the following development for the segment of length "l".

$$C_t = \frac{C_{t1}}{l} \int_0^l \frac{dz}{g(z)} \quad \text{and} \quad L_t = \frac{L_{t1}}{l} \int_0^l g(z) dz$$

which results in

$$Z_t = \sqrt{\frac{L_t}{C_t}}$$

Since, as part of the modeling requirement, each segment is taken short enough so that the transverse characteristic impedance is taken to vary linearly, it is presumed that  $g(z)$  is linear and may be modeled as  $g(z) = 1 + mz$ . Using this formulation for  $g(z)$  and applying the previous integrals for  $C_t$  and  $L_t$  results in:

$$C_t = \frac{C_{t1}}{ml} \ln(1 + ml) \quad \text{and} \quad L_t = L_{t1} \left( 1 + \frac{ml}{2} \right)$$

with

$$m = \frac{1}{l} \left( \frac{Z_{r2}}{Z_{r1}} - 1 \right) \equiv \frac{1}{l} (\tau - 1)$$

which results in

$$L_t = \frac{L_{r1}}{2} (\tau + 1) \text{ and } C_t = \frac{C_{r1} \ln(\tau)}{(\tau - 1)}.$$

The characteristic impedance for the equivalent section of line is then:

$$Z_t = \sqrt{\frac{L_t}{C_t}} = Z_{r1} \sqrt{\frac{1}{2} \frac{(\tau^2 - 1)}{\ln(\tau)}}$$

The segment losses may include conductor losses, dielectric losses, or magnetic losses. The predominant losses in the structures considered in this thesis are conduction losses. Since the electric and magnetic energy have been conserved in each SEC by the choice of characteristic impedance derived above, material losses for the intervening materials may be handled by specifying the quality factors for the isotropic linear dielectric material ( $Q_e$ ), and isotropic linear permeable material ( $Q_h$ ). The conductor losses are handled by assuming the equivalent conductor width, defined in section 7.2.2 and denoted by " $w_e$ ", for each end of the line segment being modeled varies linearly from one end to the other. Then the constant equivalent width for each conductor of the SEC is derived using the technique of this section.

If the line were uniform with a constant current, then the conduction losses for each conductor would be:

$$P_d = \frac{I_o^2 R_s l}{w_e}$$

In the above expression, " $w_e$ " represents a constant conductor width and " $l$ " represents the conductor length. If the conductor width varied from " $w_{e1}$ " to " $w_{e2}$ " over the length " $l$ ", then the losses would be:

$$P_d = I_o^2 R_s \int_0^l \frac{dz}{w_{e1} + \left(\frac{w_{e2} - w_{e1}}{l}\right)z} = \frac{I_o^2 R_s l}{w_{e2} - w_{e1}} \ln\left(\frac{w_{e2}}{w_{e1}}\right)$$

Equating the two expressions and solving for  $w_e$  yields

$$w_e = \frac{w_{e2} - w_{e1}}{\ln\left(\frac{w_{e2}}{w_{e1}}\right)}$$

The above expression is applied to each conductor of the tapered line.

### 8.2.3 Other Methods for Choosing $Z_t$

Other methods for choosing the transverse impedance exist. Some of these will be considered here in comparison to one another. Since the transmission line modes considered here have no lower cutoff frequency, the choice of  $Z_t$  should be valid under dc conditions. The other possible representations are compared to one another with respect to how well each

maintains the net electrostatic and magnetostatic energy. It is found that none of the representations considered can maintain both forms of energy simultaneously.

The modeling technique requires that  $Z_t$  be chosen to vary linearly as in the previous section. Since the group velocity is chosen to be the velocity in the medium, the definitions for capacitance per meter and inductance per meter defined before still hold.

$$Z_t = Z_{t1}g(z) , C_t = \frac{C_{t1}}{g(z)} , L_t = L_{t1}g(z)$$

As before, the parameters which bound the tapered line segment are  $Z_{t1}$ ,  $C_{t1}$ ,  $L_{t1}$  and  $Z_{t2}$ ,  $C_{t2}$ , and  $L_{t2}$  with  $g(z) = 1 + mz$  and  $m$  determined to maintain the begin and end line values. The "best" representation is taken to be the one that minimizes the error function

$$Error = \sqrt{(\Delta U_e)^2 + (\Delta U_h)^2} \times 100 \%$$

with

$$\Delta U_e = \frac{U_{ez} - U_e}{U_e} \text{ and } \Delta U_h = \frac{U_{hz} - U_h}{U_h}$$

where  $U_e$  and  $U_h$  represent the actual electrostatic and magnetostatic stored energy that would be measured and  $U_{ez}$  and  $U_{hz}$  represent the values predicted by the particular choice of determining  $Z_t$ . In practice, the values for the electrostatic and magnetostatic energy will be represented by a net capacitance and inductance respectively.

Four methods of resolving the linearly varying transverse characteristic impedance into a constant characteristic impedance are investigated. These methods include 1) conservation of total energy ( results from the previous section), 2) arithmetic mean, 3) geometric mean, and 4) conservation of electrostatic energy. The first method was derived in detail in the last section, so it need not be repeated here. Each of the other three will be tersely derived.

### 1. Conservation of Total Energy

$$Z_t = Z_{t1} \sqrt{\frac{1}{2} \frac{(\tau^2 - 1)}{\ln(\tau)}}$$

### 2. Arithmetic Mean

$$Z_t = \frac{Z_{t1} + Z_{t2}}{2}$$

### 3. Geometric Mean

$$Z_t = \sqrt{\frac{\frac{L_{t1} + L_{t2}}{2}}{\frac{C_{t1} + C_{t2}}{2}}} = \sqrt{Z_{t1} Z_{t2}}$$

### 4. Conservation of Electrostatic Energy

$$C_t = \frac{C_{t1} \ln(\tau)}{(\tau - 1)} \Rightarrow Z_t = \frac{1}{v C_t}$$

Table 8.1 shows that the conserved energy approach results in the minimum net error, while the geometric mean has the largest net error. The arithmetic mean perfectly conserves the magnetostatic energy at the expense of a larger error in the electrostatic energy while the conservation of electrostatic energy approach does exactly the opposite by perfectly maintaining the electrostatic energy at the expense of a larger error in the magnetostatic energy. Figure 8.2 plots the transverse characteristic impedance determined from each of the four methods for linear tapers varying from 10 to 100 Ohms as well as the error for each choice of  $Z_1$ .

Table 8.1 Percent Error for the Four Choices of  $Z_1$

<b>Taper <math>Z_{02}/Z_{01}</math></b>	<b>Conservation of Total Energy</b>	<b>Geometric Mean</b>	<b>Arithmetic Mean</b>	<b>Conservation of Electrostatic Energy</b>
1	0.00	0.00	0.00	0.00
2	2.73	6.06	3.82	3.82
3	6.49	14.34	8.97	8.97
4	9.84	21.62	13.44	13.44
5	12.70	27.80	17.15	17.15
6	15.14	33.09	20.27	20.27
7	17.26	37.68	22.91	22.91
8	19.10	41.73	25.19	25.19
9	20.74	45.35	27.18	27.18
10	22.20	48.62	28.93	28.93



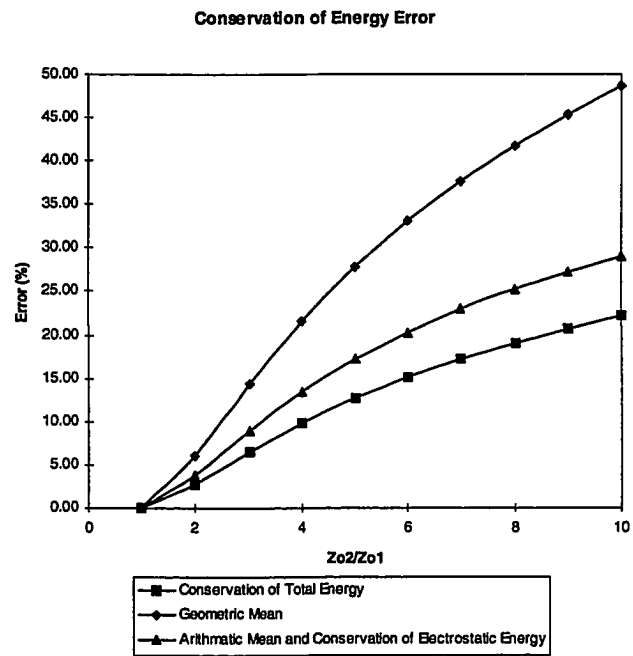
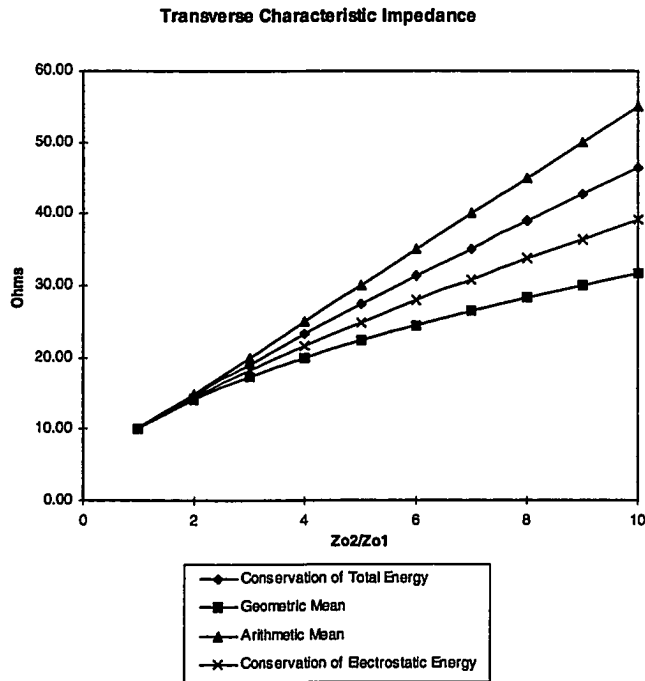


Figure 8.2 A comparison of the choices for the transverse impedance.

### 8.3 An Exponentially Tapered Transmission Line

A solution to the exponentially tapered transmission line was previously developed by Womack [8.1]. (Keep in mind that an exponentially tapered transmission line is one in which the characteristic impedance varies exponentially). The solution was based on an exact solution to the Riccati differential equation developed by Sugai [8.9, 8.10]. The work by Womack is used to test the SEC developed here. The solution developed by Womack is outlined here for background.

In the TEM mode of propagation, the differential equations which represent the voltage and current on the transmission line as a function of location on the line are

$$\frac{dV}{dz} + Z(z)I = 0 \quad , \quad \frac{dI}{dz} + Y(z)V = 0$$

where  $Z(z)$  and  $Y(z)$  are the series impedance and shunt admittance per meter of line, respectively. Differentiation of the above set of equations yields the familiar set of second order linear differential equations:

$$\frac{d^2V}{dz^2} - \frac{1}{Z} \left( \frac{dZ}{dz} \right) \left( \frac{dV}{dz} \right) - YZV = 0 \quad , \quad \frac{d^2I}{dz^2} - \frac{1}{Y} \left( \frac{dY}{dz} \right) \left( \frac{dI}{dz} \right) - YZI = 0$$

Sugai [8.9] has shown that these second-order linear differential equations yield a general Riccati's differential equation

$$\frac{dr}{dz} + P_1(z)r + Q_1(z)r^2 = Q_1(z),$$

where  $r$  is the voltage reflection coefficient defined by

$$r(z) = \frac{V - IK_o(z)}{V + IK_o(z)},$$

and

$$K_o(z) = \sqrt{\frac{Z(z)}{Y(z)}}, \quad P_1(z) = -2\sqrt{Z(z)Y(z)}, \quad Q_1(z) = -\frac{1}{2K_o(z)} \left( \frac{dK_o(z)}{dz} \right).$$

For the exponentially tapered transmission line, the characteristic impedance is chosen to vary exponentially as

$$K_o(z) = K_{01} e^{\delta z}.$$

Using the above definition, and assuming negligible losses, the differential equation for an exponential transmission line is

$$\frac{dr}{dz} - 2\frac{\gamma}{\delta}r + \left(\frac{\delta}{2}\right)(1 - r^2) = 0,$$

whereby using transforms discovered by Sugai [8.10] to reduce the above equation to a first order linear differential equation the solution is found to be

$$r(z) = 2\frac{\gamma}{\delta} + A \frac{1 - B \tanh\left(\frac{\delta Az}{2}\right)}{\tanh\left(\frac{\delta Az}{2}\right) - B},$$

where

$$A^2 = 1 + 4\frac{\gamma^2}{\delta^2},$$

$$B = \frac{A - \left(r_o - 2\frac{\gamma}{\delta}\right) \tanh\left(\frac{\delta Al}{2}\right)}{A \tanh\left(\frac{\delta Al}{2}\right) - \left(r_o - 2\frac{\gamma}{\delta}\right)},$$

$$\gamma = j\beta = j\frac{2\pi}{\lambda}.$$

A so-called "antiresonant" section of short-circuited transmission line with a short at position "l" has boundary conditions

$$r(l) = -1 \text{ and } r(0) = +1.$$

Solving for the length of line needed to achieve the imposed boundary conditions yields

$$l_n = \frac{n\pi + \tan^{-1}\left(\frac{4\beta^2}{\delta^2} - 1\right)^{\frac{1}{2}}}{\beta\left(1 - \frac{\delta^2}{4\beta^2}\right)^{\frac{1}{2}}} \frac{\lambda}{4}.$$

The fundamental ( $n = 0$ ) mode is compared to the results obtained from simulating exponential resonators for five different tapers using the technique described in the previous section to develop an equivalent circuit. The simulations are performed using the RESON computer

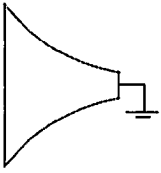
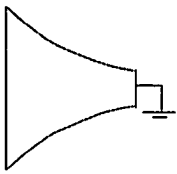
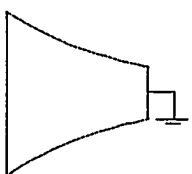
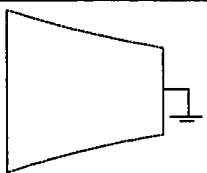
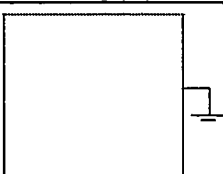
	Theoretical	Simulated	
$\frac{\delta}{\beta}$	$\frac{l}{\left(\frac{\lambda}{4}\right)}$	$\frac{l}{\left(\frac{\lambda}{4}\right)}$	$Z_0$ Taper
2.0	0.637	0.637	
1.5	0.696	0.696	
1.0	0.770	0.770	
0.5	0.867	0.867	
0.0	1.0	1.00	

Figure 8.3 The simulated exponential ( $Z_0$ ) line versus theory.

program as described in section 4.3. The results for each tapered line are found for a fixed resonant frequency of 500 MHz.

Figure 8.3 displays the theoretical results obtained from the above equation and the simulated results. The data for the simulated results in figure 8.3 are for the case where the true characteristic impedance " $Z_o$ " (in contrast to the transverse characteristic impedance " $Z_t$ ") varies exactly exponentially. Figure 8.4 displays the results that were measured by Womack for various microstrip transmission lines with exponentially varying  $Z_t$  (i.e. exponentially varying  $Z_t$  versus  $Z_o$ ) after removing the end effects. Also shown in figure 8.4 for comparison is the results obtained from the simulation which includes discontinuity elements to model the effects of the taper. The simulations converged to within 0.1% when the line was sliced into nine or more equal length segments with each segment modeled with a SEC as described. All of the simulations sliced the line into 18 segments.

The line built by Womack had an exponentially varying  $Z_t$  versus the exponentially varying  $Z_o$  that is the basis of the theoretical result. This can be seen in figure 8.5 by the fact that when the theoretical case is compared to the simulated case for an ideal exponentially varying taper, the result matches theory to within 0.04%. Next, the simulated results are shown to shift closer to the measured results when the model is modified by adding discontinuity elements to account for the longitudinal fields with  $Z_t$  varying exponentially. Although the results shift closer to the experimental data, some other effect is evident in the measured data that causes an additional discrepancy which can easily be seen in the measured data for the well

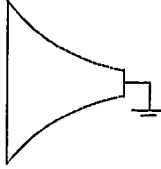
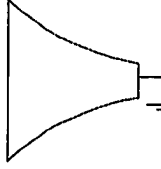
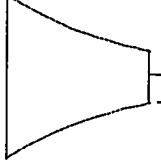
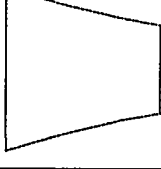
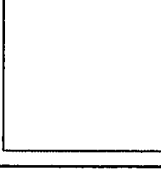
	Measured	Simulated	
$\frac{\delta}{\beta}$	$\frac{l}{\left(\frac{\lambda}{4}\right)}$	$\frac{l}{\left(\frac{\lambda}{4}\right)}$	$Z_1$ Taper
2.0	0.626	0.627	
1.5	0.688	0.687	
1.0	0.755	0.760	
0.5	0.840	0.857	
0.0	0.990	0.999	

Figure 8.4 The simulated exponential ( $Z_1$ ) line versus measured results.

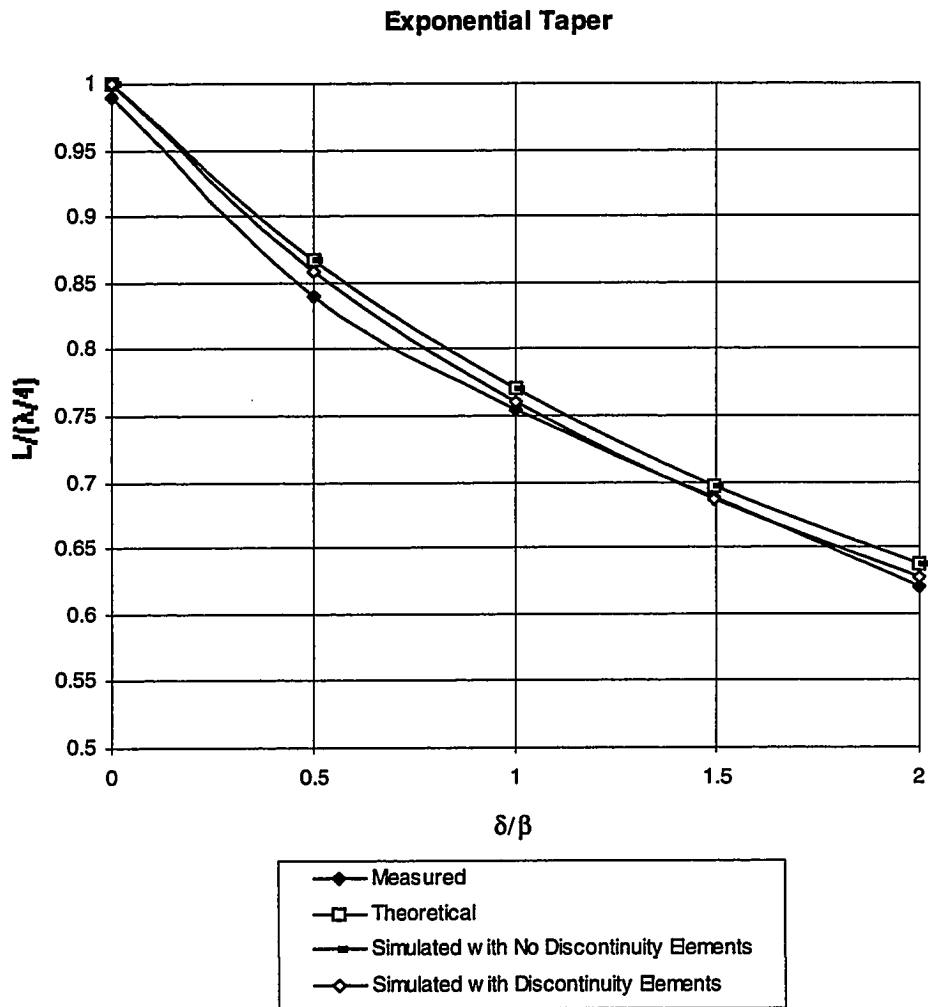


Figure 8.5 A plot of the exponentially tapered transmission lines results.



known simple case of no taper. The experimental data for the case of no taper (uniform) case differs by 1% from what it should be (an untapered line should be exactly  $1/4$  wavelength long at resonance) whereas the simulation is within 0.1% of the correct value. Some other unknown effect in the measured data in the region where the abscissa of the graph shown in figure 8.5 varies from 0.0 to 1.0 is likely responsible for the additional error between the simulated versus measured results in this region. This effect is probably also responsible for the obvious 1% discrepancy in the case of no taper.

#### **8.4 A Linearly Tapered Transmission Line**

Having established the validity of the technique in the previous section on exponential transmission lines, this section will establish a convergence criteria for segmentation based on the slope of the linear taper. The results are determined by multiple computer simulations using RESON for transmission lines with linearly tapered  $Z_0$ . Since the previous section has shown that the converged solution matches the theoretical solution nearly exactly, the converged solution will be taken as identical to the theoretical solution in this study.

##### **8.4.1 Development of the Segmentation Convergence Criteria**

A set of simulations were performed for transmission lines with a linearly tapering characteristic impedance ( $Z_0$ ) where the ratio of begin line to end line impedance, varies from 1 ( no taper ) to 10. The length of the

line was held constant to 15 cm corresponding to a 500 MHz quarter-wave resonator for the case of no taper. For a given taper, solutions were found for 1 to N segments in order to establish the convergence criteria. Figure 8.6 displays the result for the five tapers that were analyzed. Figure 8.7 shows the convergence characteristics for the resonant frequency and equivalent shunt circuit elements for four different tapers. Figure 8.8 displays some constant error curves for this case. Each curve in the figure represents the minimum number of SECs (the graph ordinate) necessary to maintain an error of less than the labeled amount for linearly tapered quarter-wave resonator.

Based on the results, the solution is observed to converge rapidly with a convergence that may be modeled as

$$error \propto \frac{k}{N^2}$$

where "k" is a constant and "N" is the number of SECs.

The constant error curves in figure 8.8 may be used as an aid to determine the segmentation necessary to achieve a desired error margin for an arbitrary section of line being modeled. To do this, the value of the abscissa of figure 8.8 must be determined from the parameters of the section being modeled. Using  $\tau$  and the electrical length ( $\beta l$ ) of the section being modeled at the highest relevant frequency, the abscissa value ( $Z_{o2}/Z_{o1}$ ) of figure 8.8 may be determined for the section from:

$$\frac{Z_{o2}}{Z_{o1}} = \left( \frac{\pi}{\beta l} \right) (\tau - 1) + 1$$

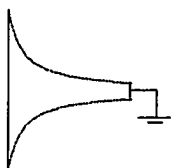
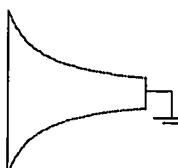
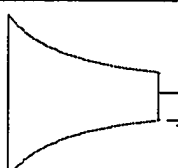
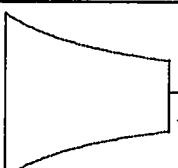

	Simulated	
$Z_{o2}/Z_{o1}$	$\frac{l}{\left(\frac{\lambda}{4}\right)}$	$Z_1$ Taper
10.0	0.635	
6.0	0.710	
4.0	0.780	
2.0	0.840	
0.0	1.00	

Figure 8.6 An overview of the linearly tapered transmission line study.

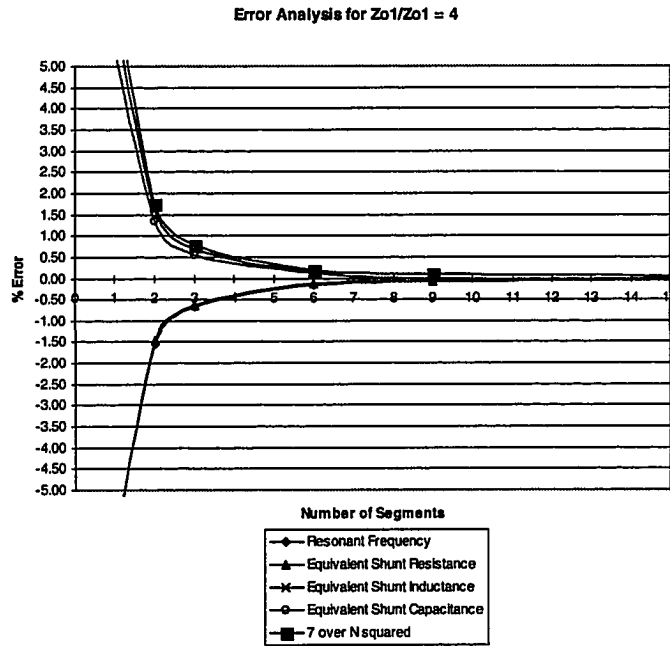
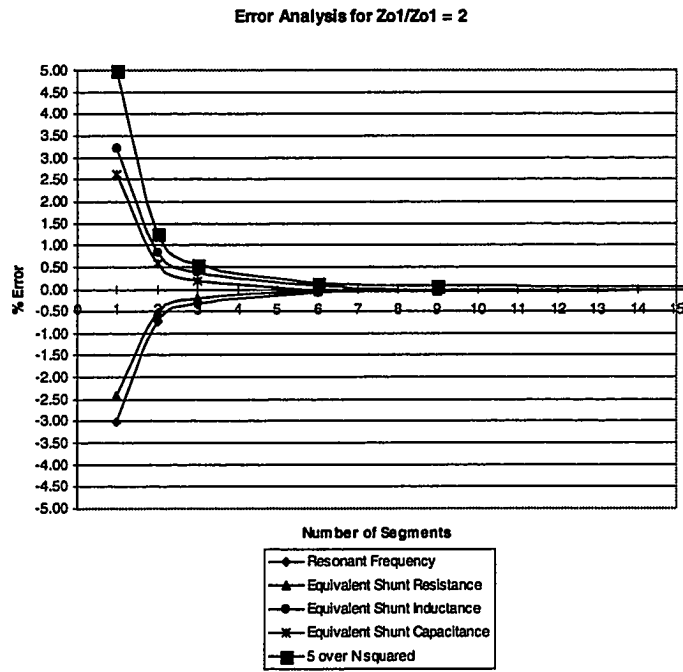
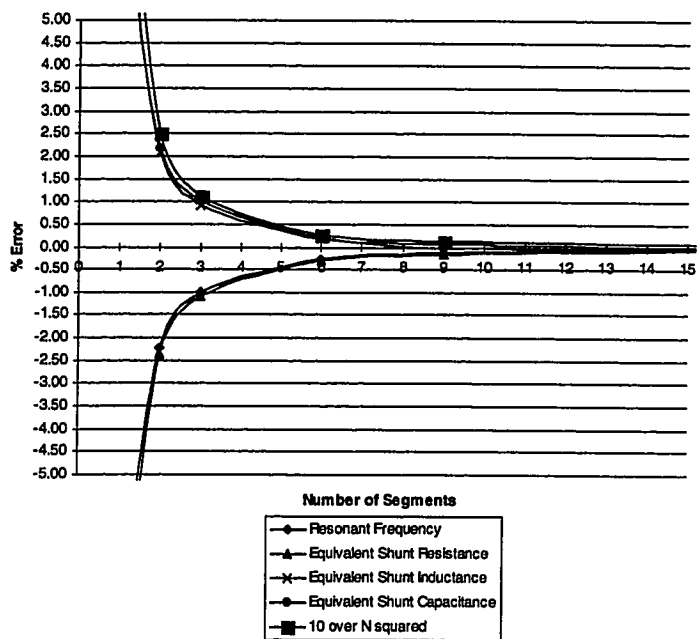


Figure 8.7 Plots of the convergence versus segmentation for linearly tapered quarter-wave resonators.

Error Analysis for  $Z_{o1}/Z_{o1} = 6$



Error Analysis for  $Z_{o1}/Z_{o1} = 10$

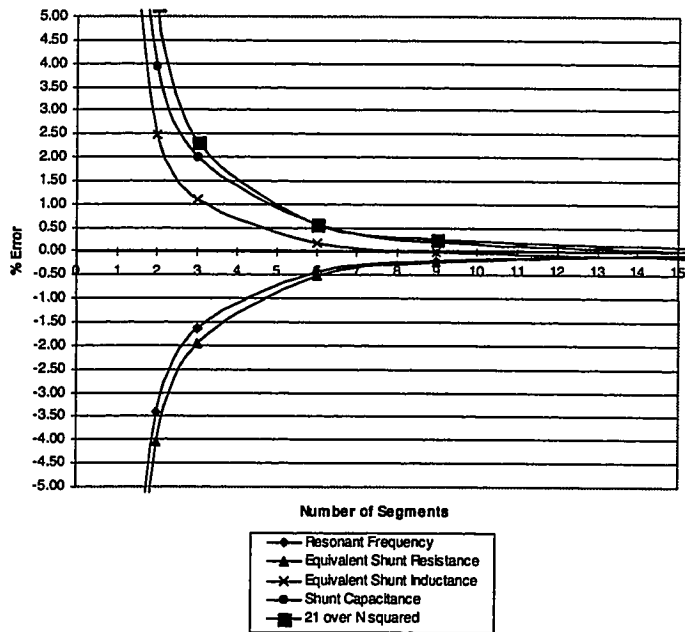
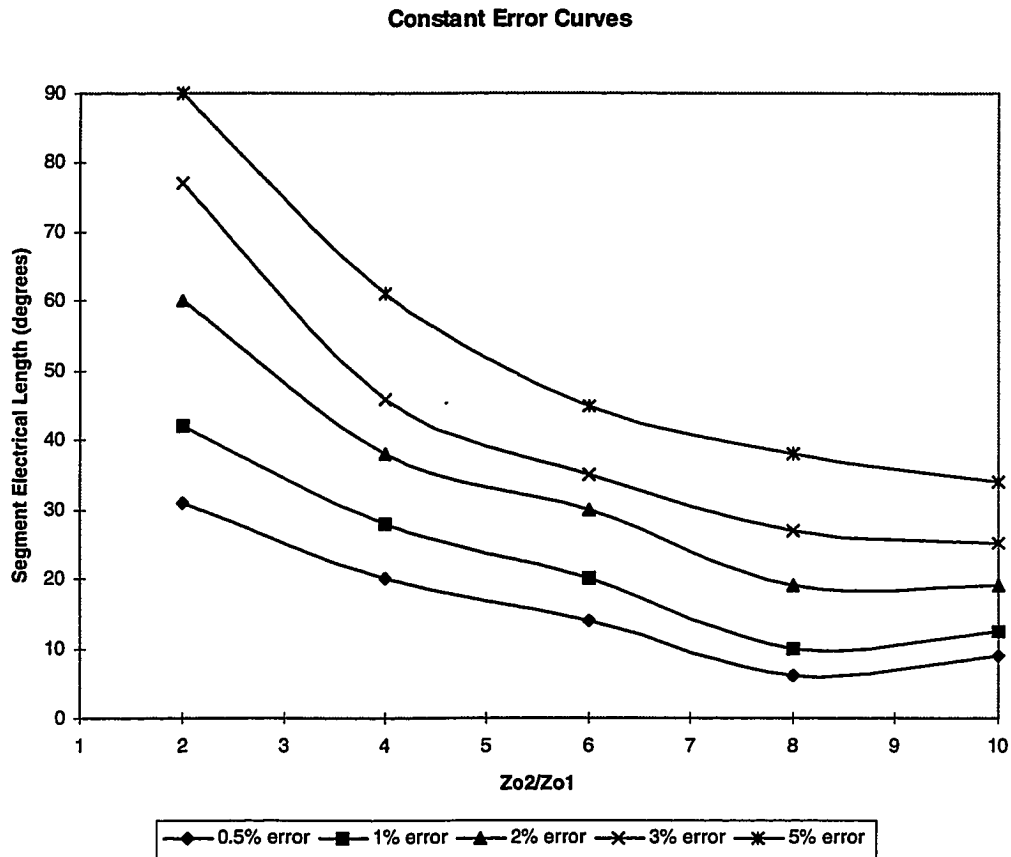


Figure 8.7 (continued)



**Figure 8.8** Constant error curves for linearly tapered quarter-wave resonators.

### 8.4.2 The Non-Uniform Tapered Transmission Line Modeling Process

The previous sections have shown that solutions based on the SEC developed converge to within an acceptable tolerance with reasonably finite segmentation. Arbitrarily complex geometries may have significantly more complicated behavior than the simple quarter-wave exponential and linearly tapered transmission line resonators used to establish these results. The results of the previous sections may be used to obtain an initial engineering estimate of the expected error versus slope and segmentation.

A five-part process can be used to model and analyze an rf structure to within a known error tolerance. The first part of the process requires that a maximum frequency of interest be specified since the accuracy required is a function of frequency. This frequency is used to determine  $\beta l$  for use in the previous expression for  $Z_{o2}/Z_{o1}$ . For example, a resonator may be designed to work over a well known frequency band where good accuracy is desired, while the harmonic behavior may also be a parameter of interest but at a lower accuracy. In the case of the K1200 cyclotron, a error tolerance of less then or equal 0.5% at 27 MHz is desired and an error tolerance less than or equal to 5 % at the fifth harmonic ( 135 MHz ) is desirable.

The step-by-step procedure is as follows:

1. Slice the resonator up sufficiently so that the transverse characteristic impedance " $Z_t$ " varies linearly.
2. Further slice up each segment, found in step 1, as needed to fall within an acceptable error tolerance using error estimates obtained from figure 8.8.
3. Analyze the structure using RESON and determine the circuit sensitivity to each element based on the energy the element manages and the power the element dissipates versus the circuit total energy as discussed in section 5.6.
4. For non-uniform sections that manage a significant amount of circuit energy, where corroborating measurements are not available, double the segmentation and re-analyze the circuit.
5. Establish the convergence rate with the  $k/N^2$  law, and when the change from iteration to iteration falls within the acceptable error tolerance, stop.



## **CHAPTER NINE**

### **Development of the K1200 Cyclotron RF Resonator Equivalent Circuit**

#### **9.1 Introduction**

The K1200 cyclotron rf system is comprised of the cyclotron resonators and couplers, the power amplifier chains, high power bias supplies, tuning servo mechanisms, and many electronics modules used for monitoring, regulation, equipment interlocks, process sequencing, safety interlocks, and supervisory remote controls. The purpose of the equipment is to safely and efficiently apply peak voltages of 50 kV to 180 kV at frequencies varying from 9.5 to 26.5 MHz to the charged particle accelerating electrodes historically referred to as "Dees" within the cyclotron. This chapter covers the modeling of the K1200 cyclotron resonators which were first energized on January 15, 1988.

#### **9.2 Resonator Configuration**

An overview of the rf resonator is shown in figure 9.1. It is important in this system for the dee voltage to be balanced about the median plane of the cyclotron. To maintain the balance, the resonators are designed to be symmetric about the median plane. Due to the symmetry, the upper and lower resonators may be analyzed separately as independent quarter

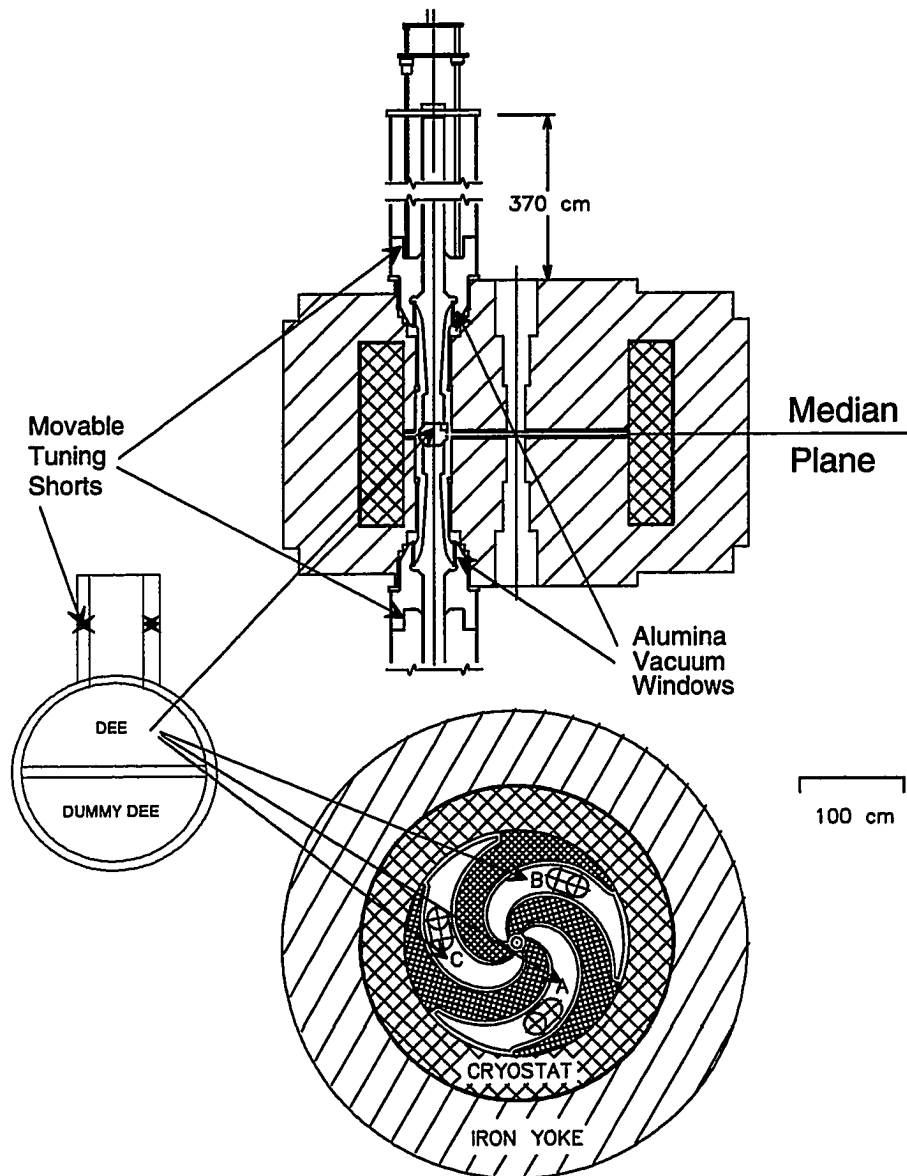


Figure 9.1 An overview of the K1200 cyclotron rf resonators.

wave structures. When the upper and lower resonators are perfectly balanced, no reactive current crosses the intervening boundary. However, a slight imbalance in the design occurs because the power needed to drive the system is only coupled into the lower resonator. This asymmetry is caused by the addition of the rf input coupler to the lower resonator. The asymmetry results in some reactive current (current that differs in phase from the voltage by 90 degrees) and some real component of current (current in phase with the voltage) to cross the median plane. Due to the high dee voltage, the real component of current that must cross the cyclotron median plane to drive the upper resonator is inconsequential.

### **9.3 Developing the Resonator Model**

As introduced in section 1.5.2, the equivalent circuit method is a three step process. The steps include 1) determining a circuit topology, 2) determining the electrical parameters for each element of the circuit, and 3) analyzing the circuit to determine the response. Steps one and two are developed in this chapter. Step three is accomplished in chapter ten.

The first step of the modeling process requires that the resonator be represented by a suitable circuit topology. The skeletal circuit diagram providing a reasonable representation of the K1200 resonator is shown in figure 9.2. The skeletal diagram does not include all of the model details necessary, but rather provides an overview of the structure suitable for initial modeling considerations. The details of the model will be presented

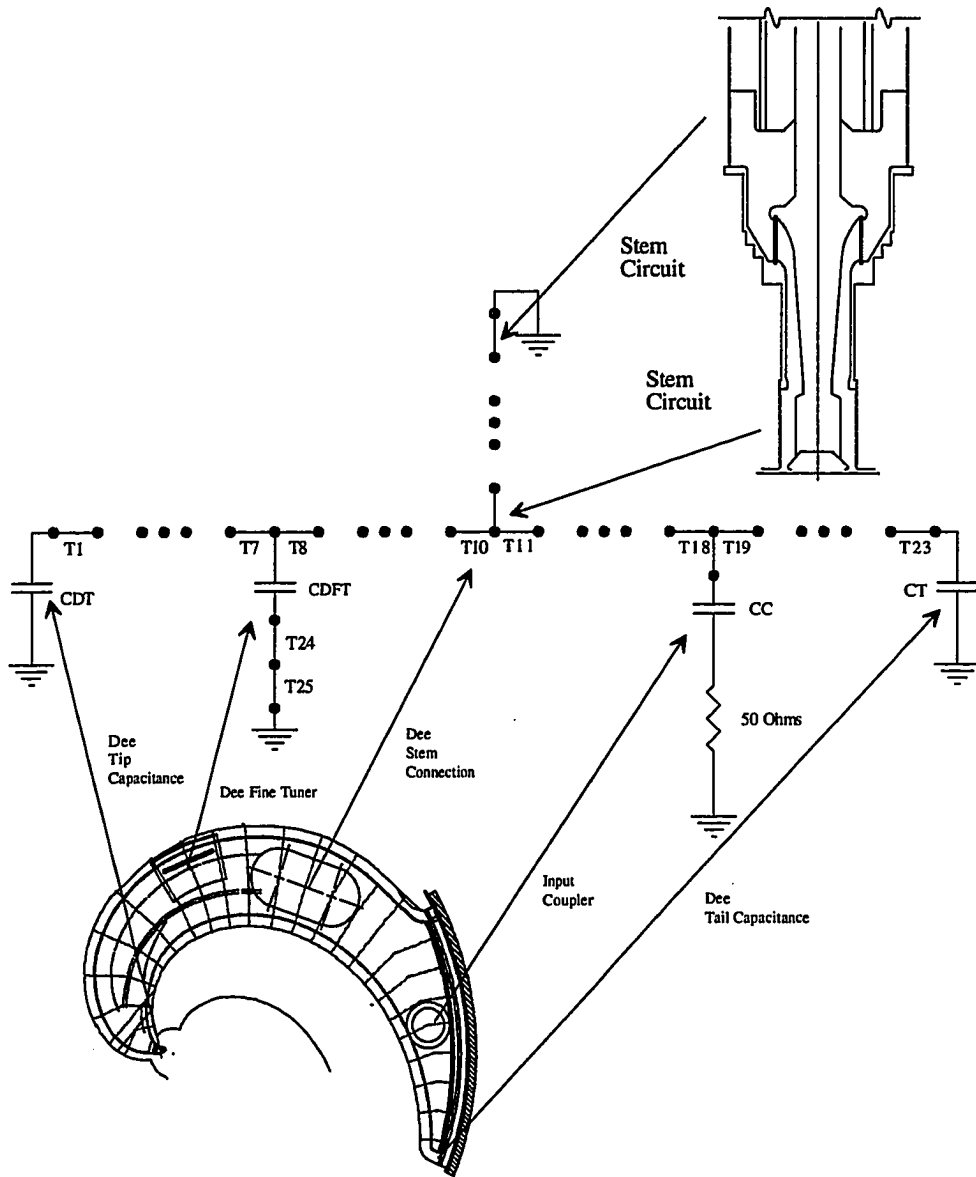


Figure 9.2 The K1200 resonator quarter wave section circuit topology.

in the ensuing discussion, figures, and tables. The model presented includes the transmission line behavior of the dee and tuning stem, the power input coupling, the abrupt discontinuities, and the joint resistances. This step of the process is qualitative and the model is not unique.

In step two, the cross-sections of the resonator are taken at several locations along the presumed transmission lines as shown in figure 9.3 for the dee. Each of the cross-sections is analyzed to determine the electrical parameters needed to parameterize the transmission line Segment Equivalent Circuit (SEC). The degree of segmentation for the circuit analysis is set by the requirements that all parameters vary linearly along each non-uniform segment, and that each segment is sufficiently short electrically at the highest frequency of interest to maintain the desired accuracy. Due to the requirement that the transverse characteristic impedance ( $Z_t$ ) varies linearly, the transverse characteristic impedance in the middle of a segment is simply the average of the value at the ends, so that doubling the segmentation to infer the error from the  $1/N^2$  law as described in section 8.4.1 is possible.

If desired, a smooth function for each of the electrical parameters may be obtained by applying a smoothing algorithm for each of the electrical parameters obtained from the cross-sections against a variable defined along the guided wave path. The values of the electrical parameters used to define the transmission line segments may be taken from these smoothed data curves at any point along the curve versus directly from the cross-section locations. Parameterization of the functions in this way allows the modeler to choose the degree of segmentation

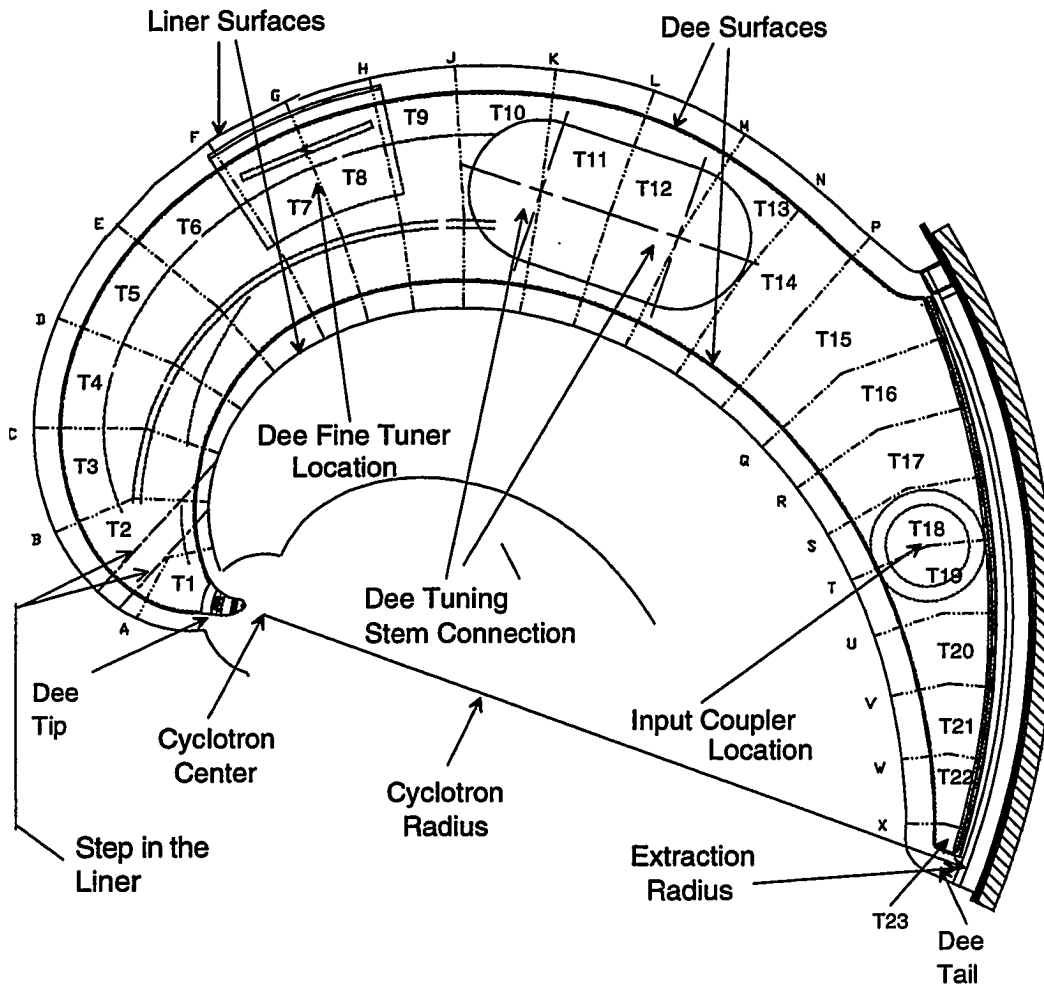


Figure 9.3 The top view of the K1200 dee showing the cross-sections to be analyzed.

independent of the number of analyzed cross-sections provided the smoothed curves are an accurate representation of the actual variation of each electrical parameter.

When the overall resonator response is thought to be relatively insensitive to the component being modeled, and a rigorous attempt at determining the "best" estimate of the element would be very time consuming, then crude estimates referred to as "back-of-the-envelope" techniques are applied to determine values for the component. The next step of the modeling process is to determine the electrical parameters of each element of the circuit model.

## **9.4 Determining the Element Values.**

### **9.4.1 The K1200 Dee Elements**

The dee modeling process must provide for determining the capacitance of the "Dee Tip" (CDT), the "Dee Tail" (CT), the effect of the "Dee Fine Tuner" (CDFT, T8, T9), and the general distributed dee model consisting of series transmission lines (T1 - T23) as shown in figure 9.3. This section will determine the component values for each of these elements.

The cross-sections for the dee shown in figures 9.3 and 9.4 are analyzed to determine the transmission line electrical parameters. The results are summarized in table 9.1. The cross-sections are taken to be a suitable distance apart to model the variation of the electrical parameters along the dee linearly as required by section 8.2.2. In addition, the

surfaces of the dee and liner are nearly parallel to each other so by taking the cross-sections orthogonal to these surfaces the electric field vector lies predominantly in the plane defined by the cross-section. Making the cross-sections in this way, and inferring a qualitative extension from the section 7.4 on corners, the electrostatic energy is accounted for and the need for additional circuit elements is eliminated.

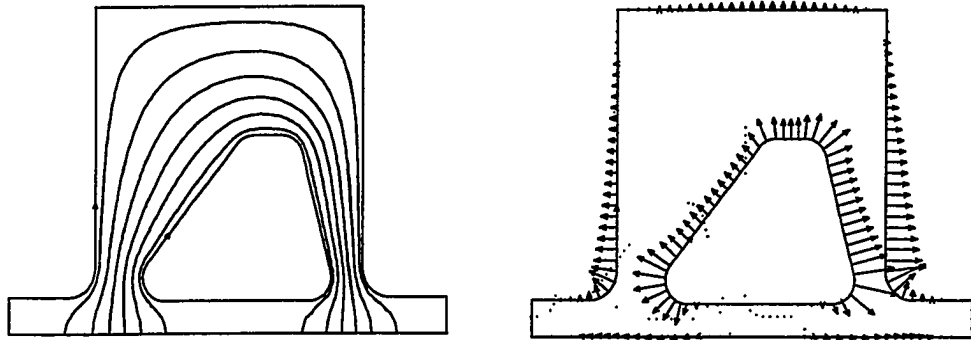
The electrostatic analysis is performed with the finite element package called "COSMOS" , discussed in chapter 4, and some additional software written for this application. Two representations of each cross-section are shown in figure 9.4 with one including the equal potential contour plots and the other the electric field plots for each conductor. The electric field vector strength is depicted by its relative length as compared to the other vectors on the cross-section. The electric field data for each conductor, calculated by COSMOS, was post processed as described in chapter 7 to determine the conductor width and equivalent conductor width for the dee ( $w_d, w_{de}$ ) and the liner ( $w_l, w_{le}$ ). A simple trapezoidal integration algorithm was applied to evaluate the integrals numerically.

$$w = \int_0^l dl \quad , \quad w_e = \frac{\left[ \int_0^l |E_s| dl \right]^2}{\int_0^l |E_s|^2 dl}$$

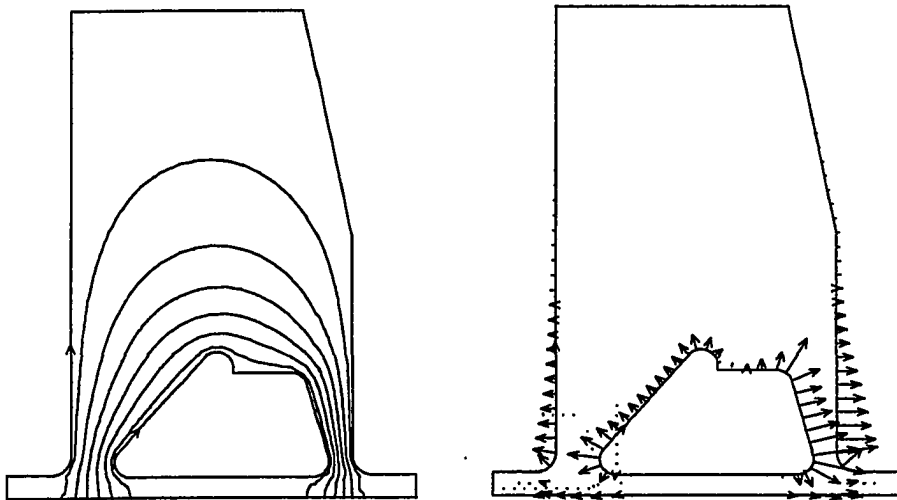


Table 9.1 Results of K1200 Dee Cross-section Analysis

<b>Cross-section</b>	<b>Parametric Coordinate (cm)</b>	<b>Zo (Ohms)</b>	<b>wd (cm)</b>	<b>wde (cm)</b>	<b>wl (cm)</b>	<b>wle (cm)</b>
<b>A</b>	5.61	47.20	33.25	23.22	86.23	31.90
<b>B</b>	15.83	45.76	47.57	25.20	150.55	35.84
<b>C</b>	26.60	45.46	59.44	32.41	160.22	38.35
<b>D</b>	37.37	49.02	65.89	38.33	165.48	53.14
<b>E</b>	48.49	50.95	70.05	39.29	173.05	59.44
<b>F</b>	61.32	48.90	73.43	40.03	179.22	69.11
<b>G</b>	70.90	50.19	77.01	42.90	173.71	63.35
<b>H</b>	80.23	49.41	79.25	46.18	177.32	66.78
<b>J</b>	89.67	48.75	81.41	46.79	178.03	67.95
<b>K</b>	100.78	61.03	63.22	33.55	178.59	50.01
<b>L</b>	111.76	61.01	63.73	33.63	179.73	51.31
<b>M</b>	122.67	61.50	62.10	33.20	176.68	50.85
<b>N</b>	133.16	62.14	59.31	32.28	173.79	49.61
<b>P</b>	142.34	62.82	57.25	32.16	173.91	49.02
<b>Q</b>	155.12	63.81	61.39	33.53	164.74	51.41
<b>R</b>	164.15	66.64	54.13	31.55	158.93	52.27
<b>S</b>	173.42	70.09	47.19	28.65	154.23	49.02
<b>T</b>	181.68	74.27	41.35	26.19	147.75	44.98
<b>U</b>	191.51	80.91	33.35	21.69	141.45	40.67
<b>V</b>	201.23	88.89	25.58	17.50	135.69	37.49
<b>W</b>	211.29	101.75	18.16	13.36	126.52	31.60
<b>X</b>	221.18	118.54	11.40	9.14	121.74	27.53
<b>SecTC</b>		48.45	56.44	38.86	148.26	54.74

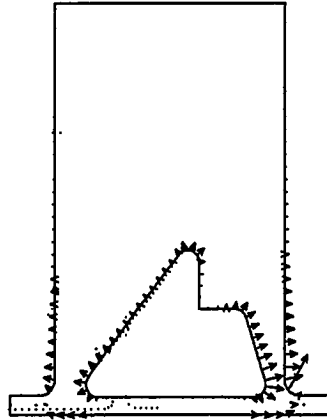
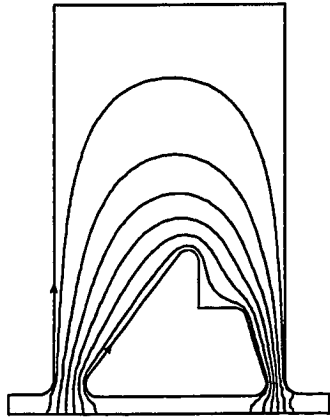


Section A

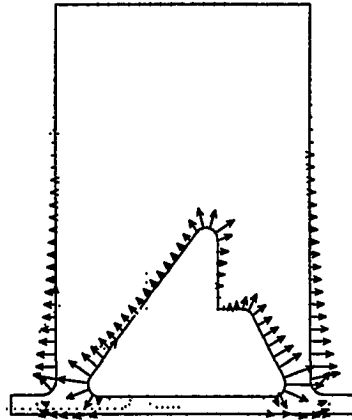
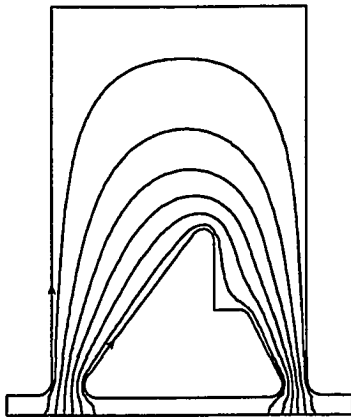


Section B

Figure 9.4 The K1200 dee cross-sections (not to scale).

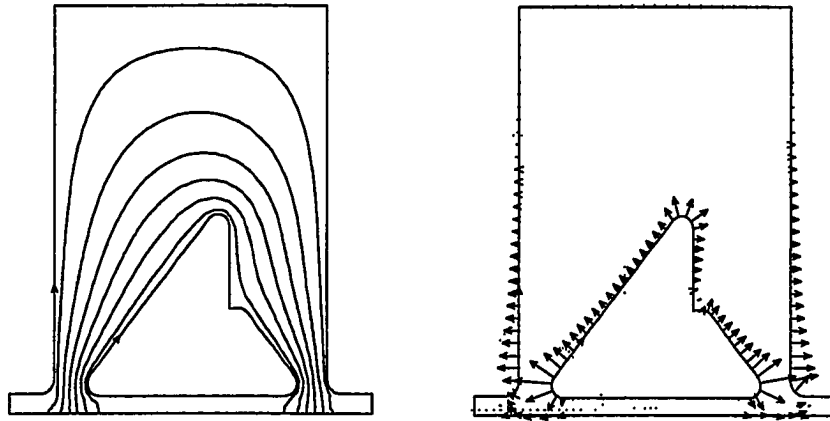


Section C

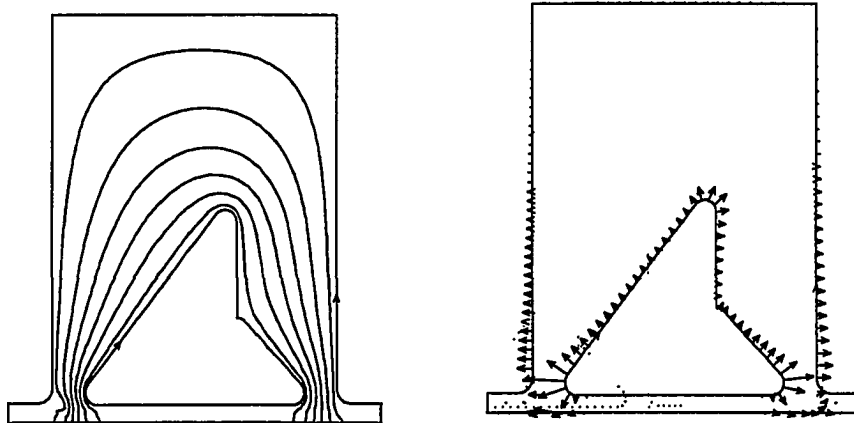


Section D

Figure 9.4 (continued)

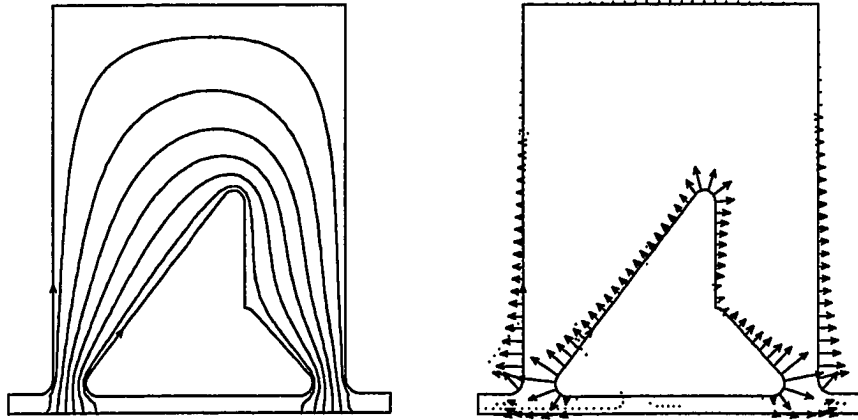


Section E

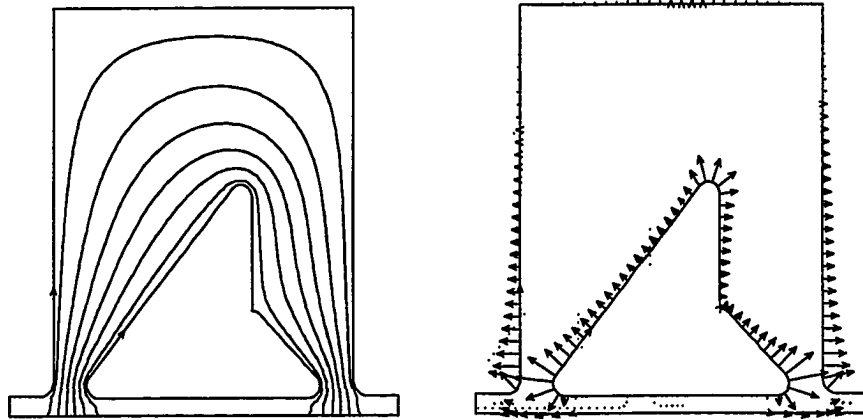


Section F

Figure 9.4 (continued)

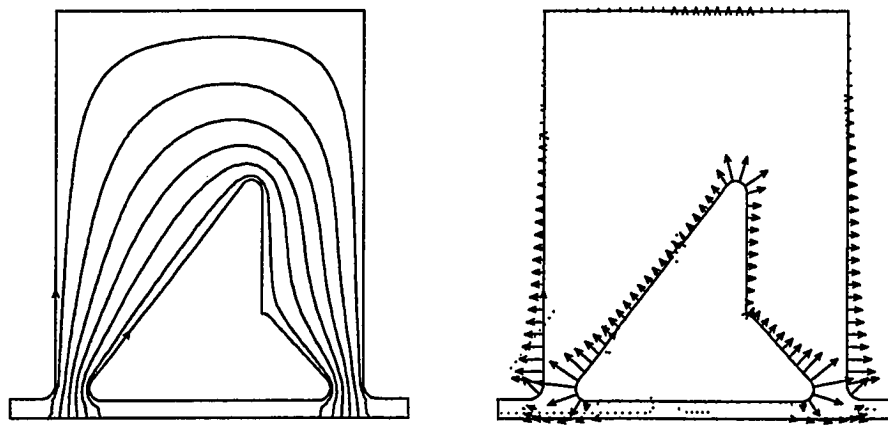


Section G

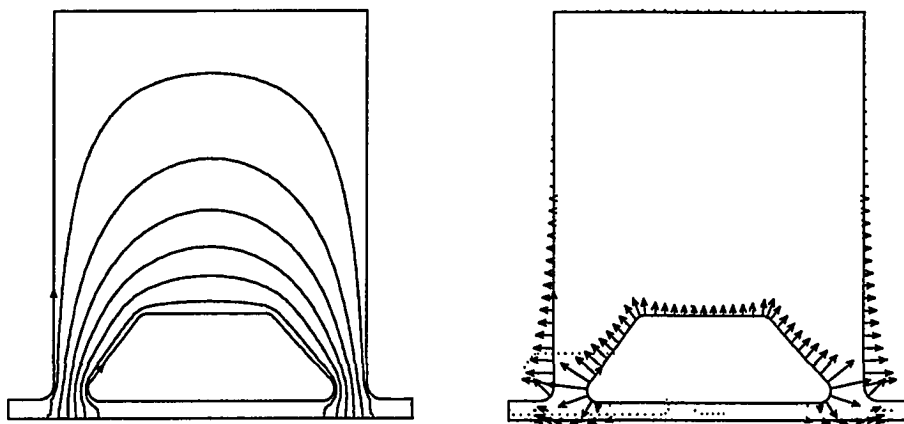


Section H

Figure 9.4 (continued)

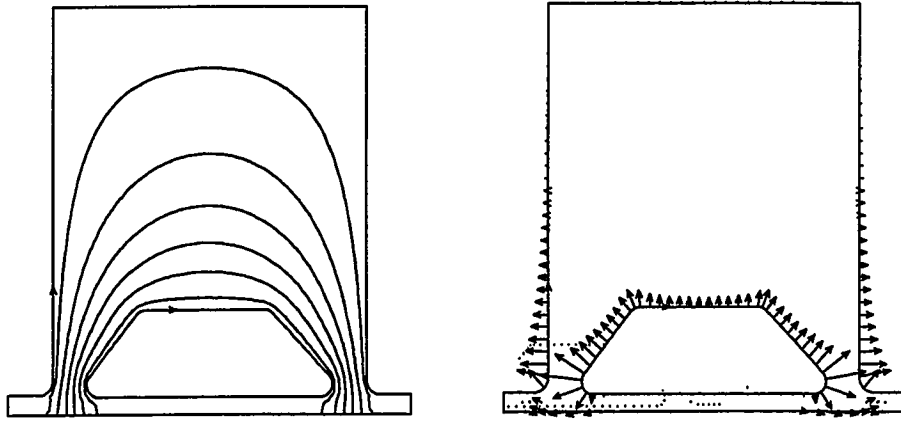


Section J

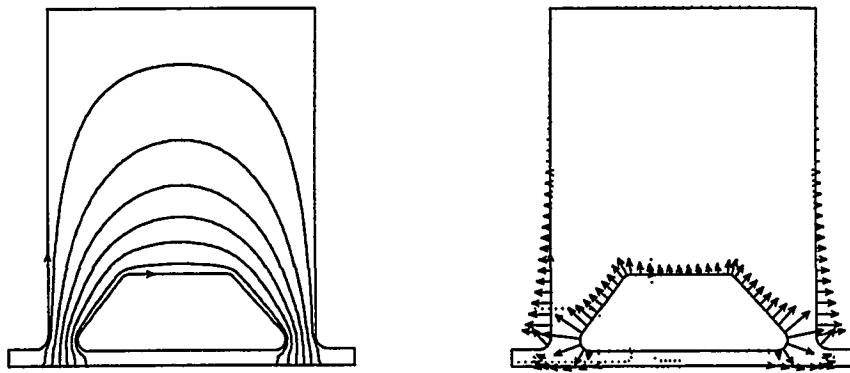


Section K

Figure 9.4 (continued)

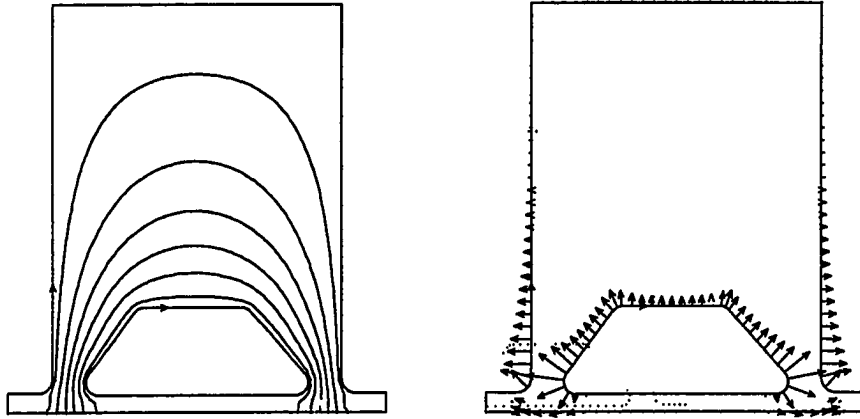


Section L

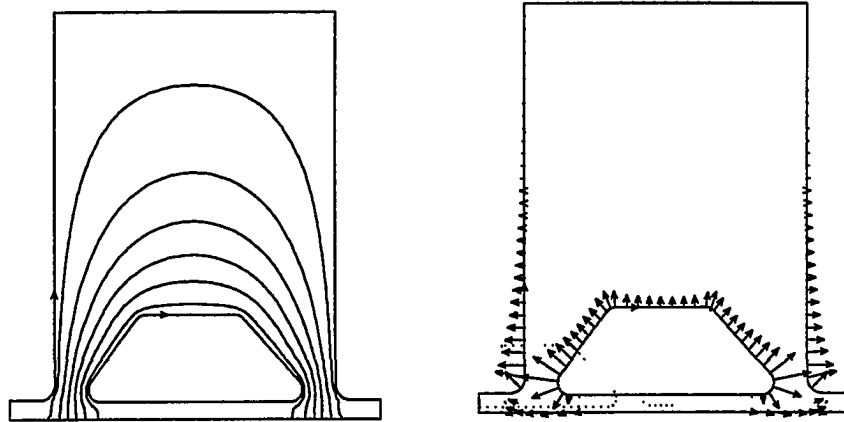


Section M

Figure 9.4 (continued)



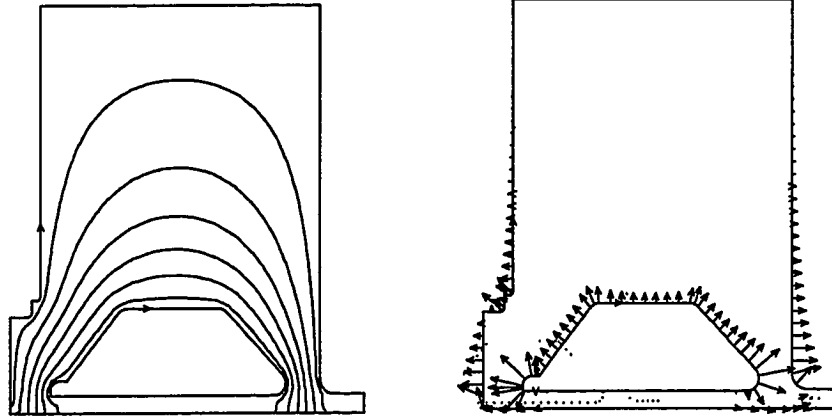
Section N



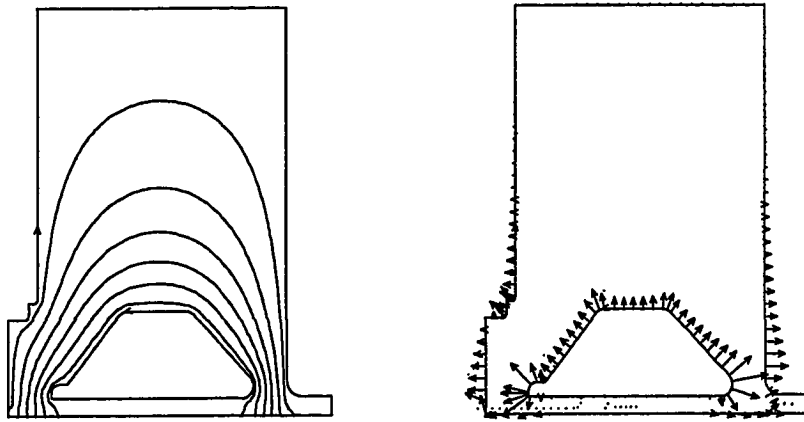
Section P

Figure 9.4 (continued)



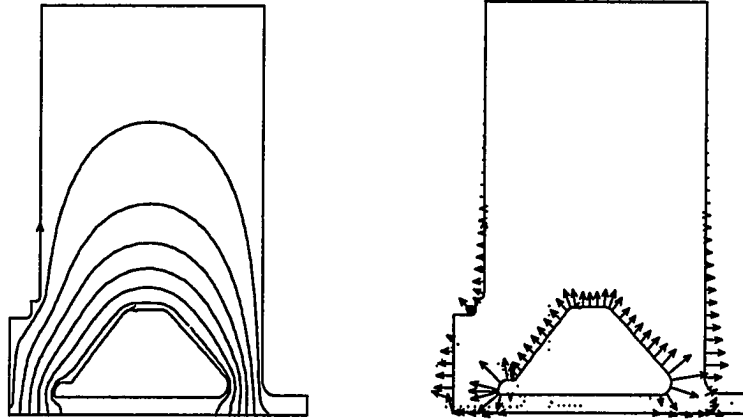


Section Q

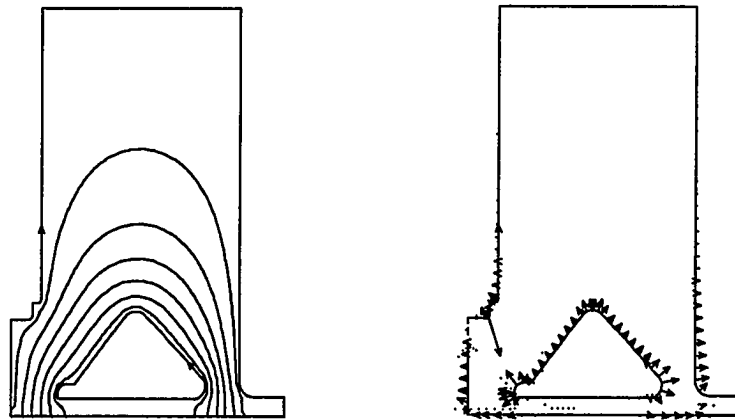


Section R

Figure 9.4 (continued)

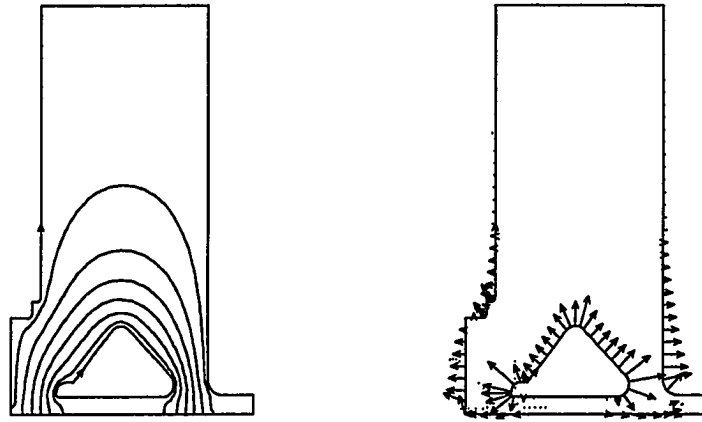


Section S

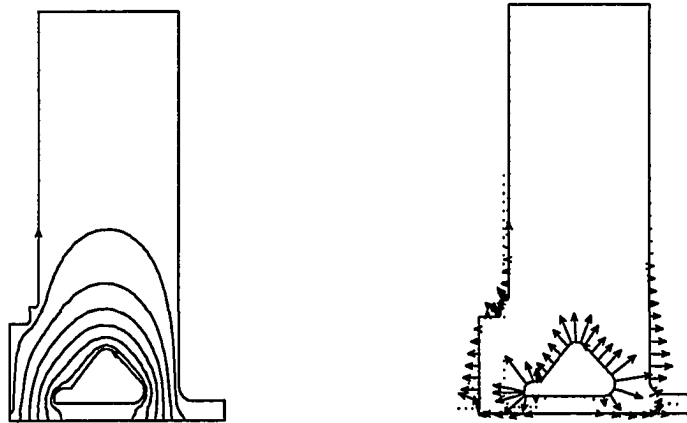


Section T

Figure 9.4 (continued)

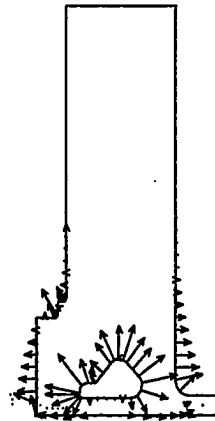
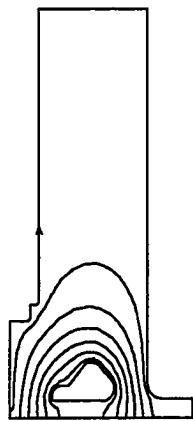


Section U

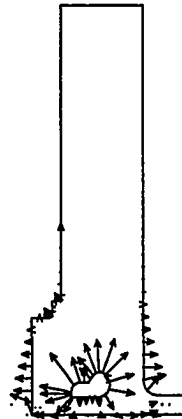
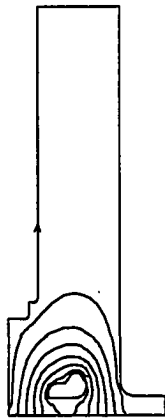


Section V

Figure 9.4 (continued)

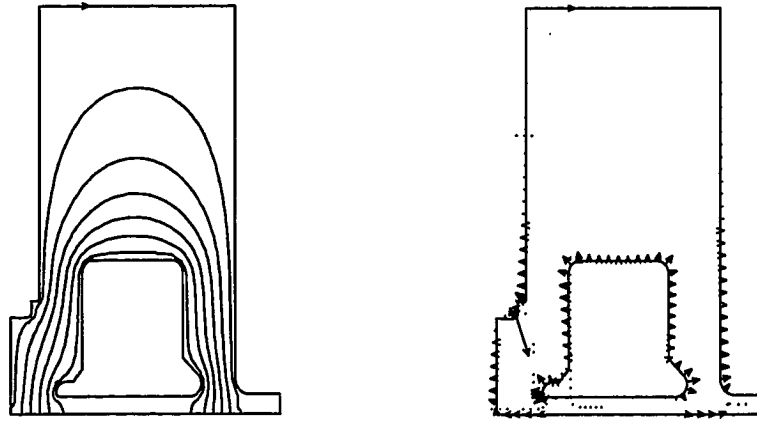


Section W



Section X

Figure 9.4 (continued)



Section TC

Figure 9.4 (continued)

The transverse characteristic impedance ( $Z_t$ ) for each cross-section is determined from the electrostatic stored energy determined by COSMOS at the applied potential. With 1 Volt applied, the formula relating the characteristic impedance to the electrostatic energy ( $U_e$ ) is

$$Z_t = \frac{1}{2cU_e},$$

where "c" is the speed of light in vacuum.

The coordinate that defines the cross-section location is defined along the guided wave axis of the dee starting at the cyclotron center. The distance from one cross-section to the next is determined by measuring the distance from one cross-section to the next along each dee inside and outside edge and taking the average. This method of accruing the distance along the guided wave axis is used because the energy is approximately evenly split between the two sides of the dee and is concentrated toward the edges of the dees where the dee comes closest to the liner which is the region of greater relative capacity and, equivalently, lowest relative  $Z_o$ . This can be seen by the electric field plots that are nearly always more intense over large areas at the dee-liner gaps than at other locations. Equivalently, this effect can be calculated by adding up the induced charge on these surfaces and noting that it is approximately evenly split across the dee and concentrated toward the edges. Table 9.2 tabulates the resultant transmission lines that describe the dee. The first and last transmission lines in the table are determined by using the value obtained from the first and last cross-sections and extending a transmission line from the cross-section location to the location of the dee tip and dee tail

respectively. The transverse characteristic impedance and the width of each conductor are calculated from the electrical parameters of the end cross-sections (figure 9.4) with the formulas derived in chapter 8 which are repeated here for reference.

$$Z_t = Z_{t1} \sqrt{\frac{1(\tau^2 - 1)}{2 \ln(\tau)}}, \quad w_e = \frac{w_{e2} - w_{e1}}{\ln\left(\frac{w_{e2}}{w_{e1}}\right)}, \quad \tau = \frac{Z_{t2}}{Z_{t1}}$$

Table 9.2 The K1200 Dee Transmission Line Chart

TLine	Section 1	Section 2	Z <sub>t</sub> (Ohms)	W <sub>de</sub> (cm)	W <sub>le</sub> (cm)	Length (cm)
T1	A	A	47.20	23.22	31.90	5.61
T2	A	B	46.48	24.19	33.83	10.22
T3	B	C	45.61	28.65	37.08	10.77
T4	C	D	47.23	35.29	45.34	10.77
T5	D	E	49.98	38.81	56.23	11.12
T6	E	F	49.93	39.66	64.15	12.83
T7	F	G	49.54	41.45	66.19	9.58
T8	G	H	49.80	44.52	65.05	9.33
T9	H	J	49.08	46.48	67.36	9.44
T10	J	K	54.77	39.80	58.52	11.11
T11	K	L	61.02	33.59	50.66	10.98
T12	L	M	61.25	33.41	51.08	10.91
T13	M	N	61.82	32.74	50.23	10.49
T14	N	P	62.48	32.22	49.31	9.18
T15	P	Q	63.31	32.84	50.21	12.78
T16	Q	R	65.22	32.53	51.84	9.03
T17	R	S	68.36	30.08	50.63	9.27
T18	S	T	72.17	27.40	46.97	8.26
T19	T	U	77.57	23.87	42.79	9.83
T20	U	V	84.87	19.52	39.06	9.72
T21	V	W	95.25	15.34	34.46	10.06
T22	W	X	110.04	11.12	29.52	9.89
T23	X	X	118.54	9.14	27.53	3.64
T24	See Figure 9.7		28.68	43.02	54.33	6.99
T25	See Figure 9.7		59.82	12.47	64.84	14.61

In addition to the cross-sections describing the dee, some additional lumped elements are used to model the dee tips, dee tail, and provide first order models for the "Dee Fine Tuning Capacitor" (DFT), and the "Input Coupler". The resonator simulation will show that the effects of these elements on the overall circuit response is small, particularly with respect to the coupler and dee-end capacitances, since they represent a small fraction of the overall equivalent shunt circuit element values at their respective locations in the resonator.

The center tip of the dee is a complex 3-dimensional geometry. A exact analysis would be a complex and time consuming process. A simple "back of the envelope" analysis will be performed to obtain a first order estimate of the capacitance to be used in the resonator simulation. The resonator sensitivity to this component will be evaluated at the highest operating frequency where it is most sensitive to this component. If the component is shown to have a significant effect on the overall resonator response, and the simulation shows a significant discrepancy to the measurements, then a more rigorous value determination may be justified. Figure 9.5 displays a simplified geometry that will be used to ascertain the lumped capacitive value for this component. The geometry is approximately cylindrical. Common parallel-plate and cylindrical capacitance formulas are applied to determine the first order estimate. The parallel plate formula

$$C = \frac{\epsilon A}{d}$$

with "A" representing the cross-sectional area and "d" the plate spacing, and the capacitance between coaxial cylinders formula



$$C = \frac{2\pi\epsilon L}{\ln\left(\frac{b}{a}\right)}$$

with "a" representing the inner cylinder radius and "b" the outer cylinder radius are applied. The formulas are augmented by the ratio of the angle that the cylindrical geometry spans, as shown in figure 9.5, to 360 degrees. Using these formulas, the capacitance is found to be

$$CDT = 2\pi\epsilon \left[ \frac{\frac{32}{360} \times 1.9}{\ln\left(\frac{2.5}{1.8}\right)} + \frac{\frac{29}{360} \times 3.1}{\ln\left(\frac{8.7}{1.8}\right)} + \frac{\frac{18}{360} \times 2.5}{\ln\left(\frac{10.4}{6.6}\right)} + \frac{\frac{9}{360} \times 2.5}{\ln\left(\frac{12}{6.6}\right)} \right] + \epsilon\pi \left[ \frac{(8.7^2 - 2.5^2) \frac{32}{360}}{3.1} \right] = 1.26 \text{ pF}$$

This value is shown to represent a very small percentage of the equivalent shunt capacitance at this point for the entire resonator so that an more accurate determination should not be needed.

The DFT spans cross-sections F through H. Its effects are determined based on a analysis of cross-section G and is represented by a model consisting of a series combination of a lumped capacitor, a lumped resistor (strap), and two transmission lines to circuit common from the location of cross-section G to circuit common as partially shown in figure 9.2 . The value of the capacitor is determined by placing 1 volt on the plate and 0 Volts on the dee and liner as shown in figure 9.6 The induced charge on the dee with the boundary conditions described is a direct measure of the capacitance between the dee and the plate per unit meter. The value from the electrostatic analysis performed with COSMOS results in 42.18 pF/m.

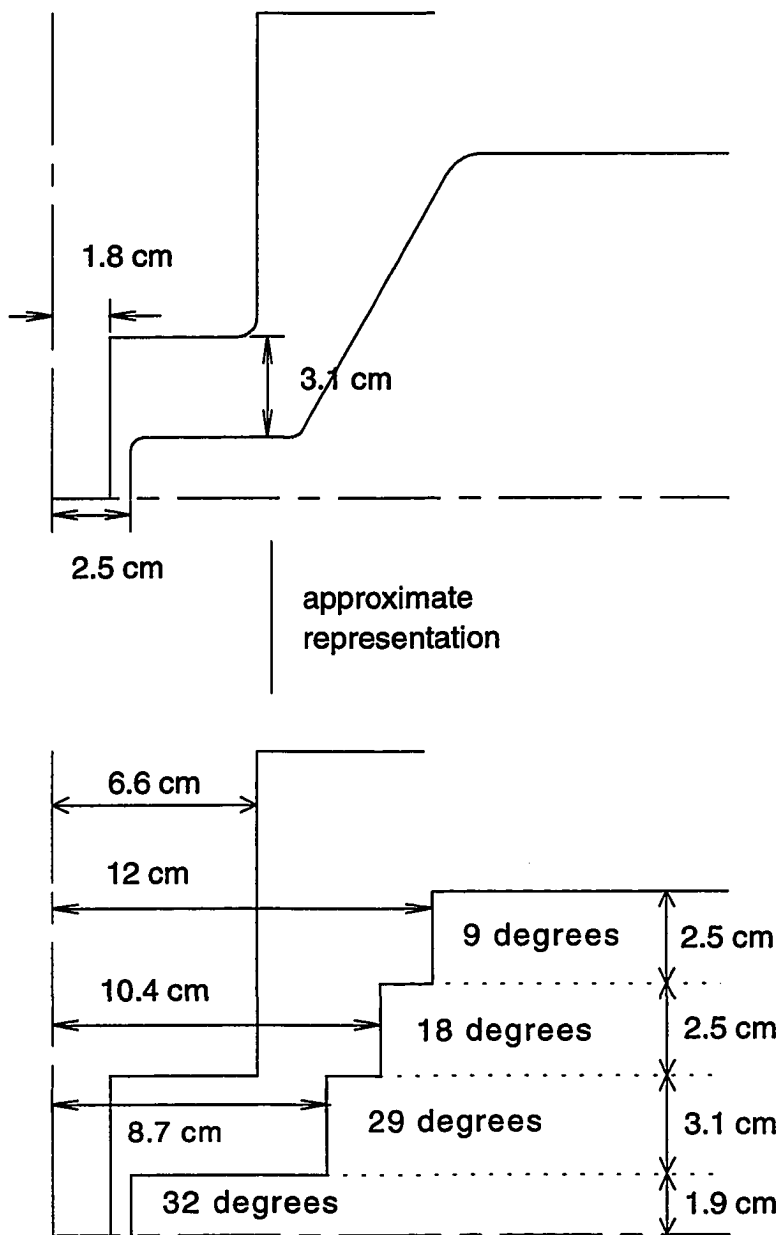


Figure 9.5 The K1200 dee tip geometry (not to scale).

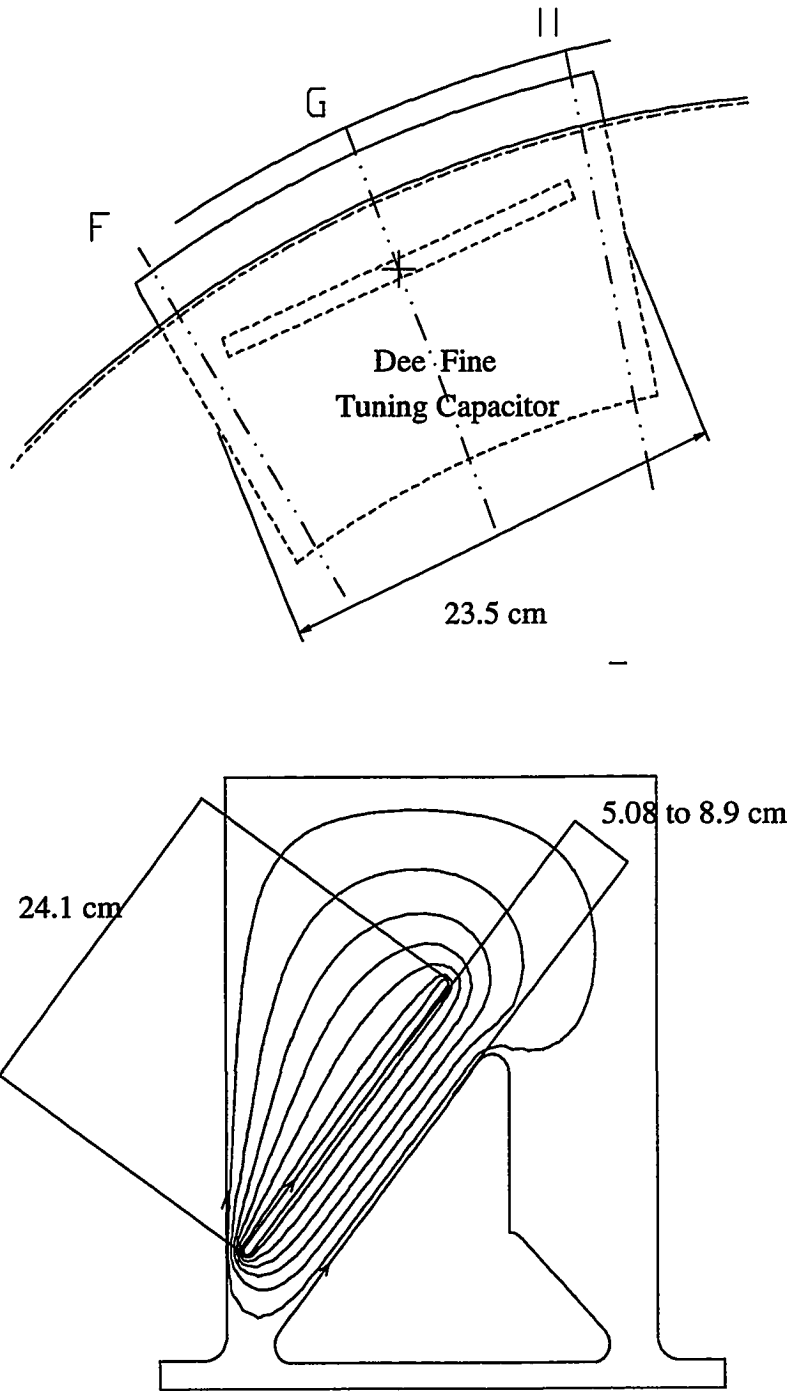


Figure 9.6 The K1200 dee fine tuner (DFT).

The calculated value assuming a parallel plate geometry and ignoring edge effects is

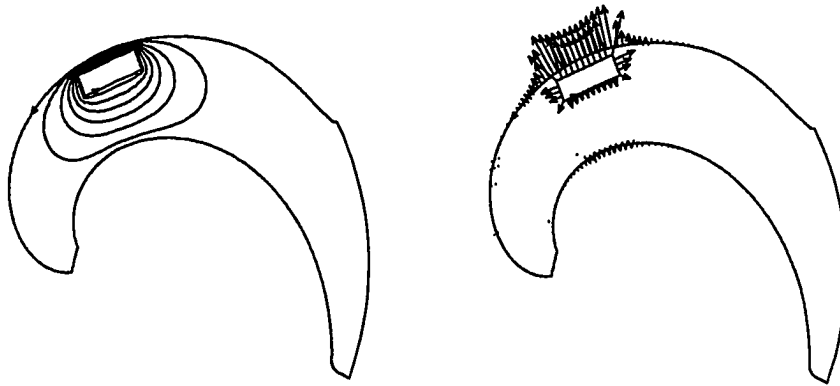
$$C = \frac{8.854 \times 0.241}{0.0508} = 42.0 \frac{\text{pF}}{\text{m}}.$$

The parallel plate approximation only results in a -0.43% error from the value calculated by COSMOS. Since the error is low, and the net effect on the overall structure due to this error is shown to be low in chapter ten, a parallel plate approximation is used to predict the capacitance value for any position of the tuning plate. The nominal operating position results in a gap of 7.72 cm from the dee-to-plate corresponding to a capacitance of 27.6 pF/m. With the plate being 0.235 meters long, the total value, ignoring end effects, is  $0.235 \times 27.6 = 6.49$  pF.

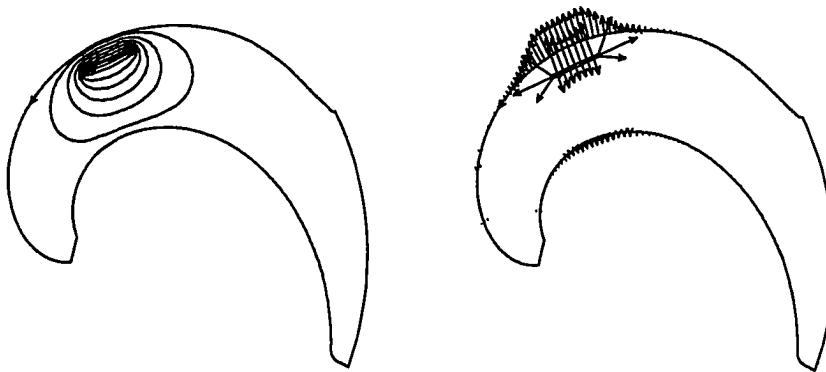
The electrical parameters of the transmission lines that tie the DFT plate to circuit common are based on finite element analysis as shown in figure 9.7. The plate resistance is conservatively based on the losses that would be incurred by a uniform current density. Since 1/2 of the current flows around the plate in either direction, the net resistance is

$$R_{DFT} = \frac{1}{2}R_s \left( \frac{L}{w} \right) \cong 0.49R_s$$

with  $R_s$  being the rf surface resistance described in chapter 3, and "L" being the length of the plate and "w" its width. A strap of length "L/2" and width "w" will represent the plate resistance. The resultant model for the DFT in its median position is then a series combination of a capacitor (6.49 pF), a strap, and two transmission lines (T24 and T25, see table 9.2 ) from the dee cross-section "G" to circuit common.



T24



T25

Figure 9.7 The K1200 dee fine tuner transmission lines.

The power input coupling is made about cross-section T. The effects are modeled as a lumped capacitance (CCC) to circuit common, and an input coupling capacitance (CC) to be determined from the resonator simulation for the input coupling capacitance needed to provide a match to the 50 Ohm source impedance of the feedline. The lumped capacitance to circuit common is determined based on the difference between the analysis of cross-section T without the coupling electrode and with it (SecTC, Table 9.1). Although the electrode is a cylindrical protrusion from the dee, a conservative (over-estimate) "back-of-the-envelope" estimate is made by extending the effects determined at the central location to span a distance of 1/2 radius on both sides of the cross-section. Cross-section T yields a value of 44.9 pF/m without the electrode and 68.8 pF/m with it. Since the electrode has a 9.43 cm diameter, the approximate value of CCC yields

$$CCC = 0.5(68.8 - 44.9) \times 0.0943 \cong 1.13 \text{ pF.}$$

The dee tail capacitance (CT) is easily estimated. It is based on a parallel plate approximation. The plate geometry is square with 3.4 cm sides, and the spacing between plates is 3.175 cm. This results in an approximate value for CT to be

$$CT = \frac{8.854 \times (0.034)^2}{0.03175} = 0.322 \cong 0.3 \text{ pF.}$$

### 9.4.2 The Tuning Stem Elements

The tuning stem is shown in figure 9.8. Referring to the figure, sections T26 - T30 are in a region known as the "Liner Valley" and the cross-sections of these lines are shown figure 9.9. T31 - T44 are cylindrical so that standard coaxial formulas are applied to determine the transverse characteristic impedance.

T38 - T40 contain a dielectric cylinder made of alumina with a relative dielectric constant of 9.8. This dielectric cylinder serves as a "Vacuum Window" separating the vacuum and air sections of the resonator. The cylinder has an inner radius of 19.05 cm and an outer radius of 20.0 cm. These transmission lines are modeled using the formulation derived in section 6.6.2. The resulting dielectric constants of the lines are 1.06, 1.065, and 1.08 for T38, T39, and T40 respectively.

Each SEC that models the non-uniform lines in the structure contains two transmission lines and a shunt capacitor arranged in a T-circuit topology as described in section 8.2.2. The transmission lines that model tapers as a part of each SEC labeled as TXX\_1 and TXX\_2 are given in table 9.4. The shunt capacitors for these lines are calculated with the coaxial step formula described in section 7.3.1 and are listed in table 9.5. Additional shunt capacitors, that are also determined by the coaxial step formula, are added at locations between T31 and T30, T37 and T38, T41 and T42, T43 and T44, and finally T45 and T46. Table 9.3 contains the cross-section data, table 9.4 contains the resultant transmission lines, and table 9.5 contains the lumped capacitor data for the dee stem.

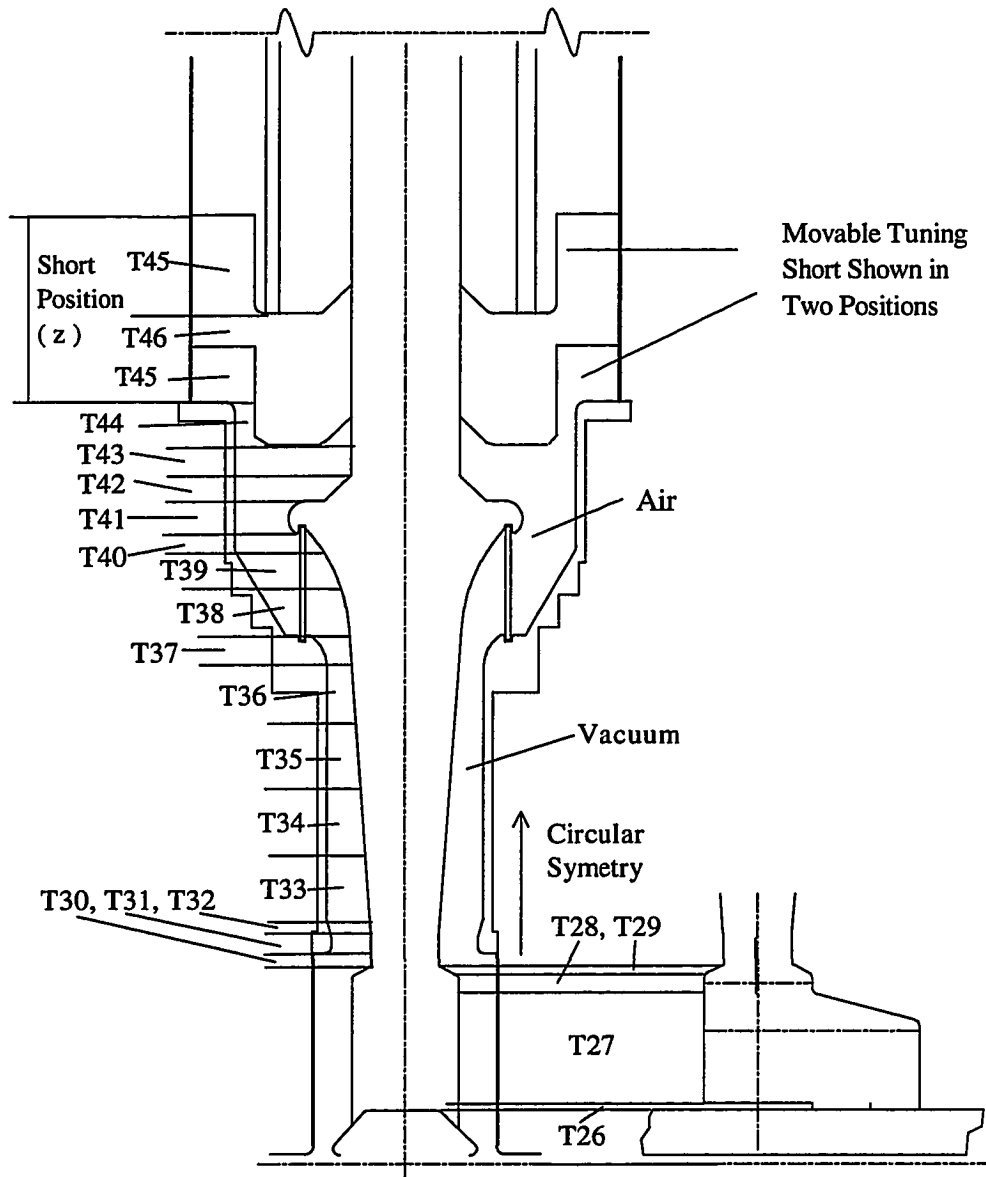
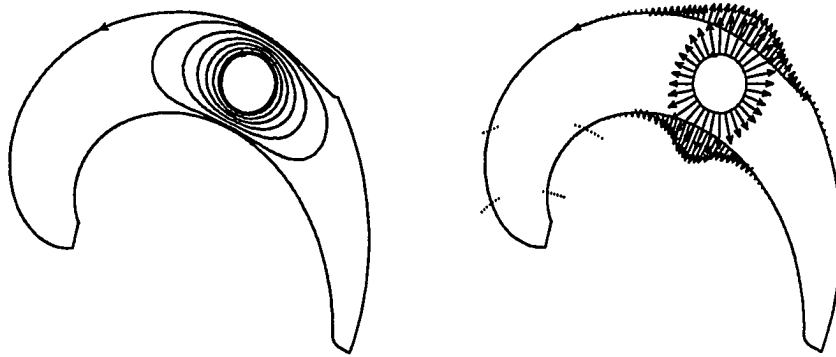
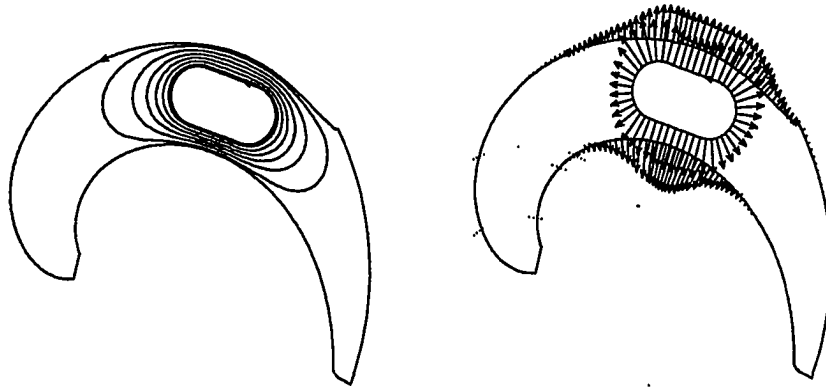


Figure 9.8 The K1200 dee stem.



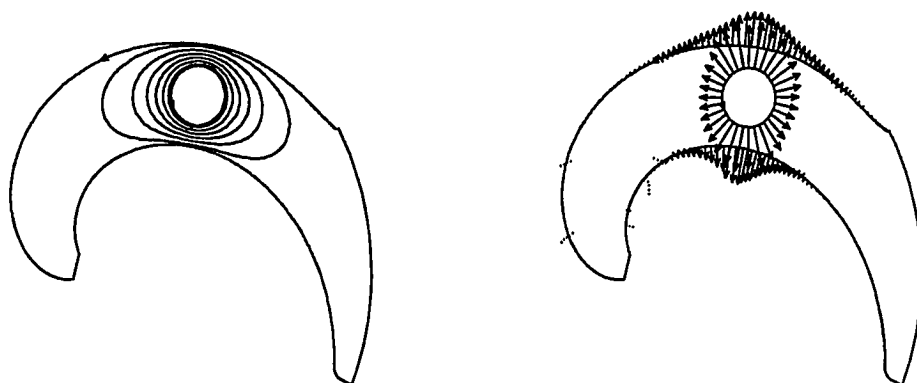


T26CS

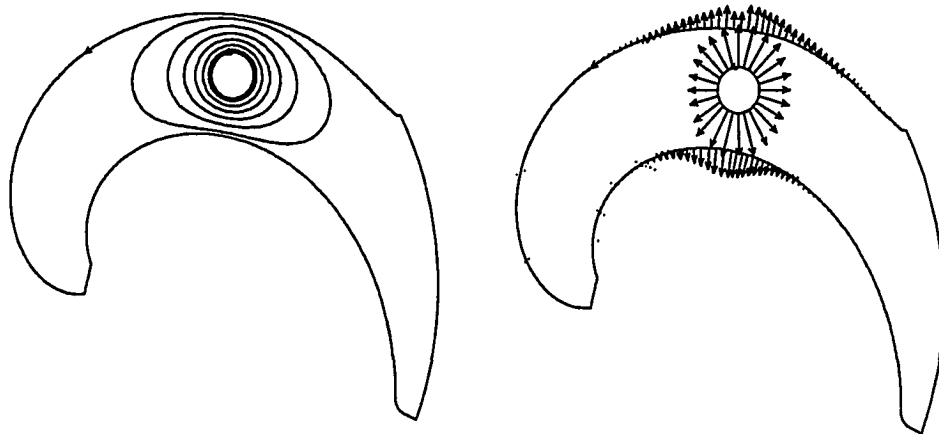


T27CS

Figure 9.9 The K1200 stem cross-sections.



T28CS



T30CS

Figure 9.9 (continued)

Table 9.3 The K1200 Dee Stem Cross-section Data

Cross-section	Inner Radius (cm)	Outer Radius (cm)	$Z_t$ (Ohms)	$w_d$ (cm)	$w_{de}$ (cm)	$w_l$ (cm)	$w_{le}$ (cm)
T26CS	See Figure 9.9		45.01	63.75	61.29	477.77	101.30
T27CS	See Figure 9.9		26.96	104.34	101.14	477.80	133.93
T28CS	See Figure 9.9		46.08	63.75	61.01	477.80	102.49
T30CS	See Figure 9.9		71.78	41.78	41.40	477.82	105.41
T31	6.502	13.970	45.85		40.86		87.78
T32	6.604	14.483	47.09		41.49		91.00
T33_1	6.731	14.923	47.74		42.29		93.76
T33_2	7.605	14.923	40.42		47.78		93.76
T34_1	7.605	14.923	40.42		47.78		93.76
T34_2	8.501	14.923	33.74		53.42		93.76
T35_1	8.501	14.923	33.74		53.42		93.76
T35_2	9.375	14.923	27.87		58.91		93.76
T36_1	9.375	14.923	27.87		58.91		93.76
T36_2	10.259	14.923	22.47		64.46		93.76
T37_1	10.259	14.923	22.47		64.46		93.76
T37_2	10.610	18.161	32.23		66.66		114.11
T38_1	10.610	22.885	44.76		66.66		143.79
T38_2	11.989	27.686	48.86		75.33		173.96
T39_1	11.989	27.686	48.86		75.33		173.96
T39_2	15.987	32.512	41.23		100.45		204.28
T40_1	15.987	32.512	41.23		100.45		204.28
T40_2	18.999	32.512	30.87		119.38		204.28
T41	21.590	32.512	24.55		135.65		204.28
T42_1	15.288	32.512	45.24		96.06		204.28
T42_2	10.320	32.512	68.80		64.84		204.28
T43	10.320	32.512	68.80		64.84		204.28
T44	28.702	32.512	7.47		180.34		204.28
T45CS	See Figure 9.10		21.50		180.34		257.78
T46CS	See Figure 9.10		82.76		64.83		257.78

Table 9.4 The K1200 Dee Stem Transmission Lines

Element Name	$Z_t$ (Ohms)	$w_{de}$ (cm)	$w_{le}$ (cm)	Length (cm)
T26	45.01	61.29	101.30	1.27
T27	28.51	101.14	133.93	21.48
T28	46.08	61.01	102.49	3.01
T29_1	58.45	50.57	103.94	1.40
T29_2	58.45	50.57	103.94	1.40
T30	71.78	41.40	105.41	2.65
T31	47.74	40.86	87.78	3.15
T32	47.09	41.49	91.00	3.48
T33_1	45.89	44.98	93.76	6.32
T33_2	42.23	44.98	93.76	6.32
T34_1	38.74	50.55	93.76	6.32
T34_2	35.39	50.55	93.76	6.32
T35_1	32.26	56.12	93.76	6.32
T35_2	29.32	56.12	93.76	6.32
T36_1	26.51	61.64	93.76	6.32
T36_2	23.80	61.64	93.76	6.32
T37_1	24.87	65.55	103.60	2.59
T37_2	29.76	65.55	103.60	2.59
T38_1	45.78	70.91	158.40	4.26
T38_2	47.83	70.91	158.40	4.26
T39_1	46.94	87.29	188.71	4.26
T39_2	43.12	87.29	188.71	4.26
T40_1	38.61	109.64	204.28	2.03
T40_2	33.43	109.64	204.28	2.03
T41	24.55	135.65	204.28	5.37
T42_1	51.02	79.43	204.28	0.5*LT42(z)
T42_2	62.82	79.43	204.28	0.5*LT42(z)
T43	68.80	64.84	204.28	LT43(z)
T44	7.47	180.34	204.28	LT44(z)
T45	21.42	180.34	257.78	LT45(z)
T46	82.76	64.83	257.78	LT46(z)

Table 9.5 The K1200 Coaxial Step Capacitors

Label	Location	Step Type	a (cm)	b (cm)	c (cm)	Value (pF)
CS1	T30-T31	outer	8.33	13.97	17.47	7.03E-13
CS2	T37-T38	outer	10.61	14.92	22.89	2.73E-12
CS3	T41-T42	inner	19.00	21.59	32.51	7.48E-13
CS4_1	T43-T44	inner	10.32	28.70	32.51	1.64E-11
CS4_2	T45-T46	inner	10.32	28.70	41.03	8.95E-12
CS5_1	T44-T45	outer	28.70	32.51	41.03	8.35E-12
CS5_2	T43-T46	outer	10.32	32.51	41.03	5.05E-13
CT29	Taper	inner	6.65	10.15	22.26	7.37E-13
CT33	Taper	inner	6.67	7.60	14.92	1.40E-13
CT34	Taper	inner	7.60	8.50	14.92	1.58E-13
CT35	Taper	inner	8.50	9.38	14.92	1.87E-13
CT36	Taper	inner	9.38	10.26	14.92	2.45E-13
CT37_1	Taper	inner	10.26	10.61	16.67	4.20E-14
CT37_2	Taper	outer	10.43	14.92	18.16	1.03E-12
CT38_1	Taper	inner	10.61	11.99	25.29	1.76E-13
CT38_2	Taper	outer	11.30	22.89	27.69	5.76E-13
CT39_1	Taper	inner	11.99	15.99	30.10	9.31E-13
CT39_2	Taper	outer	13.99	27.69	32.51	5.64E-13
CT40	Taper	inner	15.99	19.00	32.51	6.97E-13
CT42	Taper	inner	10.32	15.29	32.51	1.06E-12

Transmission line T27, referred to as the "Dog Leg" and the surrounding geometry needs some further explanation. Transmission line T27 is affectionately referred to as the "Dog Leg" because its shape roughly resembles that of the rear leg of a dog. This jog in the stem was not originally in the design, however calculations and measurements made on a full scale low power model indicated the voltage distribution on the dee was not optimal. The voltage on the center dee tip was higher than the voltage at the tail. Since considerable difficulty was being experienced in finding a solution for extracting the beam from the cyclotron theoretically,

and higher voltages at the tail end of the dee aids the extraction process by increasing the turn-to-turn beam separation at that location, it was decided to shift the stem to achieve a more favorable dee voltage distribution.

The "Dog Leg" transmission line, T27, has a characteristic impedance that accrues the net capacitance determined by finite element analysis (see figure 9.9). The top of the section where it tapers to the cylindrical stem connection is handled by taking the average of the sum of the extension of the cylindrical line through the tapered region and the extension of the untapered section through the taper. The net capacitance of the tapered section of the dog leg using this approximation is then

$$C = \frac{1}{2} \frac{L}{c} \left( \frac{1}{Z_{o1}} + \frac{1}{Z_{o2}} \right) = \frac{1}{2} \frac{5.62}{3 \times 10^{10}} \left( \frac{1}{26.96} + \frac{1}{46.08} \right) = 5.5 \text{ pF}$$

The capacitance of the untapered section of the dog leg is

$$C_2 = \frac{15.86}{3 \times 10^{10} \times 26.96} = 19.61 \text{ pF.}$$

The net capacitance of this section of the dog leg is  $C_1 + C_2 = 25.11 \text{ pF}$ . A Section of line that accrues this value of capacitance over the length of T27 has a characteristic impedance of

$$Z = \frac{L}{cC} = \frac{21.48}{3 \times 10^{10} \times 25.11 \times 10^{-12}} = 28.51 \text{ Ohms}$$

Table 9.4 lists the values obtained for transmission line T27.

The rest of the stem and capacitances are listed in tables 9.3, 9.4, and 9.5. The main tuning stem outer conductor is a dodecahedron (12

sided) with each side being a removable panel. Figure 9.10 displays the results of finite element analysis for a 1/6<sup>th</sup> section of each of the effected transmission lines. Since the analysis predicts very slight differences from assuming a standard coaxial structure, for analysis purposes the outer conductor diameter of these lines is simply set equal to a diameter that yields the correct characteristic impedance. Finally, the functions for the lengths of the lines T42, T43, T44, T45, and T46 as a function of short position "z" are

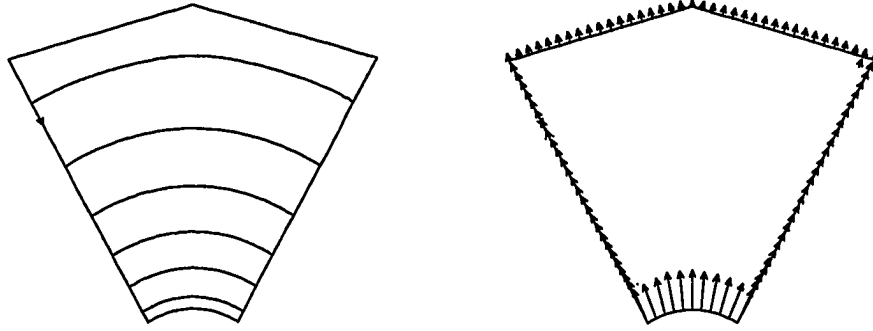
$$LT42(z) = \begin{cases} z & \text{if } z \leq 5.23 \\ 5.23 & \text{if } z \geq 5.23 \end{cases} \text{ cm}$$

$$LT43(z) = \begin{cases} 0 & \text{if } z \leq 5.23 \\ z - 5.23 & \text{if } 5.23 < z < 19.68 \\ 14.45 & \text{if } z \geq 19.68 \end{cases} \text{ cm}$$

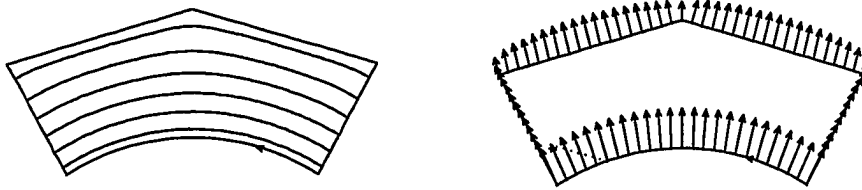
$$LT44(z) = \begin{cases} 19.68 - z & \text{if } z \leq 19.56 \\ 0 & \text{if } z \geq 19.56 \end{cases} \text{ cm}$$

$$LT45(z) = \begin{cases} z & \text{if } z \leq 19.68 \\ 19.68 & \text{if } z \geq 19.68 \end{cases} \text{ cm}$$

$$LT46(z) = \begin{cases} 0 & \text{if } z \leq 19.56 \\ z - 19.56 & \text{if } z \geq 19.56 \end{cases} \text{ cm}$$



T45CS



T44CS

Figure 9.10 The K1200 tunable stem sections.



### 9.4.2.1 Joint Resistors

The joints on the dees consist of the dee tips to dee shell and the upper to lower dee shell finger connections. The dee joints carry no significant current so they will not be included in the model. The dee stem contains many significant current carrying joints, so that the effects of these joints must be included. Chapter three determined a value for bolted joint resistance of 0.0019 Ohm-cm and of 0.015 Ohm-cm for the NSCL finger contact strips. Table 9.6 lists the joint resistors to be included in the model. The joints have the same equivalent widths as the lines they connect.

Table 9.6 The K1200 Dee Stem Joint Resistances

Label	Location	Conductor	$w_e$ (cm)	Value (Ohms)
RJ1	T27-T28	inner	101.14	3.95E-05
RJ2	T28-T29	inner	63.75	6.27E-05
RJ3	T30-T31	outer	87.78	4.56E-05
RJ4	T37_2-T38	outer	65.55	6.1E-05
RJ5	T41-T42_2	inner	96.06	4.16E-05
RJ6	T44-T46	inner	257.78	1.55E-05
RJ7	T46-T45	inner	64.83	6.17E-05
RJ8	T46-T45	inner	64.83	2.31E-04
RJ9	T45- Com	outer	257.78	1.55E-05
RJ10	T45-Com	outer	257.78	5.82E-05

### 9.4.2.2 Annuli

The sliding shorting plane as well as the surfaces that caused the coaxial step capacitances listed in table 9.5 also lead to losses that need to be accounted for. These losses are accounted for with resistive annuli the

dimensions for which are listed in Table 9.7. The annulus resistance for a constant current is calculated from the formula

$$R = \frac{R_s}{2\pi} \ln\left(\frac{b}{a}\right),$$

where  $R_s$  represents the rf surface resistance described in chapter three and  $b/a$  representing the outer/inner annulus radii.

Table 9.7 The K1200 Annuli

<b>Label</b>	<b>Location</b>	<b>Inner Radius (cm)</b>	<b>Outer Radius (cm)</b>
<b>ANCS1</b>	T30-T31	13.97	17.47
<b>ANCS2</b>	T37-T38	14.92	22.89
<b>ANCS3</b>	T41-T42	19.00	21.59
<b>ANCS4</b>	T45-T46	10.32	28.70
<b>ANCS5</b>	T43-T46	32.41	41.03
<b>ANT44</b>	Short	28.70	41.03

## **CHAPTER TEN**

### **The K1200 Resonator Simulation and Measurements**

#### **10.1 Introduction**

This chapter begins by describing some perturbation based measurement techniques. The chapter then goes on to its principle purpose which is to describe the techniques that were used to make the actual measurements on the K1200 resonators and to compare these data to the results obtained from analyzing the model developed in the previous chapter. The measured data associated with the resonant frequency are found to agree well with the simulations while the resonator losses are found to have the same overall functionality yet require approximately 50% more power than the simulations predict. This inconsistency has been observed before at the NSCL and is likely due to the uncertainty in predicting the rf surface resistivity and the joint resistances.

The measurements and model simulations are performed at 10 frequencies that span the K1200 operating frequency range of 9.5 to 26.5 MHz. The results are presented in the form of the resonator tuning stem position and the equivalent shunt circuit elements (R, L, C) at the cyclotron center. The tuning stem position and the shunt resistance are measured. The tuning stem position versus frequency is an indirect measure of the reactive shunt circuit elements. The degree to which the measured tuning

stem position differs from the calculated value is a measure of the accuracy of the calculated reactive shunt circuit values, particularly at the high frequency end of the tuning range where the structure is dominated by nonstandard, non-uniform structures.

## **10.2 Measurements of Shunt Capacitance and Voltage Variations by Method of Resonator Perturbation.**

Perturbation techniques are commonly applied to determine parameters that are difficult (or impossible) to measure directly. The techniques are applied by varying known controllable parameters and monitoring some resultant change in the system being perturbed. A knowledge of the change observed in the monitored parameter(s) and known relationship(s) between the perturbed parameter and the monitored parameter(s) in terms of the parameter being sought is applied to obtain the unknown parameter value. The techniques presented here include 1) measuring the electric field or voltage variations by capacitive perturbation, and 2) measuring the resonator equivalent shunt capacitance by varying a known capacitance and adjusting the frequency to reestablish resonance.

### **10.2.1 Voltage Variations by Inserting a Known Capacitor.**

Electric field strength or voltage variations may be measured by moving a known capacitor or dielectric "bead" about a resonator and noting the change in resonant frequency at each position. It is reasonable to assume that regions of highest voltage or electric field strength will lead to greater perturbations in the resonant frequency since at these locations the

inserted element would have the largest effect on the stored electric energy. The capacitor or bead value must be chosen to cause a small fractional change in the stored electric energy so that the fundamental resonator mode, or circuit response, is unchanged. The technique described here was applied in 1988 to the K1200 resonator on a full scale model to determine the dee voltage variations [10.1]. The variations observed confirmed the need to move the stem location to modify the dee voltage variations along the radius of the cyclotron to better match the accelerator needs. Additionally, these measurements have been used to confirm the voltage variations predicted by the resonator model.

If at some point in a resonator an equivalent shunt circuit representation  $R_o$ ,  $L_o$ , and  $C_o$  is defined, the resonant frequency is found from

$$\omega_o = \frac{1}{\sqrt{L_o C_o}}.$$

For small perturbations, the change in resonant frequency due to the addition of a small capacitance may be described by a first order truncated Taylor's series expansion.

$$\omega = \omega_o - \frac{\omega_o}{2C_o}(C - C_o)$$

If the definitions

$$\omega \equiv \omega_o - \Delta\omega \quad \text{and} \quad C \equiv C_o + \Delta C,$$

are made and inserted into the previous result then

$$\Delta\omega = \frac{\omega_o}{2} \left( \frac{\Delta C}{C_o} \right).$$

If the variation of the voltage between two points is sought where the shunt circuit is defined by  $R_1, L_1, C_1$  and  $R_2, L_2, C_2$  then from

$$U_e = \frac{1}{2} C_1 V_1^2 = \frac{1}{2} C_2 V_2^2 \rightarrow \frac{C_2}{C_1} = \left( \frac{V_1}{V_2} \right)^2$$

and

$$\Delta\omega_1 = \frac{\omega_1}{2} \left( \frac{\Delta C}{C_1} \right) \quad \text{and} \quad \Delta\omega_2 = \frac{\omega_2}{2} \left( \frac{\Delta C}{C_2} \right).$$

it follows by taking the ratio of the two expressions for frequency and substituting the square of the voltages for the ratio of shunt capacitances that

$$\frac{\Delta f_1}{\Delta f_2} = \left( \frac{V_1}{V_2} \right)^2 \quad \text{or} \quad \left( \frac{|\mathbf{E}_1|}{|\mathbf{E}_2|} \right)^2 \quad (\text{for beads}).$$

The above result is useful since it does not require an exact knowledge of the shunt capacitance value, or the inserted capacitance value, or the exact dielectric bead effect. All that is required to be known is that the inserted component causes a small similar effect in the overall electric stored energy at the two locations. By measuring the frequency shift at each location, the above expression yields the relative ratio of the fields between the two locations. If an absolute calibration is known at some

point, then this knowledge in combination with the perturbation measurements may be used to obtain the absolute calibrations at all points.

### 10.2.2 Measurement of the Shunt Capacitance

The equivalent shunt capacitance may be measured by inserting a known capacitance and measuring the needed change in frequency to reestablish resonance. Using the following definitions

$$C = C_o + \Delta C \text{ with } \Delta C \geq 0 \rightarrow f = f_o - \Delta f \text{ with } \Delta f > 0.$$

Two frequency measurements are made corresponding to

$$\omega_{o1} = \frac{1}{\sqrt{L_o C_o}} \text{ and } \omega_{o2} = \frac{1}{\sqrt{L(C_o + \Delta C)}}.$$

Taking the ratio of the measurements yields

$$\frac{f_{o1}}{f_{o2}} = \sqrt{1 + \frac{\Delta C}{C_o}}.$$

The above relationship may be rearranged to determine the unknown quantity based on the known quantities.

$$C_o = \frac{\Delta C}{\left(\frac{f_{o1}}{f_{o2}}\right)^2 - 1}$$

### **10.3 The Measurement Techniques and Trials**

The K1200 Cyclotron is scheduled for 24 hours per day, 7 days per week operation. Maintenance periods are heavily scheduled on a priority basis. The first trial of measurements were made on the system on November 6 and 8, 1995. Exhaustive tuning and operating parameters for the rf system were taken during this period. During the first trial, x-ray calibrations to confirm the displayed dee voltages were only obtainable for one frequency because of high residual background radiation as a result of the previous physics experiment, and equipment malfunctions which were not resolved until late in the scheduled period. In addition, the rf power measurements were made at low power levels and with low transmitter plate efficiency which led to uncertainty in the ensuing analysis. Based on the results of the first trial, the measurement techniques were improved and a second trial was performed on January 25 and January 27, 1996. The improved techniques and conditions included 1) measuring x-rays at all the frequencies to calibrate the voltage monitors, 2) operating at a higher and constant voltage of 120 kV peak for all measurements at all frequencies, 3) obtaining an exact calibrating of the equipment used to make the calorimetric measurements against the anode power supply output power, and 4) tuning the rf transmitters in a special high efficiency mode. The improved techniques in combination with the absolute voltage calibrations obtained with the x-rays significantly improved the accuracy of the measurements.



### 10.3.1 The X-ray Dee Voltage Measurement Technique

Since the vacuum chamber containing the dees is inaccessible, and the operating voltages are high, a special technique is applied to calibrate the dee voltage readings [10.2]. For good x-ray spectrums, the NSCL operations group can determine the dee voltage to within  $\pm 1$  kV using this technique. Since the dee voltage calibrations were performed at 120 kV, the accuracy will be taken to have an accuracy of  $\pm 1$  %. On the upper cap of the cyclotron, holes exist in the same locations as the mirror image holes on the lower cyclotron cap that are used to couple in the resonator drive power. The upper holes have been fitted with glass windows and a fixture to hold a portable germanium detector ( EG&G ORTEC model number Gem 33190-Plus). The germanium detector includes an integrated charge sensitive amplifier. The detector appears to the integrated charge sensitive amplifier as a capacitively coupled reverse biased diode. It is biased to 3 kVDC with a 0-5kVDC Ortec model 459 power supply. The amount of charge released for a given energy x-ray is linearly proportional to the x-ray energy in the operating domain that we are interested in. The detector is maintained at liquid nitrogen temperature with an integrated vessel to reduce the noise. The output of the charge sensitive amplifier is coupled to an Ortec model 572 shaping amplifier. The shaping amplifier takes the potential difference of the abrupt step produced for a given x-ray and creates a short duration pulse whose peak height is precisely proportional to the charge. The output of the shaping amplifier feeds a Norland Inotech 5300 Multichannel Analyzer (MCA). The MCA is calibrated by applying to the germanium detector two sources of different

energy to fit a straight line in a manner that makes each channel have a 1/2 keV granularity with the first channel equal to 0 keV.

The basic idea is that the germanium detector is used to detect bremsstrahlung x-rays produced in the vacuum chamber by the electrons accelerated by the high dee voltages. The endpoint of the energy spectrum corresponds to the peak dee voltage. The multichannel analyzer is calibrated to display increasing keV along the x-axis, while the y-axis is the number of counts that have accumulated for each channel since the device was last cleared. Provided the detector is arranged to dominantly detect x-rays emanating from the cyclotron dee being monitored, and the residual radiation is low enough, the highest energy x-ray detected not attributed to background corresponds to the peak dee voltage. Figure 10.1 displays a typical x-ray spectrum obtained with the constant background subtracted out.

### **10.3.2 The Resonator Amplitude Measurement Technique**

Each quarter wave section of the cyclotron resonators is tuned by a sliding short. Each sliding short contains 2 small machined loops which are used to monitor the rf field levels in the resonator. The loops yield the greatest response in the operating band at 27 MHz where they are designed to generate approximately 10 Vrms at 200 kV peak dee voltage. This topology results in a total of 12 loops on the cyclotron, two per each of six quarter wave sections. Signals from these loops are transported approximately 225 ft to the "K1200 RF Control Balcony" through high quality, phase matched, semi-rigid coaxial 50 Ohm cables.

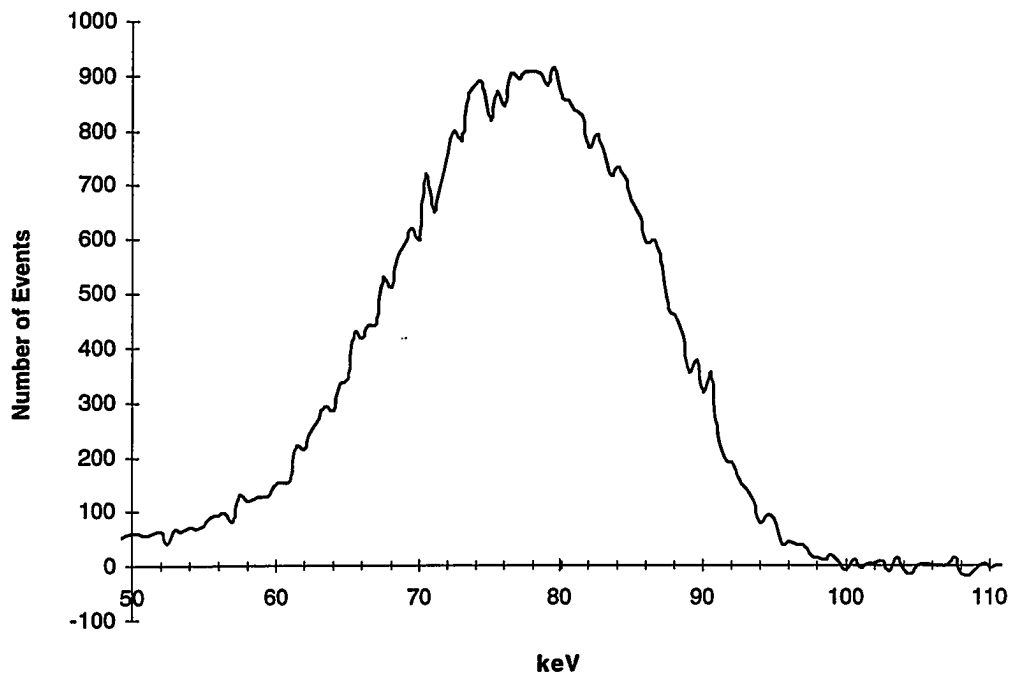


Figure 10.1 98 kV X-ray spectrum from the K1200 C dee at 26.5 MHz.

Most of the signals from the loops are passed through resistive 4-way signal splitters. The outputs from the splitters feed rf signals to many different types of electronics modules. The input impedance of these modules, although nominally 50 Ohms, are not perfect and vary in complex ways over the operating frequency range. One of the loops, labeled as DV4, for each resonator was terminated in a pure 50 Ohm resistor to remove any complex variations due to imperfect terminations. The measurements using the DV4 loop is used here as the definitive reference since its load impedance was carefully controlled.

RF amplitude measurements from the DV4 monitor were made at 10 rf frequencies spanning the operating range of the resonators of 9.5 to 26.5 MHz. The measurements of the loop voltages were made with a single voltmeter. The voltmeter used is a Hewlett-Packard (HP) Vector Voltmeter model 8405A voltmeter in combination with a HP 11576A 10:1 divider. This instrument, as configured, has an advertised accuracy of +/- 6% of full scale. The measurements were made on the 10 Volt full scale and 3 Volt full scale ranges as appropriate leading to a measurement accuracy of +/- 0.6 Volts and +/- 0.18 Volts respectively. The measurements were made with x-ray calibrations leading to an absolute ratio of DV4 voltage to the cyclotron voltage at the input coupler location.

### **10.3.3 The Resonator Power Measurement Technique**

The resonator loss measurements were made indirectly. The loss measurements were made at the same levels as the loop measurements described in the previous section. As mentioned previously, all of the

measurements were made at 120 kV peak voltage at the rf input coupler location as confirmed by x-ray measurements.

The rf amplifier final stage uses a 250 kW water cooled tetrode vacuum tube as its driving element. This tube is operated in class AB very close to the class C boundary and achieves between 60-to-80 % plate conversion efficiency when it is optimally biased. The plate conversion efficiency is a number that relates the dc input power to the tetrode plate to the resultant rf output power; the difference resulting in losses to the plate that is removed by the water cooling. In addition to the power consumed in the plate, the transmitter plate resonant tank and the 6 1/8 inch diameter, 50 Ohm, coaxial transmission line that feeds the cyclotron resonator combined consume about 0.5% of the available output power. The transmitter output also includes a minimum output load to help maintain stability during turn-on periods that consists of a series circuit containing a 12 pF capacitor in series with a 168 Ohm water cooled resistor. The minimum load is placed in parallel with the transmitter output which also places it in parallel with the 6 1/8 inch transmission line that feeds the cyclotron resonator.

The available transmitter rf output power can be determined by subtracting the measured power deposited in the cooling water from the measured power supplied to the plate ( $W_p$ ) by the plate bias power supply. This power must be further reduced by the 0.5 % previously mentioned and by the power lost in the minimum load. In order to reduce the overall uncertainty accumulated by all of the equipment associated with the calorimetric and power supply metering circuits, an absolute calibration of the calorimetric power to anode bias supply power was made. The calibration was made by adjusting the anode current under dc conditions

(all of the power is deposited in the plate cooling water under these conditions) and monitoring the temperature difference between the supply and return cooling water. A straight line relationship is expected similar to

$$W_A = 264 \cdot GPM \cdot \Delta T \text{ Watts,}$$

where GPM represents the Gallons-per-Minute of cooling water. The relationships actually measured combine the GPM and 264 into a single constant and include an offset because some of the tube filament power is also deposited in the anode water cooling circuit under conditions of no or low anode power dissipation. The equations arrived at for each resonator, denoted as A, B, and C, for GPMs of 30.9, 32.9, and 33.64 respectively are

$$W_{WA} = 8.36 \cdot \Delta T - 5.01 \text{ kW}$$

$$W_{WB} = 8.61 \cdot \Delta T - 5.34 \text{ kW}$$

$$W_{WC} = 9.25 \cdot \Delta T - 5.74 \text{ kW}$$

Determining the plate loss with the above equations, which were derived based on the anode power supply measurements, resolves the total measurement error to that of the uncertainty in the plate power supply output power alone. The uncertainty associated with the anode power supply power readings are bounded within +/- 3%. The available power is then calculated from

$$W_{Ax} = (W_{px} - W_{wx}) \text{ +/- 3 \%}$$

where the subscript "x" in the relationship is replaced by A, B, or C to reference the appropriate resonator being considered.

The above power is distributed as mentioned into resonator drive, minimum load drive, and other losses (0.5 %). The minimum load power is computed with the results of the following development. The total available power may be written as the sum of the power to the resonator and the power to the minimum load as

$$W_A = W_R + W_L$$

This expression may be rearranged into

$$W_R = \frac{W_A}{1 + \frac{W_R}{W_L}}$$

This expression may be cast into the following form

$$W_R = \frac{W_A}{1 + \frac{Z_o}{R} [1 + (\omega RC)^2]}$$

with R and C equal to the series minimum load elements and  $Z_o$  representing the 6 1/8 inch transmission line characteristic impedance.

Using the expressions developed, the net power available to the cyclotron resonators is

$$W_R = \frac{0.995[(W_{px} - W_{wx})]}{1 + \frac{Z_o}{R} [1 + (\omega RC)^2]} \quad +/ - 3\%$$

The equivalent shunt resistance, as described in section 5.3.2, is computed from the ratio of the dee voltage, which is known to  $\pm 1\%$ , squared to the power dissipated, which is known to  $\pm 3\%$ . This results in a maximum measurement error for the equivalent shunt resistance of  $\pm 5\%$ .

#### **10.4 The K1200 Measurements**

The important parameters associated with the cyclotron resonators include the tunable frequency range, accurate knowledge of the operating voltage, and the needed drive power. The measurements concentrated on accurately determining these parameters. The tuning range is determined by the resonant frequency versus tuning stem position. The needed drive power may be described by the equivalent shunt resistance at some agreed upon location in the resonator where the voltage is commonly known. The voltage which is specified to the operators for any particular beam is the peak dee voltage at the center of the cyclotron. Since this is an important cyclotron tuning parameter and is specified for each charged particle beam to be accelerated, the equivalent shunt circuit parameters will be specified at this point. Table 10.1 lists the calibrations for the DV4 rf monitor for all three stations. Table 10.2 list the measured shunt resistance values for all three stations at the cyclotron center, and figure 10.1 plots them. The tuning stem lengths that were measured are listed in table 10.3.



Table 10.1 The K1200 DV4 Monitor Calibration

Frequency (MHz)	Displayed Dee Voltage (kV Peak)	Dee Voltage at Center of Cyclotron (kV Peak)	DV4 Loop Voltage Measurement Uncertainty (+/- Vrms)	A Station DV4 Loop Voltage (Vrms)	B Station DV4 Loop Voltage (Vrms)	C Station DV4 Loop Voltage (Vrms)
9.50	120.00	119.66	0.18	1.34	1.35	1.35
11.00	120.00	119.58	0.18	1.67	1.70	1.66
13.00	120.00	119.50	0.18	2.17	2.20	2.20
15.00	120.00	119.33	0.18	2.71	2.80	2.75
17.00	120.00	119.16	0.60	3.35	3.30	3.35
19.00	120.00	118.99	0.60	3.98	4.10	3.90
21.00	120.00	118.16	0.60	4.65	4.60	4.65
23.00	120.00	118.49	0.60	5.30	5.40	5.70
25.00	120.00	118.16	0.60	6.60	6.70	6.60
26.50	120.00	116.94	0.60	7.20	7.20	7.20

Table 10.2 The K1200 Shunt Resistance Measurements

Frequency (MHz)	A Station Rshunt (kOhms)	B Station Rshunt (kOhms)	C Station Rshunt (kOhms)	Average Rshunt (kOhms)
9.50	191.34	206.11	191.85	196.43
11.00	171.97	182.92	170.50	175.13
13.00	150.81	158.30	150.14	153.09
15.00	132.50	138.15	131.92	134.19
17.00	113.55	121.39	112.83	115.92
19.00	103.88	102.11	101.41	102.47
21.00	86.74	87.94	86.16	86.95
23.00	77.40	78.27	77.93	77.87
25.00	65.96	67.81	67.80	67.19
26.50	58.75	61.33	58.99	59.69

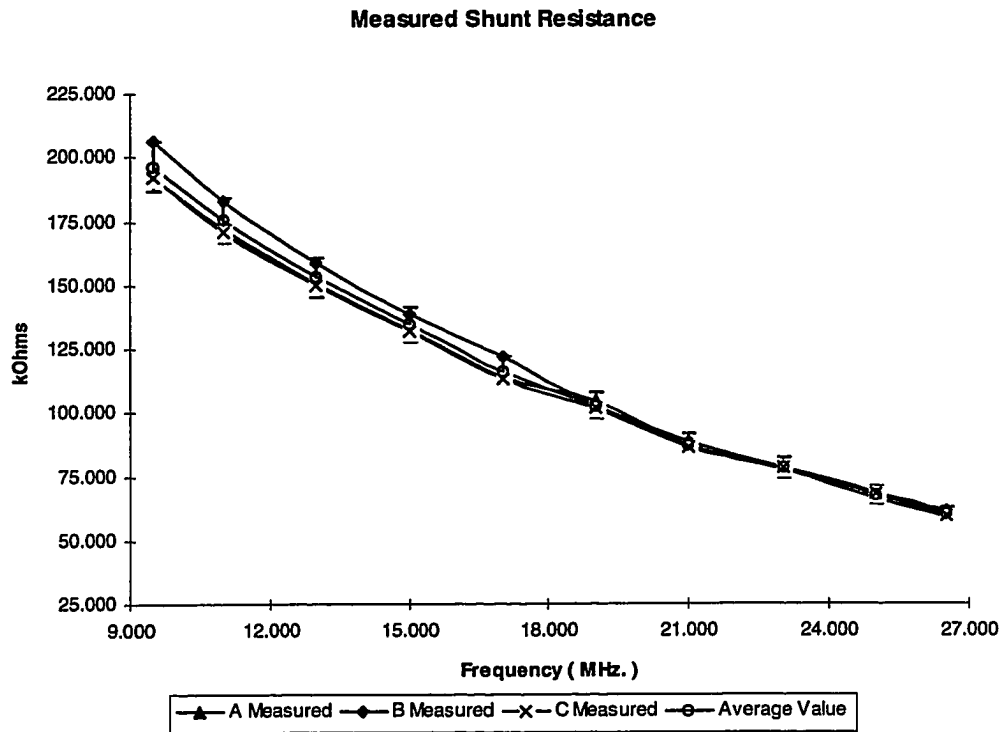


Figure 10.1 The K1200 measured shunt resistance at the cyclotron center.

Table 10.3 The K1200 Tuning Stem Measurements

Frequency (MHz)	A Station Tuning Stem Position (cm)	B Station Tuning Stem Position (cm)	C Station Tuning Stem Position (cm)	Average Tuning Stem Position (cm)
9.50	299.48	295.36	298.18	297.67
11.00	223.68	220.60	223.01	222.43
13.00	156.74	154.27	156.28	155.77
15.00	111.98	110.06	112.07	111.37
17.00	80.93	79.51	80.72	80.39
19.00	58.35	57.00	58.21	57.85
21.00	41.62	40.32	41.32	41.09
23.00	28.51	27.25	28.26	28.01
25.00	18.03	16.80	16.80	17.21
26.50	11.37	10.37	11.18	10.97

### 10.5 The Simulation of the K1200 Resonator Model.

The K1200 resonator model that was developed in chapter nine is analyzed for the same ten frequencies that were measured. An iterative procedure is used to find the tuning stem length resulting in the desired frequency. A detailed analysis is then performed to find the correct value of coupling capacitance and the equivalent shunt circuit parameters at the cyclotron center. The shunt circuit values are then inserted back into the circuit at the cyclotron center location in parallel with the total resonator to simulate the effect of the mating resonator. The value of input coupling capacitor is then sought and inserted into the circuit. An iterative procedure is again used to find the tuning stem position needed to regain the correct resonant frequency. Finally, a detailed analysis is made to document the circuit response. Table 10.4 tabulates the results of the simulation.

Table 10.4 The K1200 Resonator Simulation

Frequency (MHz)	Stem Length (cm)	Rs (kOhms)	Cs (pF)	Ls (nH)	Input Coupling Capacitor (pF)
9.50	297.36	233.30	567.40	494.70	4.71
11.00	222.30	214.60	532.40	393.20	4.23
13.00	154.90	190.30	494.60	303.20	3.94
15.00	109.90	168.60	462.20	243.70	3.62
17.00	78.75	150.30	433.20	202.40	3.38
19.00	56.05	134.50	406.40	172.70	3.19
21.00	38.30	119.50	384.20	149.50	3.04
23.00	25.66	110.00	358.10	133.80	2.90
25.00	14.80	100.20	337.10	120.20	2.79
26.50	7.50	93.01	326.10	110.60	2.70

As given in section 8.4.1, the non-uniform transmission lines modeled with the SEC development were found to converge at a rate proportional to  $1/N^2$ , where  $N$  is the number of series connected SECs used to represent the line. The study of the linearly tapered line in section 8.4 established the model error as a function of segment length (rf degrees) as shown in figure 8.8. For the K1200 model, the tapered transmission line section with the coarsest segmentation is in the set of segments T33 - T36 as shown in figure 9.8. For this section of line,  $\tau = 1.93$  and the electrical length at 27 MHz is 0.286 radians or 16.4 degrees. Using the formula from section 8.4.1,  $Z_{o2}/Z_{o1} = 6.1$ . Using the plot in figure 8.8, for an error of less than 0.5% the line would need to be represented by series connected SECs of less than 14 degrees long each. Since each line segment used in the current model to represent the line is  $16.4/4 = 4.1$  electrical degrees long, the model segmentation is more than adequate for

the desired accuracy. As a test of this premise, the segmentation of the line was doubled and the model analyzed at 26.5 MHz where it is most sensitive. As expected, the change in equivalent shunt circuit elements was less than 0.1% verifying that the model is converged with respect to segment length and that no significant gain of accuracy would be made by further segmentation.

The highest frequency (26.5 MHz) is where the resonator is most sensitive to the elements of the model with the largest uncertainty. Therefore, the sensitivity of the resonator response to each element is evaluated at 26.5 MHz. The sensitivity of the model to each element is ascertained with the technique described in chapter five that compares the amount of energy and power dissipated of the element to the total energy. A list of all of the elements in the model and the percent of electric and magnetic energy it stores and the power it dissipates is listed in table 10.5. For example, one of the elements with a large uncertainty is the dee tip capacitance listed as CDT. Table 10.5 shows that this element manages less than 1 % of the total electric energy and none of any other form. It is therefore not necessary to pursue a more rigorous value.

Table 10.5 The K1200 Element Sensitivity at 26.5 MHz

<b>Element Name</b>	<b>Fraction of Total Power (%)</b>	<b>Fraction of Total Electric Energy</b>	<b>Fraction of Total Magnetic Energy</b>
RSH	49.70	0.00	0.00
LSH	0.00	0.00	49.99
CSH	0.00	49.95	0.00
CDT	0.00	0.39	0.00
TR1	0.00	1.21	0.00
TR2	0.02	2.24	0.01
TR3	0.06	2.38	0.04
TR4	0.11	2.25	0.08
TR5	0.17	2.14	0.16
TR6	0.28	2.37	0.28
TR7	0.28	1.70	0.29
TR8	0.41	1.57	0.44
TR9	0.48	1.52	0.53
TR10	0.78	1.48	0.83
TR11	0.69	1.31	0.69
TR12	0.57	1.41	0.58
TR13	0.44	1.45	0.44
TR14	0.32	1.32	0.31
TR15	0.33	1.92	0.34
TR16	0.17	1.38	0.18
TR17	0.14	1.40	0.14
TR18	0.10	1.22	0.10
CCC	0.00	0.89	0.00
CC	0.00	0.87	0.00
VC	0.00	0.00	0.00
TR19	0.05	1.38	0.05
TR20	0.03	1.27	0.02
TR21	0.01	1.19	0.01
TR22	0.00	1.02	0.00
TR23	0.00	0.35	0.00
CT	0.00	0.10	0.00
CDFT	0.00	1.70	0.00
TR24	0.00	0.00	0.00

Table 10.5 ( continued )

<b>Element Name</b>	<b>Fraction of Total Power (%)</b>	<b>Fraction of Total Electric Energy (%)</b>	<b>Fraction of Total Magnetic Energy (%)</b>
TR25	0.02	0.00	0.01
Rx	0.01	0.00	0.00
VDFT	0.00	0.00	0.00
TR26	0.21	0.20	0.29
CDL	0.00	0.03	0.00
TR27	2.70	4.68	3.63
RJ1	0.24	0.00	0.00
TR28	0.65	0.35	0.94
RJ2	0.39	0.00	0.00
TR29_1	0.35	0.12	0.56
CT29	0.00	0.11	0.00
TR29_2	0.35	0.12	0.57
TR30	0.77	0.17	1.34
CS1	0.00	0.10	0.00
RJ3	0.30	0.00	0.00
ANCS1	0.31	0.00	0.00
TR31	0.99	0.29	1.08
TR32	1.09	0.30	1.20
TR33_1	1.91	0.50	2.18
CT33	0.00	0.01	0.00
TR33_2	1.98	0.47	2.08
TR34_1	1.90	0.44	1.97
CT34	0.00	0.01	0.00
TR34_2	1.96	0.42	1.87
TR35_1	1.90	0.40	1.76
CT35	0.00	0.01	0.00
TR35_2	1.96	0.38	1.65
TR36_1	1.92	0.36	1.55
CT36	0.00	0.01	0.00
TR36_2	1.99	0.35	1.44
TR37_1	0.77	0.12	0.63
CS2	0.00	0.09	0.00
CT37_1	0.00	0.00	0.00
CT37_2	0.00	0.04	0.00
TR37_2	0.79	0.10	0.77

Table 10.5 ( continued )

<b>Element Name</b>	<b>Fraction of Total Power (%)</b>	<b>Fraction of Total Electric Energy (%)</b>	<b>Fraction of Total Magnetic Energy (%)</b>
RJ4	0.56	0.00	0.00
ANCS2	0.84	0.00	0.00
TR38_1	1.08	0.09	2.04
CT38_1	0.00	0.00	0.00
CT38_2	0.00	0.01	0.00
TR38_2	1.09	0.07	2.15
TR39_1	0.90	0.05	2.14
CT39_1	0.00	0.01	0.00
CT39_2	0.00	0.01	0.00
TR39_2	0.91	0.04	1.98
TR40_1	0.37	0.02	0.86
CT40	0.00	0.01	0.00
TR40_2	0.37	0.02	0.74
TR41	0.85	0.04	1.40
CS3	0.00	0.00	0.00
RJ5	0.40	0.00	0.00
ANCS3	0.27	0.00	0.00
TR42_1	0.60	0.01	1.58
CT42	0.00	0.00	0.00
TR42_2	0.60	0.00	1.59
CPlate	0.00	0.01	0.00
TR43	0.61	0.00	1.68
CS4_1	0.00	0.01	0.00
TR44	1.70	0.02	1.00
RJ6	0.16	0.00	0.00
ANCS5	0.51	0.00	0.00
TR46	0.00	0.00	0.01
CS5_1	0.00	0.00	0.00
RJ7	0.62	0.00	0.00
RJ8	2.32	0.00	0.00
ANCS4	2.20	0.00	0.00
TR45	0.96	0.00	1.78
RJ9	0.16	0.00	0.00
RJ10	0.59	0.00	0.00
ANT45	0.77	0.00	0.00
VShort	0.00	0.00	0.00



## 10.6 Comparisons of Measurements to Simulations

The results of the simulations are compared with the results from the measurements in table 10.6.

Table 10.6 The K1200 Simulated and Measured Average Values

Frequency (MHz)	Measured Average Rshunt (kOhms)	Simulated Rshunt (kOhms)	Measured Average Tuning Stem Position	Simulated Tuning Stem Position
9.50	196.43	233.30	297.67	297.36
11.00	175.13	214.60	222.43	222.30
13.00	153.09	190.30	155.77	154.90
15.00	134.19	168.60	111.37	109.90
17.00	115.92	150.30	80.39	78.75
19.00	102.47	134.50	57.85	56.05
21.00	86.95	119.50	41.09	38.30
23.00	77.87	110.00	28.01	25.66
25.00	67.19	100.20	17.21	14.80
26.50	59.69	93.01	10.97	7.50

Figure 10.2 plots the simulated and measured shunt resistance and figure 10.3 plots the simulated and measured tuning stem positions. The shunt resistance error is defined as

$$\% \text{ Error} = \frac{R_{\text{measured}} - R_{\text{simulated}}}{R_{\text{measured}}} \times 100\%.$$

The tuning stem error is plotted as  $L_{\text{measured}} - L_{\text{simulated}}$ . The next section discusses the results.

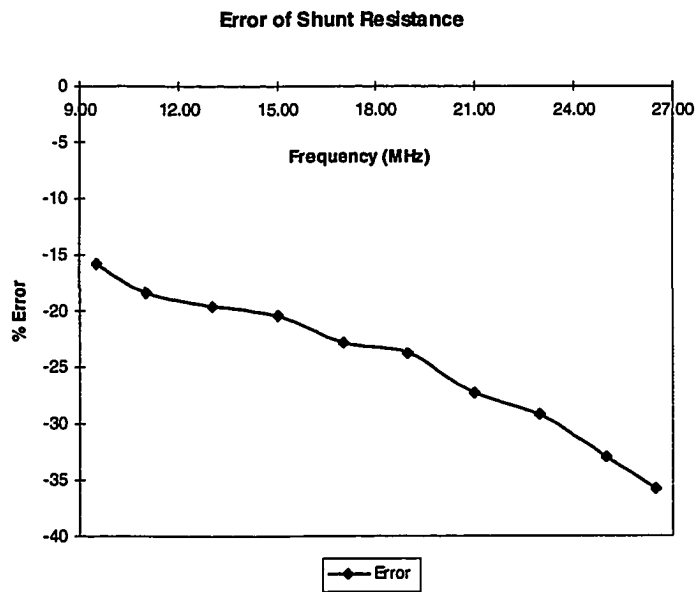
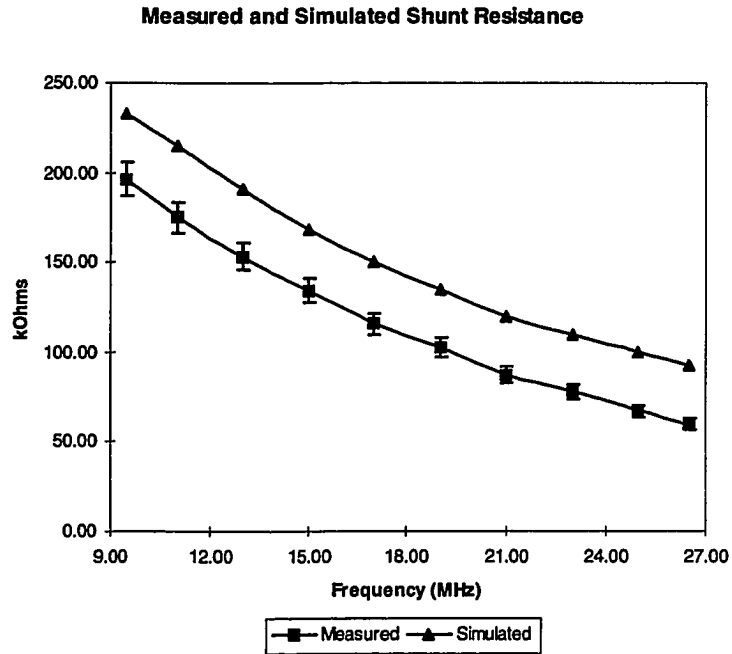


Figure 10.2 The K1200 simulated versus measured shunt resistance.

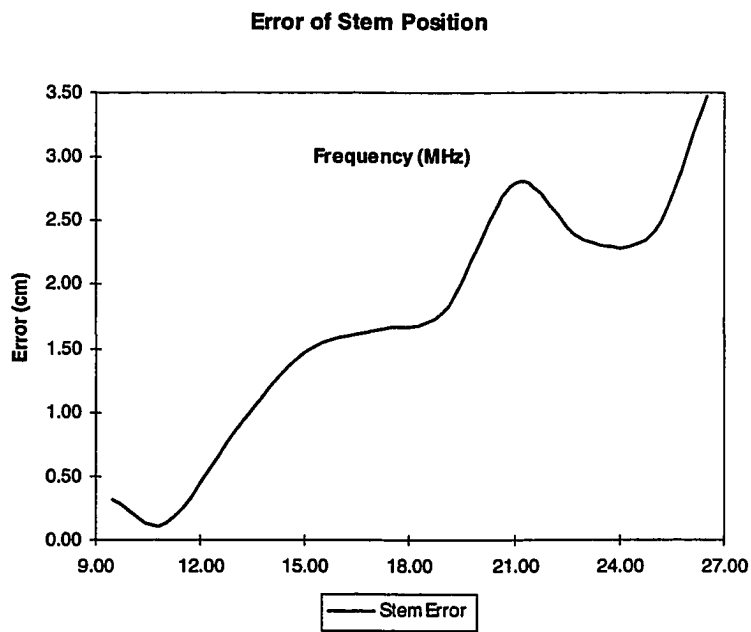
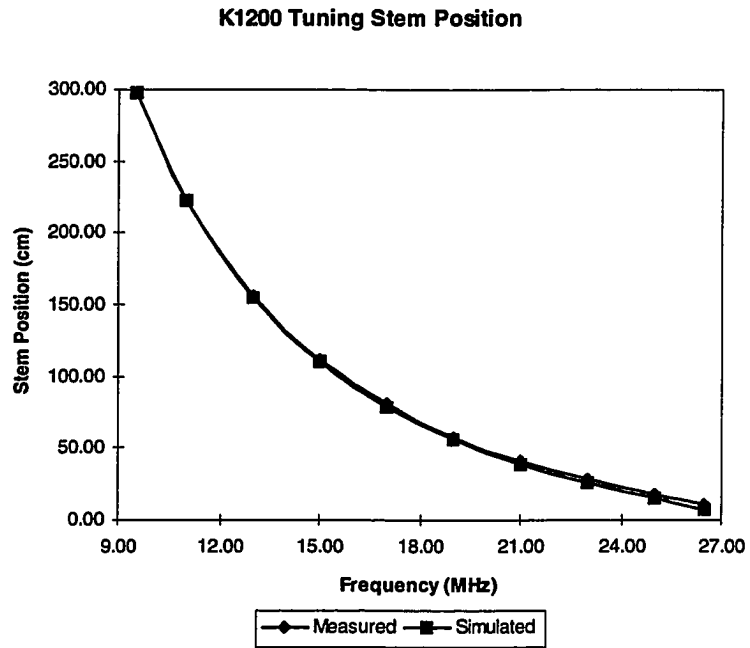


Figure 10.3 The K1200 tuning stem measured versus simulated positions.

## 10.7 Adjustments to the Simulation Model to Match Measurements

The results of the resonant frequency versus stem position are in very good agreement so that no further investigation is warranted. However, the losses are, as predicted in chapter three, off by a significant percentage. This is thought to be due to a combination of the large uncertainty in the joint resistances and the resistivity of the heavily worked and welded surfaces.

It is "postulated" that the material surface properties are more suspect than the joints. The reason becomes apparent if table 10.4 is inspected for the combined total of the total joint resistance losses as compared to the total losses in the surfaces. A change in joint resistance for the bolted joints in excess of the measured finger resistance would be needed to create the increased losses necessary to match the measurements. It is "believed" that this level of joint losses would become problematic to the machine operations which has not been observed.

When the resistivity of the effected surfaces are degraded by a factor of 3.2, then the results begin to match measurements closely as shown in figure 10.4. The agreement is shown to be within the +/- 5 % measurement tolerance. The surfaces in question include all of the dee and liner surfaces consisting of lines T1 - T30 , the spinnings associated with the stem passing through the magnet steel which include the inner conductors of T31 - T37, the inner and outer conductors of T38 - T40, and the outer conductors of T41 - T44. All other surfaces not mentioned, to include all of the annuli, are not degraded in this study. Detailed research with specially designed apparatus would be needed to investigate this problem systematically with confidence.

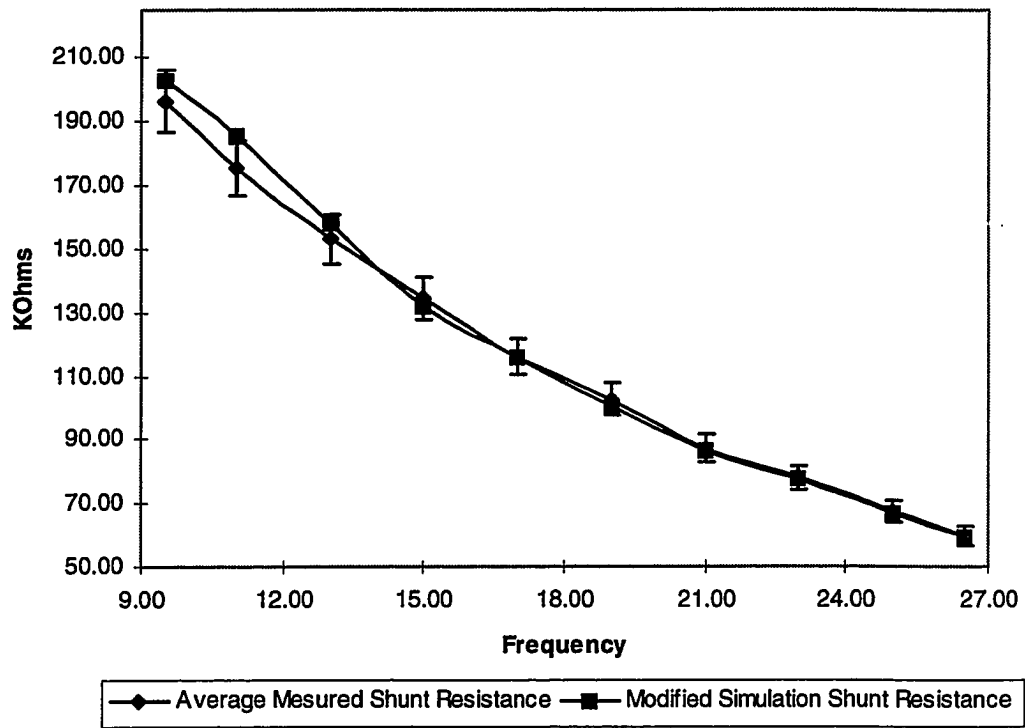
**Measured and Modified Simulated Shunt Resistance**

Figure 10.4 The simulated shunt resistance with the resistivity degraded.

## **CHAPTER ELEVEN**

### **Summary**

#### **1.0 Overview of the Problem**

Techniques for developing and applying an equivalent circuit to the analysis of rf resonators have been developed and described. These techniques were applied to model the K1200 cyclotron rf resonators at the National Superconducting Cyclotron Laboratory and verified by comparing the model predictions to the experimental measurements of the K1200.

Along with the techniques specifically developed as a part of this research, many additional techniques commonly used to work with high power resonators are also included. This is an attempt to bring together in one document the relevant techniques organized and specifically aimed at this category of application.

The procedures developed in this thesis were applied to model and analyze the K1200 rf resonator. The tuning response was predicted with good accuracy, supporting the premise that the reactive elements of the model were modeled appropriately. However, the comparisons between the predicted and measured conduction loss were less favorable. Since the voltage and current distribution can be inferred to be correct from the tuning response, and the overall conduction loss across the tuning range seems functionally correct, the higher experimental conduction power loss

can be attributed to issues not associated with the modeling techniques applied.

The increased losses observed can be attributed to lower than actual values being used in the model for joint resistance, and for the resistivity of surfaces that were significantly modified by welding or mechanical shaping. It is postulated that the most significant component is due to the uncertainty of the surface resistivity of specified conductors since the bolted joint resistances would need to be degraded significantly beyond measurements of the NSCL finger contact resistance to account for the increased loss. In fact, by increasing the model values for surface resistivity of heavily modified conductors by a factor of 3.2, the conduction loss was brought to within the measurement uncertainty across the entire tuning range. This is consistent with the postulate that the conductor surface resistivity is significantly altered by welding or mechanically shaping.

## **2.0 Summary of the Dissertation**

The dissertation begins in chapter one and two with a brief discussion of the dissertation scope, the research institution, and the history of the relevant techniques and associated software. Material properties and phenomena unique to vacuum insulated rf structures are discussed in chapter three followed by a discussion of the computer software used or developed in chapter four. A set of techniques for modeling rf structures is described in chapters five through eight. Chapters nine and ten apply the techniques to the modeling, measurements, and analysis of the K1200 rf resonators.

The common use of an R, L, C parallel resonant circuit to represent the overall response of a more complex resonant system is described in chapter five. The technique is useful as an aid to 1) analyze interactions between complex structures, 2) facilitate the design of needed components such as input and output couplers, or 3) simply describe the overall response in a simple understandable way. Additionally, a method for expanding the R, L, C representation in a manner useful for 1) analyzing complex interactions between the resonator components, or 2) measuring the relative effect of a particular component to the overall resonator response, or 3) quantifying the effect of the uncertainty of any element to the overall circuit response was described.

Many common techniques are investigated such as the handling of corners and bends by extending the transmission lines an appropriate distance into the corner as is described in chapter seven. Commonly applied equivalent circuits for modeling lumped elements that exhibit parasitic effects is described in chapter six. Perhaps the most relevant portions of the modeling process developed deals with the modeling of nonstandard transmission lines as described in chapters seven and eight.

Chapter seven describes and develops techniques to appropriately model abrupt discontinuities, corners and bends along the guided wave axis, as well as transmission lines with nonstandard cross-sections. The method developed to transform a nonstandard transmission line to a equivalent standard representation conserves the electrical properties of the original line. The electrical properties preserved include the material properties, the conduction loss of each conductor by determining an "Equivalent Width" denoted by " $w_e$ " that accrues the same losses as the



original conductor yet with a constant current density, and the characteristic impedance denoted by " $Z_o$ ". The mapping is accomplished using the electric field determined with electrostatic techniques. The electrostatic stored energy ( $U_e$ ) and the electric fields on the surface ( $E_s$ ) are used. The results for 1 Volt applied are:

$$Z_o = \frac{1}{2vU_e} \quad \text{and} \quad w_e = \frac{\left[ \int_0^l |E_s| dl \right]^2}{\int_0^l |E_s|^2 dl},$$

where " $v$ " is the group velocity.

Chapter eight developed methods for modeling transmission lines with a cross-section that varies along the guided wave axis which are referred to as "non-uniform" in the literature. Since the model developed has no lower cut-off frequency, the technique seeks to maintain the average electrostatic and magnetostatic energy that would be accrued along each segment under dc conditions. The non-uniform line is broken into series connected segments with each segment defined by a "Segment Equivalent Circuit" denoted by SEC. The SEC contains both lumped and transmission line elements. The lumped element portion of the SEC is designed to model the effects of the longitudinal field components that are determined from the actual geometry by resolving the net geometric variation along the guided wave axis by an abrupt discontinuity in the center of the segment. Techniques described in chapter seven are applied to evaluate the discontinuity for the appropriate lumped circuit topology and element values. The transmission line elements of the SEC are determined by using the transverse field components to determine a

so-called "Transverse Characteristic Impedance" denoted by  $Z_t$  at each end of the segment. The segment must be chosen short enough to be able to model the variation of  $Z_t$  as linear along its length and to further maintain a desired error tolerance at the highest frequency of interested. Under these conditions the constant characteristic impedance and loss characteristics of the SEC is determined from

$$Z_t = Z_{t1} \sqrt{\frac{1(\tau^2 - 1)}{2 \ln(\tau)}}, \quad w_e = \frac{w_{e2} - w_{e1}}{\ln\left(\frac{w_{e2}}{w_{e1}}\right)}$$

with  $Z_{t1}$  being the impedance at one end of the segment,  $w_{e2}$  and  $w_{e1}$  being the equivalent width of a conductor at each end of the segment ( this expression is evaluated for each conductor separately), and

$$\tau = \frac{Z_{t2}}{Z_{t1}}$$

The resonant frequency for multiple exponentially tapered transmission line quarter-wave resonators is found to converge to within 0.04% of the theoretical solution using the techniques developed. The error is shown to converge to zero with a rate proportional to  $\sim 1/N^2$  (N being the number of series connected SECs used to describe the non-uniform segment) through evaluation of multiple linearly tapered resonators.

### 3.0 Conclusion

A technique to model rf resonators operating in a transmission line mode has been successfully described, developed, tested, and applied to the complex K1200 Superconducting Cyclotron rf resonators. The K1200 tuning stem length versus frequency was calculated and measured. Over the 300 centimeters of travel, the measured tuning stem position versus frequency matched the calculations with a error varying from a worst case of approximately 3.5 cm at 26.5 MHz to less than 1 cm at 9 MHz. This indicates that the reactive elements of the resonator were accurately predicted. However, the lack of agreement of the power loss between the model and experimental data likely stems from a lack of realistic values for the resistivity of certain conducting surfaces. This is a problem that is not specific to the techniques applied. By increasing the surface resistivity by a factor of 3.2 for conducting surfaces comprising the K1200 resonator that were heavily worked or welded, the simulated results matched the measured results within the error margins of +/- 5 %.

In conclusion, techniques described in this dissertation seem well suited to the analysis and design of high power rf resonators operating in the transmission line mode. A problem with predicting the surface resistivity of worked or welded conductors has been identified and further research will be needed to experimentally determine these quantities.

#### **4.0 Directions for Future Research**

During the course of this research, topics were identified which would benefit from further investigation.

1. It was postulated that the surface resistivity of the heavily welded or worked surfaces was a factor of 3.2 higher than the textbook or manufacturer's value of the perfect bulk material. To further investigate the accuracy of this postulate, a special apparatus that can isolate and measure these effects accurately would need to be designed and constructed. Since this is a significant source of error for this type of equipment, the information gained would improve the model predictions particularly in the area of conduction power losses.

2. It was found that different methods of choosing  $Z_t$  resulted in reduced error for either the magnetic or electric stored energy. This may be used to advantage to better predict the response at some particular resonant frequency. First the structure would be analyzed with the form of  $Z_t$  described in chapter eight that best preserves both forms of energy simultaneously to identify a particular resonant frequency of interest. Then a detailed analysis of this frequency to determine the forms of energy each transmission line manages would be made. Second, for transmission lines identified to be managing predominantly one form of energy,  $Z_t$  would be recalculated for this segment using the formulation that best preserves the dominant energy. Third, the modified model would be re-analyzed for the new resonant frequency and other values of interest. Computer software

could be written to apply this technique and thereby provide a refinement to the algorithm presented in this thesis.

3. Continued research could be aimed at refining the methods for determining the elements of the SEC in a way that would better preserve the time delays and stored energy. This research may also be aimed at facilitating a broader range of geometrically complex structures without significantly complicating the process.

## **LIST OF REFERENCES**

- [1.1] J. Vincent, 1986 NSCL Annual Report, "General RF Design and Analysis Techniques for Two-Conductor, Non-Symmetric, and Non-Uniform Resonators," pp.141-144.
- [1.2] J. Vincent, NSCL RF Note #103, "An Electrostatic Stored Energy Subroutine for Poisson," NSCL Internal Publication, January 15, 1986.
- [1.3] J. Vincent and J. Priller, 1991 NSCL Annual Report, "PC RESON: Radio Frequency Circuit Analysis for PC's," pp. 205-205
- [1.4] W. L. McPherson, "ITT Reference Data for Radio Engineers", Howard W. Sams & Co., Sixth Edition, 1981
- [1.5] Edward C. Jordan, "SAMS Reference Data for Engineers: Radio, Electronics, Computer, and Communications", Howard W, Sams & Co., Seventh Edition, 1985
- [2.1] K. Halbach, "Calculation of the Stray field of Magnets with Poisson," Nucl. Instr. and Meth., 66 (1968) p154-156.
- [2.2] K. Halbach, "SUPERFISH - A computer program for evaluation of RF cavities with cylindrical symmetry," Particle Accelerators, Vol 7, 1976, pp 213-222.
- [2.3] R. Klatt, et al, "MAFIA - A Three-Dimensional Electromagnetic CAD System for Magnets, RF Structures, and Transient Wake-Field Calculations," Proceedings of the 1986 Linear Accelerator Conference, Stanford Linear Accelerator Center Report SLAC-303, June 1986, pp. 276-278
- [2.4] L.W. Nagel and R.A. Roher, "Computer Analysis of Nonlinear Circuits, Excluding Radiation (CANCER)," IEEE J. of Solid State Circuits, vol. SC-6, August 1971, pp. 166-182

- [2.5] L.W. Nagel and D. O. Perderson, "Simulation Program with Integrated Circuit Emphasis," Proc. Sixteenth Midwest Symposium on Circuit Theory, Waterloo, Canada, April 12, 1973; available as Memorandum No. ERL-M382, Electronics Research Laboratory, University of California, Berkeley.
- [2.6] S. Shinnars, "Modern Control System Theory and Applications," Addison-Wesley Publishing Co., 1978, pp 135-137
- [2.7] W. Alan Davis, "Microwave Semiconductor Circuit Design," Van Nostrand Reinhold Co., 1988
- [2.8] P. Krause, "Analysis of Electric Machinery," McGraw Hill, 1986
- [2.9] W. Van Genderan, et al., "Calculation of Cyclotron RF Systems," Nucl. Instr. and Meth. in Physics Research, A258, (1987), pp. 161-169.
- [3.1] R. D. Reiswig, "Metallographic Observations on Copper Samples from AT-1", Memorandum MST-6, Los Alamos National Laboratory, March 24, 1987.
- [3.2] R. D. Lending, "New Criteria for Microwave Component Surfaces," Proc. of the National Electronics Conference, Vol. 11, pp. 391-401, 1955
- [3.3] Parker Seals Group, "Waveguide Flange and EMI Sealing," Parker Seals Group, 1982
- [3.4] J. O. Turner, "Electrical Conductivity of Soldered and Welded Joints," DESIGN DATA, Lawrence Berkeley Laboratory, University of California, D.D. 25.1, May 5, 1951
- [3.6] W. Weingarten, "Superconducting Cavities," CERN Accelerator School: RF Engineering for Particle Accelerators, CERN, Geneva, Switzerland, 1991.



- [3.7] J. Vincent, et. al., "NSCL RF Note # 113: Practical Aspects of Superconducting RF Technology", NSCL Internal Publication, March 1993.
- [3.8] W. D. Kilpatrick, "A Criterion for Vacuum Sparking Designed to Include both R.F. and D.C.," University of California Radiation Laboratory, UCRL-2321, September 4, 1953
- [3.9] A. J. Hatch, "Suppression of Multipactoring in Particle Accelerators," Nuclear Instruments and Methods, No. 41, pp 261-271, 1966
- [3.10] D. H. Preist, "On the Heating of Output Windows of Microwave Tubes by Electron Bombardment," IRE Transactions on Electron Devices, March 27, 1961
- [3.11] D. P. Sanderson and G. Stork, "RF Coupler Insulator Fabrication at NSCL," NSCL Annual Report, pp 184 - 186, 1991
- [4.1] John Priller and John Vincent, "PC-RESON version 1.3 Command and Element Reference," NSCL Internal Publication, May, 1993
- [4.2] J. Vlach, K. Singhal, "Computer Methods for Circuit Analysis and Design," Van Nostrand Reinhold Company, 1983.
- [4.3] William H. Hayt, JR., "Engineering Electromagnetics," Fourth Edition, McGraw-Hill Book Company, 1981.
- [6.1] F. D. Terman, "Radio Engineer's Handbook", McGraw-Hill Book Company, Inc., First Edition, 1943
- [6.2] R. Landee, D. Davis, A. Albrecht, "Electronics Designers Handbook," McGraw-Hill Book Company, Second Edition, 1977
- [6.3] H. A. Wheeler, "Simple Inductance Formulas for Radio Coils," Proc. I.R.E., Vol. 16, p. 1398, October, 1928
- [6.4] W. L. McPherson, "ITT Reference Data for Radio Engineers", Howard W. Sams & Co., Sixth Edition, 1981

- [6.5] F. Pigeaud, "NSCL RF Note # 114: Notes on Shielded Coil Design, " NSCL Internal Publication, June 1993
- [6.6] W. R. Smythe, "Reducing Ferrite Tuner Power Loss by Bias Field Rotation," IEEE Transactions on Nuclear Science, Vol. NS-30, No. 4, pp 2173 - 2175, August, 1983
- [6.7] L.M. Earley, et. al., "Rapidly Tuned Buncher Structure for the Los Alamos Proton Storage Ring (PSR)," Bull. Am. Phys. Soc., No 28, pp 106, 1983
- [6.8] L. S. Nergaard and B. Salzberg, "Resonant Impedance of Transmission Lines, " Proceedings of the I.R.E., pp 579 - 584, September, 1939
- [7.2] P.I. Somlo, "The Computation of Coaxial Line Step Capacitance's," IEEE Transactions on Microwave Theory and Techniques, vol. MTT-15, No. 1, pp 48-53, January, 1967
- [8.1] C. P. Womack, "The Use of Experimental Transmission Lines in Microwave Components," IRE Transactions on Microwave Theory and Techniques, vol. 10, pp 124-132, 1962
- [8.3] H. Kaufman, "Bibliography of Nonuniform Transmission Lines," IRE Transactions on Antennas and Propagation, vol. AP-3, pp. 218-220, October 1955.
- [8.4] O. P. Rustogi, "Linearly Tapered Transmission Line and its Application in Microwaves," IEEE Transactions on Microwave Theory and Techniques, vol. 17, pp 166-168, 1969
- [8.5] R. W. Kloppenstein, "A Transmission Line Taper of Improved Design," Proceedings of the IRE, vol. 44, pp 31-35, 1956
- [8.6] E. F. Bollinder, "The Optimum Tapered Transmission Line Section," Proceedings of the IRE, vol. 44, pp 1056, 1956
- [8.7] E. F. Bollinder, "Fourier Transforms and Tapered Transmission Lines," Proceedings of the IRE, vol. 44, pp 557, 1956

- [8.8] R. E. Collin, "The Optimum Tapered Transmission Line Matching Section," Proceedings of the IRE, vol. 44, pp 539, 1956
- [8.9] I. Sugai, " The Solutions for Nonuniform Transmission Line Problems," Proceedings of the IRE, vol. 48, pp. 1489-1490, August, 1960
- [8.10] I. Sugai, " A New Exact Method of Nonuniform Transmission Lines," Proceedings of the IRE, vol. 49, pp. 627-628, March, 1961
- [10.1] Thomas R. Jones, "NSCL RF Note # 105: Measurement Results from Low Power Model with Racetrack Dee," NSCL Internal Publication, January 1996.
- [10.2] Peter Miller and Edwin Kashy, "Absolute Calibration of Dee Voltage by X-ray Endpoint," Proceedings of the 7<sup>th</sup> International Conference on Cyclotrons and their Applications, 1975, pp. 171-174.